UCLA
UCLA Electronic Theses and Dissertations

Title
The Properties of Mesporous Silica Nanomaterials and their Biological Applications

Permalink
https://escholarship.org/uc/item/1gr8p8km

Author
Hwang, Angela An-Chi

Publication Date
2015

Peer reviewed|Thesis/dissertation

eScholarship.org Powered by the California Digital Library
University of California

UNIVERSITY OF CALIFORNIA

Los Angeles

The Properties of Mesporous Silica Nanomaterials and their Biological Applications

A dissertation submitted in the partial satisfaction of the requirements for the degree of Doctor of Philosophy in Chemistry

By

Angela An-Chi Hwang

2015

ABSTRACT OF THE DISSERTATION

The Properties of Mesporous Silica Nanomaterials

and their Biological Applications

by

Angela An-Chi Hwang

Doctor of Philosophy in Chemistry

University of California, Los Angeles, 2015

Professor Jeffrey I. Zink, Chair

The research discussed in this thesis is divided into a total of five chapters, and divided into two sections. In section one, novel silica nanomaterials are developed for biological applications. Chapter one discusses the invention and development of mesoporous silicate nanomaterial, as well as their biomedical application towards a drug delivery system to treat diseases. Chapter two highlights the exploration of combining multiple modalities to a mesoporous silica nanoparticle system, applied to both in vitro and in vivo models. In order to combine two functions into a nanoparticle system, several iterations are designed to synthesize a pH-sensitive nanovalve to be used in conjunction with transferrin, a popular targeting agent. In vitro results are very promising to improve the targeted and controlled delivery of doxorubicin, and show the first proof of concept for a multifunctional nanoparticle. Chapter three delves into the development of large pore silica nanoparticles to deliver biomolecules and utilizing the pH-sensitive biopolymer, chitosan, as a capping agent. Chitosan serves to be a promising potential capping agent, however further

optimizational studies are necessary to increase the loading capacity and improve release of cargo. In section two, the practical applications of mesoporous silica nanoparticles are discussed in order to treat a variety of diseases, such as tuberculosis, tularemia, and cancer. The fourth chapter discusses the fate of the mesoporous silica nanoparticles after they are exocytosed from cells in a two-pronged approach. Cells are treated with nanoparticles are labeled with fluorescent dye and a variety of inhibitors, and monitored by fluorescence microscopy to determine the mechanism of exocytosis. Nanoparticles are synthesized with a magnetic core to be collected, and the proteins adsorbed onto the surface are analyzed by mass spectrometry to be tested as a diagnostic tool. The protein corona composition varies from the various surface charges, when incubated with A549, MCF7, or HFF cells. Proteins unique to cancer cell lines are identified, which indicate mesoporous silica nanoparticles as a promising diagnostic tool. Finally, chapter five discusses the optimization of delivering isoniazid, a small molecule antibiotic, using an acid-sensitive hydrazone bond to covalently attach the drug to the surface of the MSNs to treat tuberculosis. Two size iterations are examined (50 and 100 nm diameters), which show the differences in cellular uptake and in vivo biodistribution. We see a very effective delivery of isoniazid-loaded MSNs, which is a significant improvement when compared to the free drug in both in vitro and in vivo models.

The dissertation of Angela An-Chi Hwang is approved.

Michael Jura

Yves Rubin

Jeffrey I. Zink, Committee Chair

University of California, Los Angeles

2015

DEDICATION

For my parents, Ling-Ling Tang and Hsien-Tang Hwang.

TABLE OF CONTENTS

ACKNOWLEDGEMENTS

My journey throughout graduate school has given me the fortunate opportunity to encounter and collaborate with a wide variety of people, that has shaped my understanding on science as well as my outlook on life. I am especially indebted to my advisor, Professor Jeffrey I. Zink, who is a hardworking scientist that truly cares about the welfare of his students, of which I have found is rare. I would like to thank him for the opportunity to perform great research in his lab and collaborate on many significant projects. He has mentored me directly with the encouragement to publish my findings and proposing new ideas, as well as set paradigms for me to follow. His longstanding tenure at UCLA is exemplary of the great integrity he has for science, and for his colleagues and employees. My gratitude of his support through pursuing my career path is impalpable, and I am forever grateful for his mentorship.

The development of my research would be nothing without my collaborators. In particular, I would like to recognize Professor Fuyuhiko Tamanoi and his lab for allowing me to work with Dr. Jie Lu and Dr. Rolando Yanes, who have taught me a great deal about cancer biology. I also like to acknowledge Dr. Marcus Horwitz, Dr. Daniel Clemens, and Dr. Bai-Yu Lee for their efforts in treating tuberculosis and tularemia with nanoparticle-based systems. I'd also like to thank Professor Joseph Loo for the interdisciplinary work we achieved on understanding the protein corona that evolves on MSNs.

I would also thank my lab— they are the greatest colleagues and confidants. My dear lab mates who came before me, Dr. Zongxi Li, Dr. Eunshil Choi, Dr. Courtney Thomas, Dr. Daniel Ferris, Dr. Derrick Tarn, Dr. Matt Kiesz, Dr. Bryana Henderson, Dr. Sanaz Gardner, and Dr. Yuen Lau, gave me great guidance, from taking cumulative exams to understanding the intricacies of materials synthesis. To the people who came after me: Zilu Li, Chia-Jung Yu, Dr. Bastian Rühele,

Dr. Philippe Saint-Cricq Riviere, and Daniel Pazo, I am glad I got to know you and help mentor some of you. I know you will keep the Zink group in high spirits and integrity. I am very fortunate to have such an amazing group of peers, and we have had great experiences in graduate school. In particular, I would like to thank Dr. Min Xue, who has been a great mentor and brother to me. Words cannot express all the help he has given me, I hope to see him become a great professor someday. Dr. Janie Yen-Ting Chen and Dr. Ivy Ju-Yao Dong are two great science sisters! I would not have any other two people go through the trials of graduate school together. We have been a great support system for each other, and I am glad we have become such great friends.

Of course, I could not have completed this journey without the support of good friends. I am forever grateful to Philip Wilcox, who has become of one of the most important people in my life. I didn't see you coming, but I am glad you are here now. I love you. My fellow classmates, Carly Ferguson, Tristin Rose, Matt Cipolla, Blanton Martin, Jon Brown, Andrew Roberts, Andrew Lech, Ira Strahle, , Henry Sillin, Boris Volosskiy, Ivan Ivanov, Ilya Yakovlev, Liane Fukumoto, and Tahani Zeid, are just a handful of the notable people who I know will go on to do great things. I look forward to seeing what great things you will accomplish! I am also thankful that I have had the opportunity to befriend others outside of my chemistry community, which has given me great joy. Chun Mei Nickels, Kim Phifer, Ashley Angulo, Sadie Martin, Terri Johnson, Tanya Vucetic, Damon Alexander, Lee Ricketson, Bryon Aragam, Aromalyn Magtira, and Kaeli Ward are a great motley crew of friends. We are able to talk (ok, sometimes argue) on a wide variety of topics, ranging from science to the latest gossip. I hope to keep you in my life for a while. And my roommate, Katherine McLaughlin, is one of the best products from making friends outside of the chemistry department. She is my partner in crime, even when I can't keep up. She is one of the hardest working, kindest, and self-less people I know. I have learned to embrace life fully, and eat good food (especially the organic kind). I value our long discussions about life and love.

Nothing would be possible without the love from my family. My mother, Ling-Ling Tang, is the strongest woman I know. She has supported me through the difficulties in life, and is continually there to help me. I only wish to be just as great a mother. I hope my father, Richard Hwang, is watching and is proud of me. He has always encouraged higher learning. My family away from home, Annie Hwang, James Hwang, Daniel Hwang, and Pei Fang Hwang, were an invaluable help from me when I moved here with only two suitcases. I am lucky to have the family that I have.

Finally, I would like to thank Professors Michael Jura and Yves Rubin for serving on my thesis committee.

VITA

2009	B.S., Chemistry Pennsylvania State University University Park, PA
2009-2011	Teaching Assistant Department of Chemistry & Biochemistry University of California, Los Angeles Los Angeles, CA
2010	UCLA Distinguished Teaching Award
2013	Materials Research Society Best Poster Award UCLA Departmental Fellowship
2009-2014	Research Assistant Department of Chemistry & Biochemistry University of California, Los Angeles Los Angeles, CA

PUBLICATIONS

1. pH-responsive isoniazid-loaded nanoparticles markedly improve tuberculosis treatment in mice. Angela A. Hwang, Daniel Clemens, Bai-Yu Lee, Marcus Horwitz, and Jeffrey I. Zink. *Manuscript in preparation.*

2. Functional nanovalves on protein-coated nanoparticles for in vitro and in vivo controlled drug delivery. Angela A. Hwang, Jie Lu, Fuyuhiko Tamanoi, and Jeffrey I. Zink. *Small*, 2014, *11*(3), 319-328.

3. Surface charge and cellular processing of covalently functionalized multiwall carbon nanotubes determine pulmonary toxicity. Ruibin Li, Xiang Wang, Zhaoxia Ji, Bingbing Sun, Haiyuan Zhang, Chong Hyun Chang, Sijie Lin, Huan Meng, Yu-Pei Liao, Meiying Wang, Zongxi Li, Angela A. Hwang, Tze-Bin Song, Run Xu, Yang Yang, Jeffrey I. Zink, André E. Nel, and Tian Xia, *ACS Nano*, 2013, *7*(3), 2352-2368.

4. Involvement of Lysosomal Exocytosis in the Excretion of Mesoporous Silica Nanoparticles and Enhancement of the Drug Delivery Effect by Exocytosis Inhibition. Rolando E. Yanes, Derrick Tarn, Angela A. Hwang, Daniel P. Ferris, Sean P. Sherman, Courtney R. Thomas, Jie Lu, April D. Pyle, Jeffrey I. Zink, Fuyuhiko Tamanoi, *Small,* 2012, *9,* 697-704.

5. Measurement of Uptake and Release Capacities of Mesoporous Silica Nanoparticles Enabled by Nanovalve Gates. Zongxi Li, Jeff Nyalosaso Likoko, Angela A. Hwang, Daniel P. Ferris, Sui Yang, Gaëlle Derrien, Clarence Charnay, Jean-Olivier Durand, and Jeffrey I. Zink, *J. Phys. Chem. C*, 2011, *115*, 19496-19506.

CHAPTER 1

Mesoporous Silica Nanoparticles for Biomedical Applications

1.1 Introduction

In 1959, Richard Feynman said 'there's plenty of room at the bottom', alluding to the then abstract concept of designing self-assembled structures at the atomic or molecular scale. Years later, nanoscience has become a hugely diverse field that has created new materials, methods, and a wide scope of applications. Nanotechnology has influenced the engineering of novel devices and its application to medicine is revolutionary. Nanomedicine has drastically improved healthcare with the advent of high-throughput diagnostic devices, contrast agents, and drug delivery systems. Drug delivery utilizes nanoparticle-based systems to maximize the bioavailability of therapeutics in the affected area. By decreasing the quantity of drug needed, the undesirable side effects that are incurred in most therapies are minimized. Due to their small size, nanoparticles are able to navigate the bloodstream and are easily internalized into cells. The large surface area available gives the freedom to incorporate multiple functions such as imaging, on-command delivery, and targeting. Multifunctional nanocarriers are capable of simultaneously targeting the affected areas, delivering a high payload of therapeutics, and diagnostically imaging the treatment. These features make nanoparticles an ideal platform for optimizing the delivery of therapeutics in diseases difficult to treat.

1.2 Mesoporous Silica Nanoparticles (MSNs)

A vast library of nanoparticles have been fabricated and studied, which range from soft polymeric vesicles to hard inorganic nanoparticles. Mesoporous silica nanoparticles (MSNs) are of particular interest due to their natural abundance as a resource, biocompatibility, and highly porous, well-ordered structure.[1–4] MSNs are easily synthesized at a low cost via a surfactant-templated, sol-gel process and their structure can be easily modified with additives to form core-shells or different surfactants for various porosities.[5–8] The highly porous structure creates a high surface-area-to-volume ratio that enables a large amount of cargo to be stored inside the pores, while the remaining

external surface area is available for modifications. The diverse silane chemistry can be utilized to incorporate a wide variety of organic molecules into the silica matrix before or during the synthesis of the MSNs. We, as well as others have shown a multitude of examples that demonstrate the diversity and multifunctionality these nanomaterials possess.[1,2,9–13]

Synthesis of MSNs

Silica nanoparticles are synthesized by employing a modified Stöber process, which was first published by the Werner Stöber in 1968.[14] The method is simple: alkoxysilanes are mixed in the presence of ammonia, ethanol, and water, which can produce a range of sizes of monodisperse solid silica nanoparticles, depending on the ratio of reactants. Typically, tetraethyl orthosilicate (TEOS) is used in basic conditions to promote the base-catalyzed hydrolysis of the alkoxysilanes, which in turn induces the condensation reaction between hydrolyzed alkoxysilanes. These reactions cause the silica precursor to polymerize to form a sol, producing a network of siloxane bonds. The sol then condenses into to gel phase and are aged, to produce a colloid of silica nanoparticles.

$$\text{Hydrolysis: } OH^- + Si(OR)_4 - Si(OR)_3OH + RO^-$$

$$\text{Condensation: } SiO^- + Si(OH)_4 - Si\text{-}O\text{-}Si + OH^-$$

The incorporation of surfactants into the sol enables porous patterning within the silica structure, which was first developed using thin films for catalytic applications.[15,16] The Mobil Corporation later introduced micrometer-sized, hexagonally structured mesoporous particles, known as Mobil Corporation Material #41 (MCM-41).[17] MSNs with biocompatible parameters (monodisperse, diameter ~100 nm) were first synthesized by Cai et al.[18] Methodologies have since evolved into nanoparticles with sizes below 50 nm and a plethora of morphologies.[6,19–21]

The traditional MCM-41 type of MSNs are formed upon the addition of the silica precursor, tetraethyl orthosilicate (TEOS), to a heated, alkaline solution containing the surfactant template, cetyl trimethylammonium bromide (CTAB) (Figure 1.1). These conditions induce a base-catalyzed

condensation of silica around the hexagonally packed micelle structures of the surfactant. After aging, the surfactant is removed by refluxing the MSNs in an acidic alcohol solution. The resulting high surface area nanoparticles are characterized by low angle x-ray diffraction and electron microscopy (Figure 1.2), to confirm particle size (100 nm) and their hexagonal array of pores (2-3 nm).

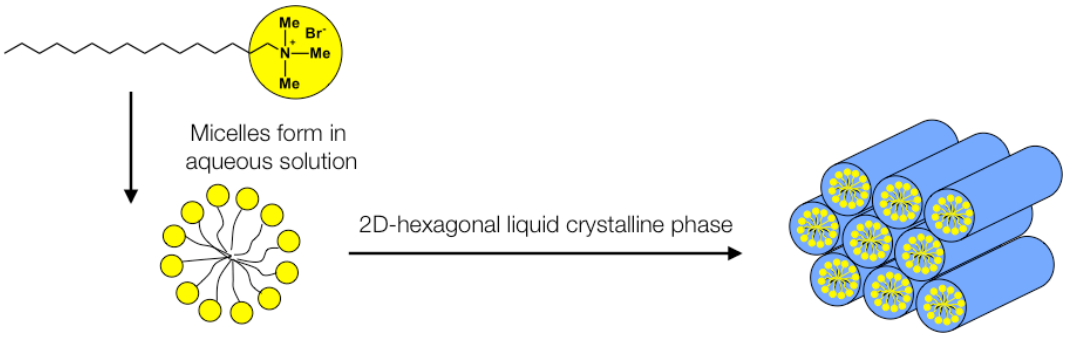

Figure 1.1. Graphical representation of surfactant assembly and the formation of mesoporous silica nanoparticles.

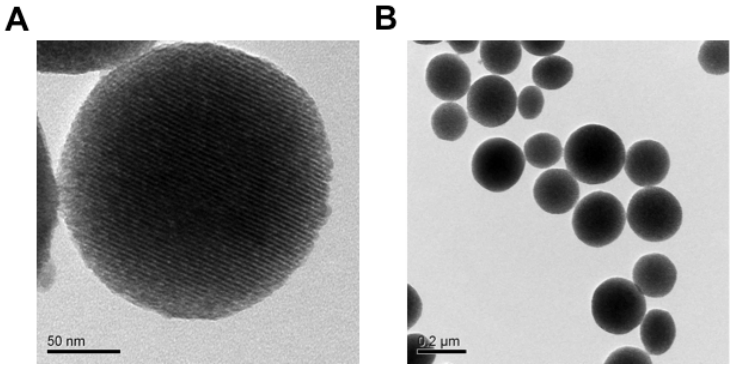

Figure 1.2. TEM images of surfactant-extracted MSNs.

Functionalization of MSNs

To enhance the MSN platform for biological applications, MSNs can be derivatized to incorporate numerous components to give the material a wide range of multifunctional properties. Organic molecules can be utilized in a wide range of uses (Figure 1.3). Supramolecular chemistry can be used to design molecular gate-keepers or nanomachines to trap cargo inside the MSNs' pores.

These nanomachines can be designed in such a way to activate and open upon a specific stimuli, such as heat, pH change, enzymatic cleavage, light, or reduction/oxidation reaction. Fluorescent dyes are used as imaging agents to gain in situ knowledge in cells. Biomolecules that incite biological responses can be used for cell targeting to direct the MSNs to a specific location for an enhanced delivery of cargo. Metal nanocrystal cores, such as superparamagnetic iron oxide, can also be integrated into the silica to be used as magnetic resonance imaging or for magnetic manipulation. Through the use of reactive silanol groups, organic functional groups can be covalently bonded to the MSNs to provide a high degree of versatility and mechanized features to the nanocarriers. For ease of detection in biological systems, organic fluorescent molecules are assimilated into the silica by two methods: co-condensation or post-synthetic grafting. The co-condensation method facilitates an in situ hydrolysis of the organosilanes (fluorescein, rhodamine B) as the mesoporous silica framework is formed.[22,23] As a result, the organic molecules are well distributed throughout the MSNs. Furthermore, this method can be employed to control the loading and release efficiencies of the system through altering the charge of the silica surface. The loading and release capacities are directly affected by the local electrostatic interactions between the cargo molecules and the intrinsically negatively changed silica surface.[24–26]

In contrast, post-synthetic grafting that primarily covers the exterior nanoparticle surface has been put into extensive practice to mechanize the MSN surface. Control of the mesopore openings enables the MSNs to achieve regulated drug release. Molecular machines are typically bulky supramolecular complexes that are covalently bonded onto the MSNs, and can be triggered for release by either an autonomous intracellular event (pH change or enzymatic cleavage) or an on-command external stimulus (light, heat, or magnetic field).[1,27–30]

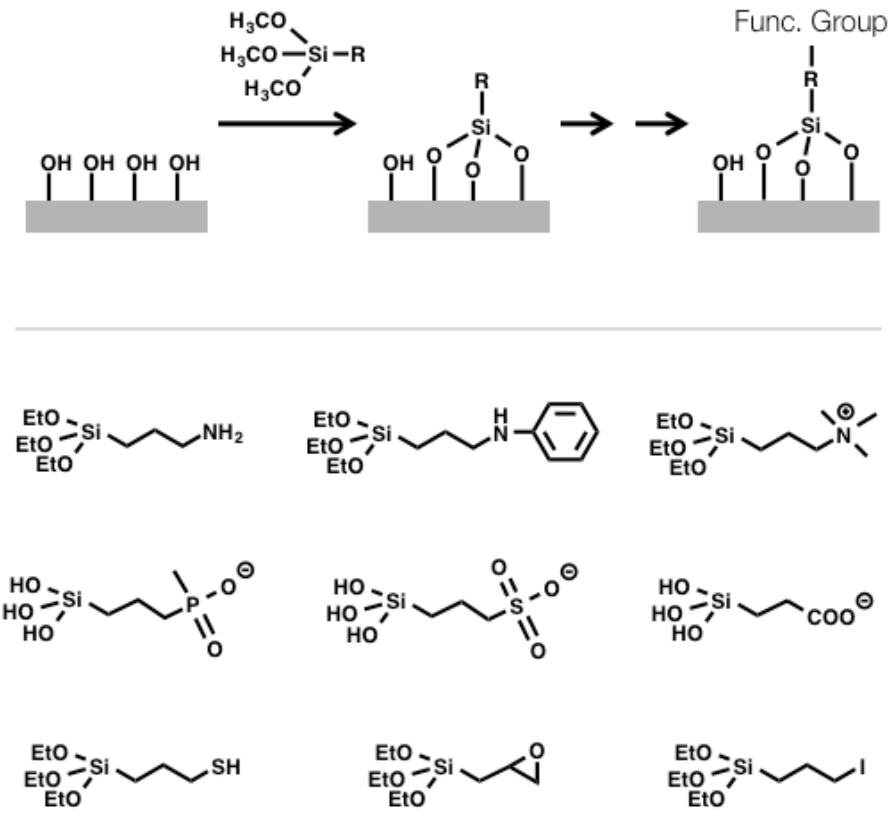

Figure 1.3. A) General scheme of surface functionalizations; B) possible surface functionalizations that are commercially available.

Metal and metal oxide nanocrystals (NCs) can be embedded into the mesporous silica matrix for imaging and magnetic manipulation applications by a surfactant-mediated phase transfer. Hydrophobic NCs are dissolved in chloroform and mixed with an aqueous CTAB solution, where the hydrophobic tail of the surfactant strongly interacts with the hydrophobic ligands on the NCs, while the cationic headgroup of the CTAB render the NCs water-soluble, as the organic solvent is evaporated.[31] This generalized procedure has enabled a variety of core/shell materials (NC@MSN) such as gold, silver, iron oxide, and gadolinium oxide for their various imaging, heating, and manipulation properties.[32–34]

1.3 Loading and Delivery of Cargo

The high surface area to volume ratio of MSNs is ideal for loading cargo into the pores, and additional surface functionalizations can enable a high degree of spatial and temporal control of delivery. A fundamental example is the MSN-assisted delivery of hydrophobic drugs. Hydrophobic drugs inherently have low solubility in water and require detrimental organic solvents for intravenous injection of the free drug. MSNs can be loaded by the diffusion of hydrophobic cargo in a hydrophobic solution, which can be dried to remove the solvent, and the excess cargo can be washed off with water. The silanol groups on the MSN surface render system hydrophilic and suspend well in aqueous media, while their large internal volume enables the safe storage and transport of hydrophobic cargo. Only until the drug-laden MSNs reach the phospholipid bilayer membrane of the cell will the drugs release from the solvation of hydrophobic drugs between the lipid bilayer. Various hydrophobic cargos that have been studied are Ibuprofen, paclitaxel (TXL), and camptothecin (CPT) with reported efficacies' much greater than free drug.[23,35–37]

With the use of nanomachines, the pore openings are controllable to deliver hydrophilic drugs. These mechanized-MSNs can be either activated via internal or external stimuli that are autonomous or remotely controlled. pH-sensitive supramolecular nanovalves are autonomously activated by tuning the chemical sensitivity to the endosomal acidification within the cell. As seen in Figure 1.4, an anisidine stalk binds tightly with bulky circular sugar, alpha-cyclodextrin (α-CD), at pH 7.4 to trap cargo molecules inside the MSNs. As the MSN system enters the endosome, the acidic environment (pH < 6) causes the amine functionality on the stalks to be protonated, and the α-CD cap dissociates, enabling the cargo to diffuse out the pores. The system was further tested for a variety of silica nanoparticles for the loading of Hoechst 33342 (Hoe), as a model cargo. Co-condensation of amine and phosphonate groups within the silica matrix cause the inherently negatively charged silica matrix to become either more positively charged or negatively charged,

respectively. The electrostatic attraction between the cargo and silica affects the loading and release efficiencies.

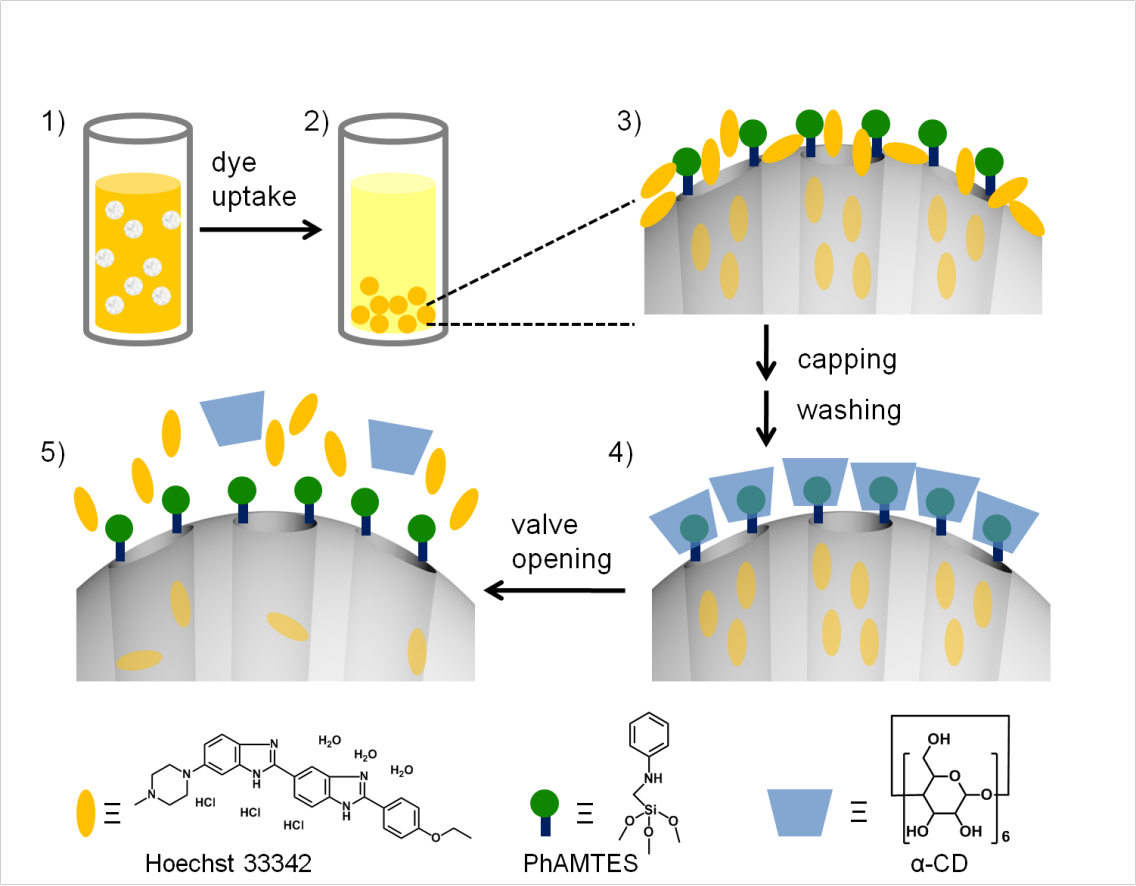

Figure 1.4. Uptake, trapping and release of model cargo (Hoechst 33342, yellow ovals) molecules by nanovalve-gated MSNs. 1) & 2) uptake of dye by MSN via surface adsorption and internalization into pores; 3) magnified particle before capping with α-cyclodextrin and washing; 4) dye trapped in pores after capping and washing off molecules from surface; 5) cargo molecules released by uncapping the pores.[24]

Alternatively, a remote stimulus for nanomachine activation is an attractive method for delivery as it provides non-invasive treatment that has refined control over a selected area, dosage, and exposure time. A notable method is the use of magnetic core-shell MSNs (mag@MSN): when exposed to an oscillating magnetic field, the magnetic cores induce local heating that can be used for hyperthermia or stimulate a thermal nanovalve. Thomas et al accomplished in vitro delivery of

doxorubicin (Dox) to the breast cancer cell line MDA-MB-231 with the application of zinc-doped iron oxide nanocrystals (ZnION) embedded in MSNs with a cucurbit[6]uril-based thermal nanovalve.[29] Once placed in an oscillating magnetic field, the ZnION@MSN induces local heating to open the thermal valve that was once closed at physiological temperatures. Furthermore, this material is also capable of providing T2-weighted magnetic resonance imaging (MRI).

1.4 MSNs as a Drug Delivery System

In order to explore the behavior of MSNs in biological systems and make discoveries at nano-bio interface, various techniques have been developed to examine the particle cellular internalization, nanoparticles' intracellular trafficking, and the particle biodistribution at intact animal level, such as tumor-bearing rodent models. In this regard, MSNs have proven to be able to carry diverse imaging probes. This includes covalent binding and/or encapsulation of various molecules and substrates that are used for fluorescent labeling, contrast agents for magnetic resonance imaging (MRI), and positron emission tomography (PET) imaging.

With easy functionalization of the silanol group on silica surface, MSNs can be covalently labeled with various fluorophores, such as fluorescein isothiocyanate (FITC), rhodamine-B-isothiocyanate (RITC), as well as near-infrared (NIR) dyes. Through the use of fluorescence microscopy including labeling the cellular organelle of interest via specific dye or immunofluorescence staining, many researchers have successfully demonstrated the cellular uptake of MSN and particles' intracellular trafficking. This also includes the study of nanoparticle uptake mechanisms, such as endocytosis and macropinocytosis.

To visualize the biodistribution of the MSN at intact animal level, it is also necessary to label the particles with a NIR fluorophore to allow real time in vivo optical imaging. A NIR dye is particularly preferred because of the low tissue background and photon penetration capability in animal tissues. For example, through the use of NIR fluorescence imaging and elemental Si analysis,

it was demonstrated that DyLight 680 dye labeled MSN coated with the poly(ethylene imine)-poly(ethylene glycol) (PEI-PEG) copolymer was capable of achieving excellent particle retention.[38] In addition to passive particle accumulation at the tumor site, this particle was also capable of entering tumor cells both in vitro and in vivo tumor xenografts to deliver a toxic dose of doxorubicin and induce a higher rate of apoptosis compared to the free drug. MSNs are excreted from animal models via urine or fecal matter, or gradually degrade into nontoxic silicic acid.

In the following chapters, my work will be presented in two major sections: the development of mechanized MSN systems for enhanced drug delivery and the applications of MSNs as a drug delivery system. Chapter 2 discusses the design and optimization of a dual system that contains both pore control and targeting, where the system is tested in vitro and in vivo. The synthesis, mechanization, and in vitro delivery of large pore nanoparticles are reported in Chapter 3. In the second half of the thesis, I will describe the application of MSNs as a drug delivery system in both in vitro and in vivo models. Chapter 4 examines the fate of the MSNs after endocytosis and exocytosis in cells and the composition of the protein corona that evolves on the surface of the MSNs analyzed using MALDI-MS. Chapter 5 demonstrates the in vitro and in vivo delivery of an isoniazid-MSN prodrug system is studied.

1.5. References

(1) Li, Z.; Barnes, J. C.; Bosoy, A.; Stoddart, J. F.; Zink, J. I. *Chem. Soc. Rev.* **2012**, *41*, 2590–2605.

(2) Mamaeva, V.; Sahlgren, C.; Lindén, M. *Adv. Drug Deliv. Rev.* **2013**, *65*, 689–702.

(3) Slowing, I. I.; Vivero-Escoto, J. L.; Wu, C.-W.; Lin, V. S.-Y. *Adv. Drug Deliv. Rev.* **2008**, *60*, 1278–1288.

(4) Pasqua, L.; Cundari, S.; Ceresa, C.; Cavaletti, G. *Curr. Med. Chem.* **2009**, *16*, 3054–3063.

(5) Wu, S.-H.; Hung, Y.; Mou, C.-Y. *Chem. Commun. (Camb).* **2011**, *47*, 9972–9985.

(6) Wu, S.-H.; Mou, C.-Y.; Lin, H.-P. *Chem. Soc. Rev.* **2013**, *42*, 3862–3875.

(7) Botella, P.; Corma, A.; Quesada, M. *J. Mater. Chem.* **2012**, *22*, 6394.

(8) Trewyn, B. G.; Slowing, I. I.; Giri, S.; Chen, H.-T.; Lin, V. S.-Y. *Acc. Chem. Res.* **2007**, *40*, 846–853.

(9) Dunn, B.; Zink, J. I. *Acc. Chem. Res.* **2007**, *40*, 747–755.

(10) Lu, A.-H.; Salabas, E. L.; Schüth, F. *Angew. Chem. Int. Ed. Engl.* **2007**, *46*, 1222–1244.

(11) Yang, P.; Gai, S.; Lin, J. *Chem. Soc. Rev.* **2012**, *41*, 3679–3698.

(12) Vivero-Escoto, J. L.; Slowing, I. I.; Trewyn, B. G.; Lin, V. S.-Y. *Small* **2010**, *6*, 1952–1967.

(13) Chen, Y.; Chen, H.; Shi, J. *Adv. Mater.* **2013**, *25*, 3144–3176.

(14) Stober, W. *J. Colloid Interface Sci.* **1968**, *26*, 62–69.

(15) Yanagisawa, T.; Shimizu, T.; Kuroda, K.; Kato, C. *Bull. Chem. Soc. Jpn.* **1990**, *63*, 988–992.

(16) Di Renzo, F.; Cambon, H.; Dutartre, R. *Microporous Mater.* **1997**, *10*, 283–286.

(17) Beck, J. S.; Schmitt, K. D.; Higgins, J. B.; Schlenkert, J. L. *J. Am. Chem. Soc.* **1992**, 10834–10843.

(18) Cai, Q.; Luo, Z.; Pang, W.; Fan, Y.; Chen, X.; Cui, F. **2001**, *10*, 258–263.

(19) Lee, J. E.; Lee, N.; Kim, H.; Kim, J. J. H.; Choi, S. H.; Kim, T.; Song, I. C.; Park, S. P.; Moon, W. K.; Hyeon, T. *J. Am. Chem. Soc.* **2010**, *132*, 552–557.

(20) Li, D.; Han, Y.; Song, J.; Zhao, L.; Xu, X.; Di, Y.; Xiao, F.-S. *Chemistry* **2004**, *10*, 5911–5922.

(21) Huang, L.; Yan, X.; Kruk, M. *Langmuir* **2010**, *26*, 14871–14878.

(22) Slowing, I.; Trewyn, B. G.; Lin, V. S.-Y. *J. Am. Chem. Soc.* **2006**, *128*, 14792–14793.

(23) Lu, J.; Liong, M.; Sherman, S.; Xia, T.; Kovochich, M.; Nel, A. E.; Zink, J. I.; Tamanoi, F. *Nanobiotechnology* **2007**, *3*, 89–95.

(24) Li, Z.; Nyalosaso, J. L.; Hwang, A. A.; Ferris, D. P.; Yang, S.; Derrien, G.; Charnay, C.; Durand, J.-O.; Zink, J. I. *J. Phys. Chem. C* **2011**, *115*, 19496–19506.

(25) Xue, M.; Zink, J. I. *J. Phys. Chem. Lett.* **2014**, *5*, 839–842.

(26) Tarn, D.; Ashley, C. E.; Xue, M.; Carnes, E. C.; Zink, J. I.; Brinker, C. J. *Acc. Chem. Res.* **2013**, *46*, 792–801.

(27) Meng, H.; Xue, M.; Xia, T.; Zhao, Y.-L.; Tamanoi, F.; Stoddart, J. F.; Zink, J. I.; Nel, A. E. *J. Am. Chem. Soc.* **2010**, *132*, 12690–12697.

(28) Cotí, K. K.; Belowich, M. E.; Liong, M.; Ambrogio, M. W.; Lau, Y. A; Khatib, H. A; Zink, J. I.; Khashab, N. M.; Stoddart, J. F. *Nanoscale* **2009**, *1*, 16–39.

(29) Thomas, C. R.; Ferris, D. P.; Lee, J.-H.; Choi, E.; Cho, M. H.; Kim, E. S.; Stoddart, J. F.; Shin, J.-S.; Cheon, J.; Zink, J. I. *J. Am. Chem. Soc.* **2010**, *132*, 10623–10625.

(30) Lu, J.; Choi, E.; Tamanoi, F.; Zink, J. I. *Small* **2008**, *4*, 421–426.

(31) Liong, M.; Lu, J.; Kovochich, M.; Xia, T.; Ruehm, S. G.; Nel, A. E.; Tamanoi, F.; Zink, J. I. *ACS Nano* **2008**, *2*, 889–896.

(32) Han, L.; Wei, H.; Tu, B.; Zhao, D. *Chem. Commun. (Camb).* **2011**, *47*, 8536–8538.

(33) Ma, M.; Chen, H.; Chen, Y.; Wang, X.; Chen, F.; Cui, X.; Shi, J. *Biomaterials* **2012**, *33*, 989–998.

(34) Cauda, V.; Schlossbauer, A.; Kecht, J.; Zürner, A.; Bein, T. *J. Am. Chem. Soc.* **2009**, *131*, 11361–11370.

(35) Liu, Q.; Zhang, J.; Sun, W.; Xie, Q. R.; Xia, W.; Gu, H. *Int. J. Nanomedicine* **2012**, *7*, 999–1013.

(36) Lu, J.; Liong, M.; Li, Z.; Zink, J. I.; Tamanoi, F. *Small* **2010**, *6*, 1794–1805.

(37) Lu, J.; Li, Z.; Zink, J. I.; Tamanoi, F. *Nanomedicine* **2011**, *8*, 212–220.

(38) Meng, H.; Xue, M.; Xia, T.; Ji, Z.; Tarn, D. Y.; Zink, J. I.; Nel, A. E. *ACS Nano* **2011**, *5*, 4131–4144.

CHAPTER 2

Functional Nanovalves on Protein-Coated Nanoparticles for In Vitro and In Vivo Controlled Drug Delivery

2.1 Abstract

A multifunctional mesoporous drug delivery system that contains fluorescent imaging molecules, targeting proteins, and pH-sensitive nanovalves is developed and tested. Three nanovalve-mesoporous silica nanoparticle (NV-MSN) systems with varied quantities of nanovalves on the surface are synthesized. These systems are characterized and tested to optimize the trade-off between the coverage of nanovalves on the MSNs to effectively trap and deliver cargo, and the remaining underivatized silanol groups that can be used for protein attachments. The NV-MSN system that has satisfactory coverage for high loading and spare silanols is chosen, and transferrin (Tf) is integrated into the system. Abiotic studies are performed to test the operation of the nanovalve in the presence of the protein. In vitro studies are carried out to demonstrate the autonomous activation and function of the nanovalves in the system under biological conditions. Enhanced cellular uptake of the Tf-modified MSNs is seen using fluorescence microscopy and flow cytometry in MiaPaCa-2 cells. The MSNs are then tested using SCID mice, which show that both targeted and untargeted NV-MSN systems are fully functional to effectively deliver cargo. These new multifunctional nanoparticles serve proof of concept of nanovalve functionality in the presence of large proteins and demonstrate another dimension of MSN-based theranostic platforms.

I would like to acknowledge my collaborators, Dr. Jie Lu and Dr. Fuyuhiko Tamanoi for participating in the research presented in this chapter, which has been adopted from the published work, Hwang, A. A.; Lu, J.; Tamanoi, F.; Zink, J. I. Functional Nanovalves on Protein-Coated Nanoparticles for In Vitro and In Vivo Controlled Drug Delivery. *Small* **2014**, 319–328.

2.2 Introduction

Mesoporous silica nanoparticles (MSNs) have shown great promise for biological applications as a drug delivery system because they are nontoxic, easily functionalized, and possess high surface areas.[1–10] MSNs are able to contain and protect therapeutic agents inside the mesopores when the pore openings are controlled by nanovalves. In addition, the exterior surface can simultaneously contain targeting ligands to enhance cellular nanocarrier internalization. Two different approaches for improving the therapeutic delivery of MSNs have been previously shown: mechanized pore control, and targeting ligands. With the diverse silane chemistries available, a variety of nanomachines can be covalently attached to MSNs. These mechanized MSNs are activated only upon a certain stimulus (light, enzyme, redox, magnetic field, pH) to remove the pore capping agent and enable the MSN contents to diffuse out, thereby achieving spatial and temporal control of the delivery of therapeutics.[11–13] pH-sensitive activation is of special interest as delivery can be autonomously activated in vitro and in vivo, due to the acidic conditions of the lysosomal compartments. These nanovalves remain closed at physiological pH (7.4), protecting and trapping the cargo. When the MSNs are endocytosed by cells and enter the lysosome (pH < 6), the pH-sensitive nanovalve will be activated— opening and releasing its contents to provide a stimulus-responsive and autonomous release of therapeutics. Many other MSN-based systems have applied pH-sensitivity to other pore-capping strategies, such as polymers, proteins, and peptides.[14–21]

Nanocarrier delivery can also be enhanced by derivatizing the MSN surface with biologically active targeting molecules (e.g. folate, RGD, transferrin) that increase the endocytosis of MSNs into cancer cells overexpressing receptors for such molecules.[22–25] These molecules incite biological responses from the cancer cell that increases NP endocytosis relative to their untargeted counterparts. Various cancer cell types express upregulated transferrin receptors (TfR) due to the higher iron requirement for cell proliferation.[26,27] Iron is carried into the cell by the 79 kD

transmembrane protein, transferrin (Tf), which can be exploited to increase delivery payload of therapeutics and maintain a localized region of treatment. Our group, as well as others, have successfully shown the enhanced delivery of therapeutics by transferrin-modified nanoparticles that induce receptor-mediated endocytosis in cancer cells.[28–34] We have demonstrated the enhanced delivery of delivery hydrophobic drugs (camptothecin, taxol) with the folate- and transferrin-modified MSNs, relying on the hydrophobic and hydrophilic forces to retain the hydrophobic cargo inside the MSN as it travels through the aqueous cellular media. However, if pore control and targeting functions can be integrated, we can fabricate a delivery system that synergistically delivers hydrophilic cargo in a localized and controlled manner.

In this chapter, the design, fabrication, and operation of a multifunctional MSN delivery system that simultaneously contains fluorescent molecules, targeting proteins, and pH-sensitive nanovalves are presented. The nanovalves can autonomously activate and deliver hydrophilic cargo when exposed to a pH lower than 6 even in the presence of a 79 kD protein. The system is optimized and tested abiotically, demonstrating the successful operation of a nanovalve in the presence of the bulky targeting protein. The transferrin protein slightly impedes the release of cargo, but in vitro testing with human pancreatic cancer cells (MiaPaCa-2) shows an enhanced delivery of doxorubicin (Dox) and cell killing. An in vivo study using SCID mice xenografts was subsequently carried out and showed successful delivery of Dox by using MSNs compared to that of the free drug. However, the transferrin targeting particles did not improve delivery compared to the untargeted particles because the impeded release of cargo counteracted the targeting.

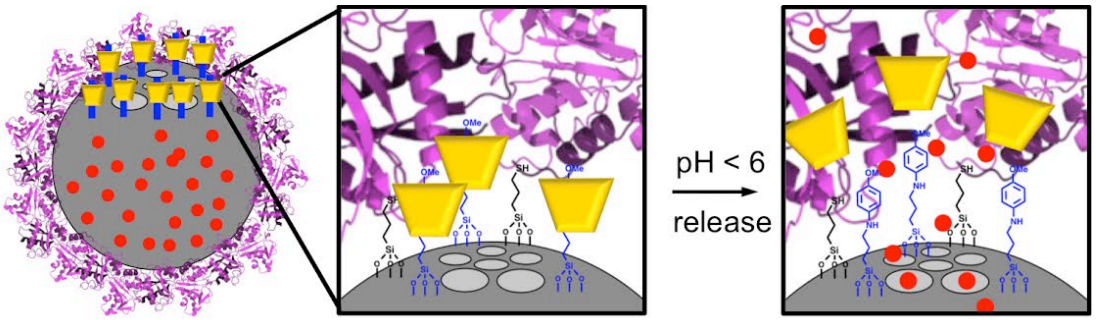

Figure 2.1. Depiction of fully assembled Tf-NV MSN system: when the pH is adjusted to below 6, the nanovalves open, and the MSNs' contents diffuse out in the presence of transferrin.

2.3 Materials and Methods

Materials

All reagents were used as received without further purification. 3-Aminopropyltriethoxysilane (APTES, 99%), *p*-anisidine (≥ 99%), cetyltrimethylammonium bromide (CTAB, 90%), α-cyclodextrin (α-CD, 98%), doxorubicin (98%), fluorescein isothiocyanate (FITC, 90%), bisBenzimide H 33342 trihydrochloride (Hoechst 33342, ≥90%), 4-(2-hydroxyethyl)-1-piperazineethanesulfonic acid (HEPES buffer, 0.05 M), propidium iodide (PI, 95%), tetraethyl orthosilicate (TEOS, 90%), transferrin (Tf, ≥98%) and 3-(trihydroxysilyl)propyl methylphosphonate monosodium aqueous solution (HTMP, 42%) were purchased from Sigma. 3-Iodopropyltrimethoxysilane (IPTMS, 90%) and 3-mercaptopropyltrimethoxysilane (MPTMS, 90%) was obtained from Gelest. Triethylamine (99.5%, EMD), ethanol (200 proof, Pharmaco-AAPER).

General Methods

Transmission electron microscopy (TEM) images were obtained using a JEM1200-EX (JEOL) instrument. UV-vis spectra were collected by a Cary 500 UV-vis-NIR spectrophotometer. The fluorescence release profiles were recorded by an Acton Spectra Pro 2300i CCD and excited by a CUBE 445-40C (Coherent Inc., Santa Clara, CA, USA) laser. ^{13}C CPMAS NMR spectra were obtained by a Bruker DSX-300 MHz Spectrometer with a 4 mm double resonance Bruker probe

head, used with Zirconium oxide 4 mm rotors and Kel-F caps. Thermogravimetric analysis (TGA) was performed by a Pyris Diamond TG/DTA (Perkin-Elmer Instruments). DLS and zeta potentials were measured by ZetaSizer Nano (Malvern Instruments Ltd., Worcestershire, U.K.).

Synthesis of MSNs

An aqueous solution of CTAB (0.25 g, 0.7 mmol) and NaOH (875 μL, 2 M) was heated to 80 °C. TEOS (1.2 mL) was added to the ethanolic solution, and then added to the heated solution drop-wise. After waiting 20 minutes, 300 μL of HTMP was slowly added into the solution and aged for 2 hours. Once the solution was cooled, MSNs were collected by centrifugation, and washed with methanol. The surfactant was removed by refluxing in an acidic methanol solution overnight, washed with MeOH, and subsequently resuspended in the desired solvent. To fluorescently label the MSNs, a separate flask containing FITC (3 mg), APTES (6 μL), and ethanol (dry, 1.5 mL) was reacted under nitrogen for 2 hours. This solution was added to the TEOS prior to being condensed in the hot CTAB solution.

Surface Functionalizations

The nanovalves and protein-coupling agent were covalently attached to the surface of the MSNs by refluxing the silanes and MSNs overnight in dry toluene. In order to synthesize the nanovalve, MSNs were first derivatized with 3-iodopropyltrimethoxysilane and subsequently coupled to *p*-anisidine. For the three nanovalves systems (Nanovalve-1, Nanovalve-2, and Nanovalve-3), differing quantities (15 μL, 25 μL, 30 μL, respectively) of IPTMS were used for 100 mg of MSNs in 10 mL of toluene. The solution was cooled and washed with additional aliquots of toluene. The iodo-functionalized NV-2 MSNs were then suspended in dry toluene (10 mL) and refluxed overnight with *p*-anisidine (120 mg) in the presence of triethylamine (450 μL). The NV-MSNs were consequently scaled with respect to the quantity of IPTMS. Again the solution was cooled and washed with toluene to remove unreacted materials. To prepare for the protein

attachment, the NV-MSNs (100 mg) were subsequently modified with the MPTMS (7 μL) by refluxing overnight in toluene (10 mL) and washed with toluene, methanol, and suspended in water. TGA and solid state NMR confirmed the surface functionalizations.

Cargo Loading and Capping

Cargos (Hoechst, PI, Dox) were loaded into the MSNs by suspending 25 mg of MSNs in a concentrated solution (Hoe and PI: 1 mM, Dox: 4 mg/mL) and left to stir overnight. The nanoparticles were capped by adding α-CD (50 mg) and stirred for 24 hours. The MSNs that did not require any further modifications were thoroughly washed with water until the supernatant ran clear. MSNs that needed Tf-modification were washed only twice to prevent any loss of cargo by excessive washing.

Protein Attachment

Transferrin was covalently attached to the surface of the loaded and capped mercapto-modified NV-MSNs (M-NV-MSNs) by first suspending 25 mg in 1 mL of water. The suspension of nanoparticles was slowly added drop wise to a stirring solution of transferrin and HEPES buffer (1 mg/mL). Finally, a 0.8 M $NaHCO_3$ (0.4 mL) was added for the reaction to proceed. The solution was capped and sealed in foil to prevent light exposure, and let stir for 4 hours at room temperature. The Tf-MSNs were carefully collected by centrifugation and washed several times with HEPES. To confirm the protein was on the nanoparticle, a modified Comassie assay was preformed and analyzed by absorption spectroscopy. Comassie blue typically absorbs at 595 nm, but will shift to 650 nm when exposed to protein. The suspension of Tf-MSNs absorbed at 650 nm but the measurement of the supernatant did not, indicating the Tf is on the MSN and not just in solution. The absorption spectra of the supernatant and suspension of MSNs with the Comassie assay were not red-shifted.

Abiotic Studies

To confirm the function and operation of the nanovalves, aqueous release studies were preformed on the MSN systems. Samples loaded with cargo (5 mg) were carefully placed in the corner of a cuvette and filled with water (7 mL). A probe beam (448 nm) was used to excite the emission of the cargo being released in the bulk water and its fluorescence was continuously monitored by a spectrophotometer in real time. Once a flat baseline was obtained to show no leakage, the solution was adjusted to a pH of 5.5 to activate the acid-sensitive nanovalves. The supernatant of the solution was measured by UV-vis spectroscopy to calculate the loading capacity and to normalize the different release profiles.

Cell Culture

Human cancer cells, MiaPaCa-2, were obtained from the American Type Culture Collection and were maintained in Dulbecco's modified Eagle's medium (DMEM) (GIBCO) supplemented with 10% fetal calf serum (Sigma, MO), 2% L-glutamine, 1% penicillin, and 1% streptomycin stock solutions. The media were routinely changed every 3 days, and the cells were passaged by trypsinization before confluence.

Fluorescence Microscopy

The MSNs emit a green fluorescence when excited at 470 nm because of fluorescein dye co-condensed within the silica matrix. Acridine Orange (AO) was used to monitor the acidic intracellular organelles. Cells were cultured on a Lab-Tek chamber slide system (Nalge Nunc International) overnight. After being incubated with MSNs for 3 hours, the cells were washed with PBS, and incubated with 6 mM AO for 1 hour in DMEM without phenol red and washed with PBS, then examined with confocal microscopy (λ_{ex} = 470 nm) (Carl Zeiss LSM 310 Laser Scanning Confocal microscope). The cellular uptake and subcellular distribution of Doxorubicin-loaded nanovalves can be easily monitored using fluorescence microscopy since Dox exhibits bright red

fluorescence under laser stimulation (excitation at 480 nm; emission maximum at 560-590 nm). MiaPaCa-2 cells were incubated with either Dox-loaded NV-MSNs or NV-MSNs for 3 hours or 12 hours at 37 °C and the fluorescence distribution was examined using a fluorescent microscope.

Cell Death Assay

The cytotoxicity assay was performed using a cell counting kit from Dojindo Molecular Technologies, Inc. Briefly, cancer cells were seeded in 96-well plates (5000 cells/well) and incubated in fresh culture medium at 37 °C in a 5% CO_2/95% air atmosphere for 24 hours. The cells were then washed with PBS, and the medium was changed to a fresh medium with indicated NV-MSNs at indicated concentrations. After the indicated incubation period, the cells were washed again with PBS. Then, 10% WST-8 solution in 100 μL of DMEM was added to the wells, and incubated for another 2 hours. Finally, the absorbance of each well was measured at 450 nm with a plate reader. Since the absorbance is proportional to the number of viable cells in the medium, the viable cell number was determined using a previously prepared calibration curve (Dojindo Co.).

Flow Cytometry

Flow cytometric analysis was used to detect the fluorescent signal of MSNs internalized by human cells. The cells treated with MSNs for 24 hours were collected, washed with PBS, and analyzed with a fluorescence-activated cell sorter (Caliber, Becton Dickinson).

Establishment of Human Cancer Xenograft

MiaPaCa-2 (5×10^6 human pancreatic cancer cells) were collected in 0.2 mL DMEM, and s.c. injected into the right lateral back of the SCID mice (Charles River). Mice were randomly divided into treatment or vehicle groups in each experiment after the tumors of approximate 3 mm in diameter were palpable.

Biodistribution of NV-MSNs

Four SCID mice bearing subcutaneous tumors approximately 8 mm in diameter were injected via the tail vein with NV-MSNs loaded with doxorubicin suspended in saline solution. After 4 hours and 24 hours, the mice were anesthetized, placed in the chamber of a Maestro 2 *in vivo* imaging system (CRi, MA), and optic light and green fluorescent images were obtained. After euthanasia with CO_2, the tumors were collected, embedded, frozen, processed to 4 μm slides by our Tissue Processing Core Lab (TPCL, UCLA). All slides were then analyzed under a fluorescent microscope.

In Vivo Tumor Growth Assay

Twenty-five SCID mice with established xenografts of MiaPaCa-2 were randomly divided to 5 groups (n=5), and the intraperitoneal injections (0.5 mg/0.2 mL per mouse) began when the average tumor diameter reached 3 mm (14^{th} day after inoculation). Animals in the first group received saline solution as control (Group 1). Group 2 was treated with Dox only. Group 3 was treated with plain NV-MSNs without loading. Group 4 was treated with NV-MSNs loaded with doxorubicin (the final concentration of Dox is the same as Group 2). Group 5 was treated with Tf-NV-MSNs loaded with Dox. All injections were performed twice per week until the end of the experiment (the 28^{h} day). Tumor volume and body weight were monitored every other day, and tumor volume was calculated using the following formula: tumor volume = (4 / 3) × 3.14 × (L / 2 × W / 2 × W / 2), where L is the length and W is the width of the tumor. At the final day, all mice were sacrificed and subjected to autopsy. Blood was collected for serological and hematological examination, and the organs were analyzed by a pathologist for histopathological examination.

Statistical Analysis

All results are expressed as means ± SD. Statistical comparisons were made using Student's t test after analysis of variance. The results were considered significantly different at P value <0.05.

2.4 Results and Discussion

Design, synthesis, and testing of pH-responsive nanovalves

In order to design a system that includes both targeting and pH-sensitive functionalities, a simple and sensitive nanovalve system that could be easily integrated into a well-established targeting scheme was chosen.[35] The nanovalve is composed of an aniline-based stalk that is grafted onto the surface of the nanoparticle, which forms an inclusion complex with α-cyclodextrin (α-CD) via hydrophilic and hydrophobic interactions to seal cargo inside the pores at neutral conditions. When exposed to acidic conditions, the phenyl amine is protonated ($pK_a \approx 6$) and the binding constant between the stalk and α-CD dramatically decreases, causing the cyclic sugar to de-bind and allow the cargo to diffuse out of the pores.

The first task was to optimize the nanovalve-MSN system in the presence of the targeting agent. There are a limited amount of silanol groups on the external surface of the MSNs, which made it necessary to adjust the relative surface coverage to simultaneously accommodate the nanovalve and a protein-coupling agent. Determining the appropriate amount of nanovalves necessary for sufficient pore capping and targeting was crucial in order for the two modalities to work synergistically. Therefore, three different MSNs systems (Nanovalve-1, Nanovalve-2, Nanovalve-3) were synthesized that contained 50%, 85%, and 100% of the concentration for maximum surface coverage of nanovalves (Scheme 2.1). The nanovalves were grafted onto the surface via silanol exchange in dry toluene.

Scheme 2.1. Synthetic schemes of acid valve assembly and incorporation of targeting agent. NV-MSN denote particles that are modified with nanovalve only, and Tf-NV-MSN are particles that have both transferrin and nanovalve derivatizations.

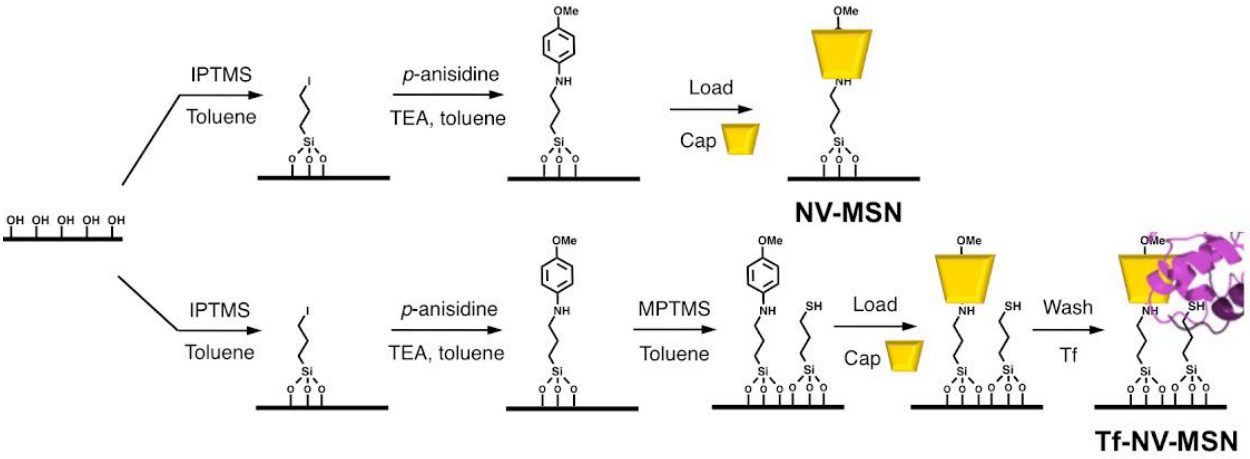

To confirm the nanovalve attachment and determine quantity of surface coverage, solid-state ^{13}C and ^{29}Si CPMAS NMR spectroscopy and thermogravimetric analysis were preformed. The ^{13}C CP/MAS SSNMR spectrum shows characteristic peaks in the aliphatic region from the propyl and methoxy groups, and four phenyl peaks in the aromatic region (Figure 2.2). Analysis of the ^{29}Si CP/MAS SSNMR spectrum show peaks in the T and Q regions, which are attributed to the silicon atoms in the bulk silica (Q region) and the silicon atoms from the surface-functionalized nanovalves (T region) (Figure 2.3). TGA showed the quantitative differences of the surface coverage, which confirmed the various quantities used in the synthesis of the nanovalve (NV-1, 6.98; NV-2, 7.82; NV-3, 8.27 % wt). As expected, the more thread used in the synthesis, the higher the weight percentage, and thus the greater number of nanovalves on the particle surface.

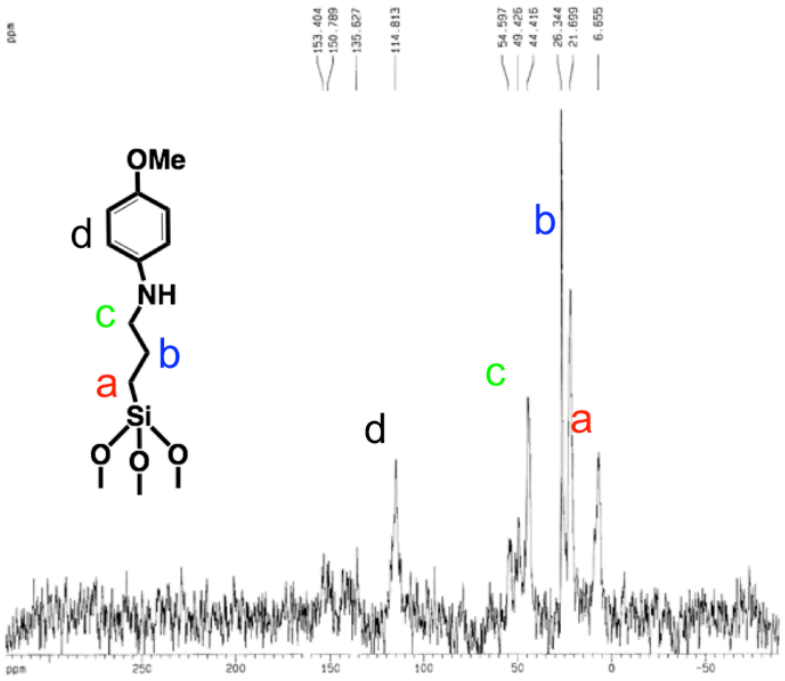

Figure 2.2. ^{13}C CP/MAS NMR of NV-MSNs show three peaks in the aliphatic region, that are indicative of the 3-carbon chain in the stalk, and peaks in the aromatic region correspond to the aromatic phenyl ring.

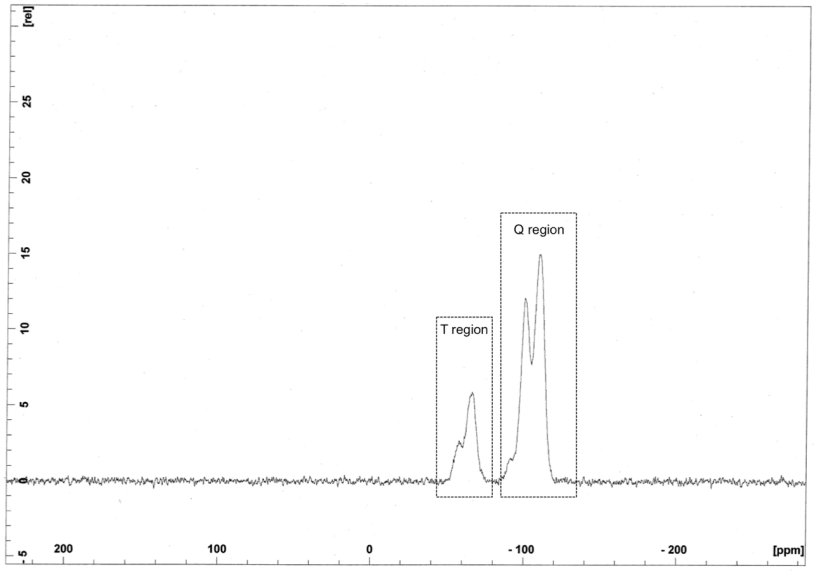

Figure 2.3. ^{29}Si CP/MAS NMR of NV-MSNs show peaks in the Q and T region, which can be respectively attributed to the bulk silica and silicon atoms grafted onto the surface of the MSNs.

The new NV-MSN systems were loaded with doxorubicin (Dox), a water-soluble and widely used anticancer drug, to determine the behavior of the nanovalve as a function of surface coverage. Dox has a bright red fluorescence under laser stimulation (λ_{ex} = 480 nm; λ_{em} = 560-590 nm), which makes it convenient to detect in release experiments. After loading, the nanoparticles were capped with α-CD and the excess dye was washed away with water until the supernatant was clear. Dox functions by inhibiting the progression of the enzyme topoisomerase II and can induce severe adverse effects such as life threatening heart damage. Many approaches to deliver Dox to target cancer cells in order to reduce its toxicity have been investigated, such as liposome-encapsulated forms Doxil, Caelyx, and Myocet.[36,37]

The three NV-MSN systems were tested abiotically using real-time continuously monitored fluorescence spectroscopy. To measure the amount of cargo that could be trapped by the different concentrations of nanovalves as well as to determine each sample's loading capacity, small amounts of dry Dox-loaded NV-MSNs were placed in a cuvette that was then filled with water. The fluorescence of the supernatant was monitored as a function of time before and after acidification. The initial flat baseline shows no increase of fluorescence (hour 0-1), indicating that the cap is tightly secured onto the stalk and there is no premature release of cargo (Figure 2.4 A). The nanovalve is activated in the aqueous solution by adjusting the pH to 5.5, which causes the amine groups on the nanovalves to become protonated and thus decrease the binding constant between the stalk and α-CD. The bulky CD dissociates from the stalk and enables the cargo to diffuse out. The movement of the cargo from the particles into the bulk solution is quantified by monitoring the increase of fluorescence of the supernatant in real time. When each release was complete, an aliquot of the supernatant was removed and analyzed by UV-vis. The quantity of Dox released in the pH = 6 solution was calculated using Beer's law, and these data were later used to normalize the release profiles to one another. The release capacities were dependent on the quantity of surface

functionalizations on the MSNs. The NV-3 had the highest release capacity of 1.2% wt, while NV-1 had the lowest (0.2% wt), and sample NV-2 had a release capacity of 0.5% wt.

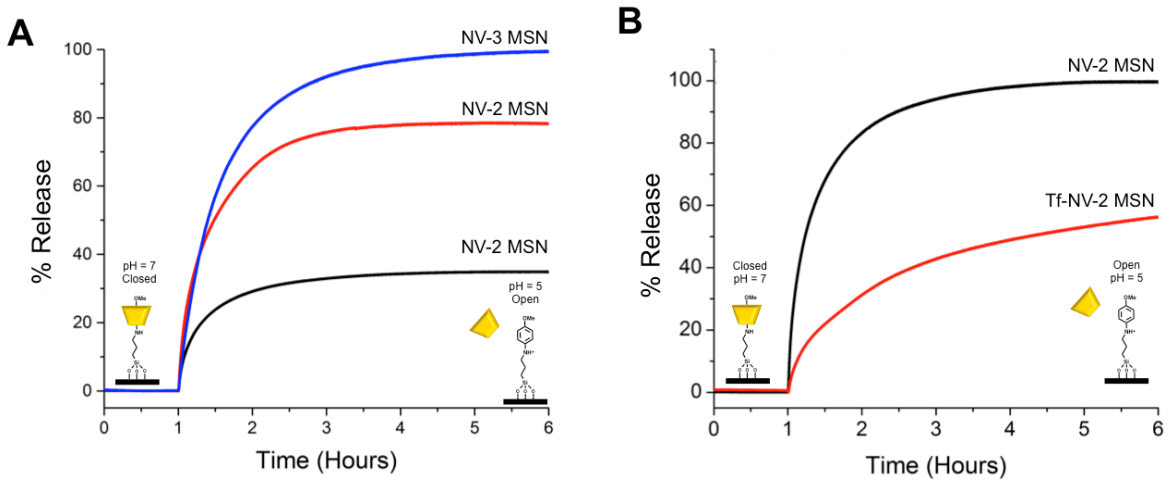

Figure 2.4. A) Release profiles for particles with 50%, 85%, and 100% acid nanovalve surface coverage (respectively NV-1, NV-2, and NV-3). Capacity is dependent on the amount of surface coverage to hold cargo. B) Release of NV-2 MSN delivery systems with and without protein modification. Protein presence hinders release of cargo. All pH activations are performed at pH of 5.

The quantity of cargo released from the NV-MSNs was directly related to the extent of nanovalves on the surface and the rate was dependent on the amount of cargo released. In order to be effective at holding cargo, the nanovalves must block both ends of the hexagonal pore openings on the MSNs. As the surface coverage of nanovalve decreased, the loading capacity and release rate were lowered because there were fewer capped pore channels to hold cargo. The trend of release rate was NV-3 > NV-2 > NV-1, which corresponds to the relationship between nanovalve surface coverage and loading capacity of the MSN. Complete release of NV-1 is achieved in 3.5 hours, evidenced by the intensity. The profile of NV-2 begins to plateau at 5 hours, and the NV-3 sample still has a nonzero slope at hour 6. It can be concluded that the new NV-MSN systems work, but suffer consequences from decreased quantity of nanovalves on the surface. NV-2 has a release that is 20% less than that of the full coverage sample, but NV-1 is only about 35% (NV-3). The NV-2

MSN system was chosen to be the optimum value to be able to accommodate the Tf while maintaining a relatively large release capacity for cargo.

Integrating pH-responsive nanovalves and Tf targeting into MSN system

The targeting component was attached to the chosen NV-2-MSN system by functionalizing the particles with the thiol-terminated silane, 3-mercaptopropyltrimethoxysilane (MPTMS), to serve as the protein-coupling agent. The M-NV-MSNs were loaded with Dox and capped before the protein was attached. Finally, transferrin (Tf) was covalently bonded to the nanoparticle by the thiol-disulfide exchange. The thiol-terminated particles are suspended in water, added drop-wise to a protein solution, and adjusted to a basic pH with $NaHCO_3$. Under basic conditions, the thiolate anion forms and exchanges readily with the disulfide bonds in the protein.[38] By attaching the Tf last, the denaturation of the protein is limited because the synthetic steps to attach the nanovalves would expose the protein to non-ideal conditions, such as nonpolar solvents and heat.

The assembled Tf-NV-MSNs were characterized by three methods. TEM imaging showed that the porous structure of the nanoparticle was preserved even after extensive surface modifications. Because electron microscopy cannot image small molecules or proteins on the particles' surface without staining, the apparent diameters of the nanoparticles did not appear to change after the surface modifications (Figure 2.5). Dynamic light scattering (DLS) was performed to ensure the nanoparticles were well suspended and monodisperse for biological studies. DLS showed the NV-MSN sample had an average hydrodynamic diameter of 108 nm, while the protein-modified MSN had a diameter of 117 nm (Figure 2.6). The increase in the average hydrodynamic radius (9 nm) is consistent with the addition of a protein (~ 6 nm) and the nanovalve on the surface of the MSN. Thermogravimetric analysis (TGA) shows the total surface coverage of both protein and assembled nanovalve was approximately 9% wt and degrades between temperatures 120 and 400 °C.

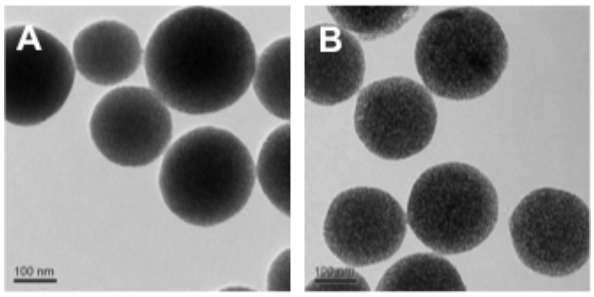

Figure 2.5. TEM images of A) before surface modification and B) after surface modifications.

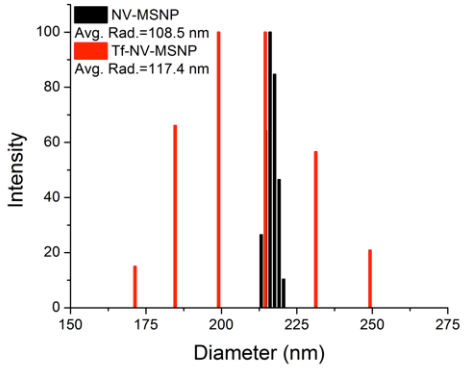

Figure 2.6. DLS data for NV-MSN and Tf-NV-MSNs. Average particulate size does not change greatly, however Tf-NV-MSNs have a broader range of sizes due to the protein modification.

To verify the presence of Tf on the nanoparticles, a modified Bradford assay was performed. Nanoparticles with and without protein modification were treated with the dye Comassie Brilliant Blue and the samples' supernatants were analyzed by UV/vis absorption spectroscopy. The dye primarily exists in its green form (λ_{max} = 650 nm), but will bind to the protein, shifting the dye to its a blue form (λ_{max} = 595 nm). The absorption spectrum of aqueous Comassie Brilliant Blue shows two peaks at 470 and 650 nm that are indicative of the two unbound forms, while the peak at 595 nm for its bound form is absent. Upon adding a suspension of Tf-MSNs, the solution turned blue and the absorption spectrum only exhibited a broad peak at 595 nm, diagnostic of the dye binding to protein (Figure 2.7). Moreover, the supernatant of the Tf-MSN solution was measured and there was a negligible amount of absorbance at 650 nm. As a control, unmodified MSNs were also assayed

and did not exhibit any bound protein peaks in the spectrum. These data suggest that Tf proteins are on the MSNs and are not in solution.

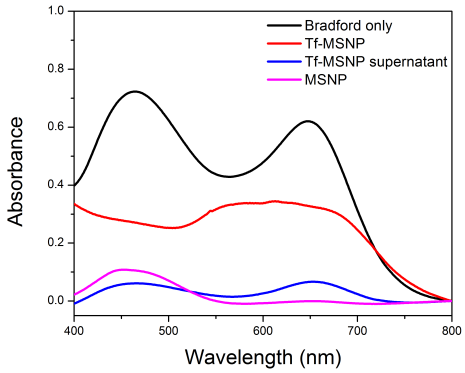

Figure 2.7. UV-vis spectra of Comassie blue assays: initial solution has peaks at 460 and 675 nm, while Tf-MSNs have broad peak around 600 nm. Supernatant of Tf-MSNs solution has small absorption around 450 and 650 nm, MSNs in assay have small absorption at 450 nm.

In order to understand the behavior and operation of the nanovalve in the presence of the Tf protein, abiotic studies were performed using the aforementioned fluorescent spectroscopic technique. After the pH was adjusted to 5.5, the release profile Dox was obtained. Profiles of the MSNs with and without protein modification show successful release of Dox that confirm the nanovalves' operation with large proteins on the surface.

The two sets of nanoparticles show successful activation of the nanovalve with release of cargo and demonstrate different release kinetics as seen in Figure 2.4 B. The Tf-modified NV-2-MSNs exhibit some impedance of cargo diffusion from the pores— the release rate at slightly acidic pH is considerably slower than that of the NV-2-MSNs. The cargo is not fully released even after 13 hours, which can be attributed to the protein delaying the diffusion of the cap and cargo from the pores. The MSNs with only the nanovalve have a faster rate of release; 90% of the cargo is in the solution after 4 hours (Figure 2.4 B, black trace). Because Dox is positively charged, the cargo can be

electrostatically adsorbed to the surrounding proteins, slowing and hindering the diffusion process as the cargo leaves the pore. We have also observed a similar effect in samples with both polymer coatings and nanovalves on the silica surface.[39]

However there is a negligible difference in the overall loading capacities of both materials. Dox-loaded nanoparticles were treated with a strong acidic solution (pH = 1) to release the MSNs' entire contents. The solution was buffered back to neutral pH, the UV-vis absorption spectrum of the supernatant was measured, and the concentration of the drug was calculated via Beer's law. The Dox-loaded NV-MSNs have a loading capacity of 2.5 % wt, while the Tf-NV-MSNs have a loading capacity of 3.8 % wt (Figure 2.8). The loading capacity of the Tf-NV-MSNs is slightly higher, which can be attributed to the modified loading method that is used to protect the transferrin.

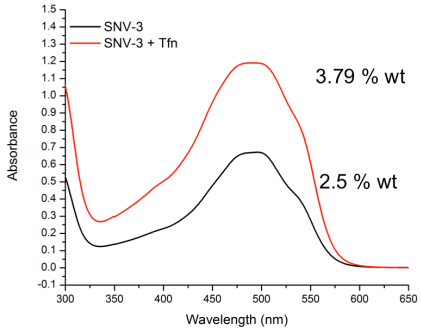

Figure 2.8. UV-vis spectra of supernatant of Dox-loaded MSN samples released in pH 6 solution, which are used to calculate the release capacity of the samples.

Enhanced Cellular Uptake of Tf-modified MSNs

After the MSNs were optimized as described above, in vitro studies were carried out to test the efficacy of the targeting agent in a pancreatic cancer cell line, MiaPaCa-2. The MSNs were synthesized and fluorescently labeled with fluorescein via a co-condensation method. Cells were incubated with MSNs with and without Tf modification for 24 hours, and subsequently washed with phosphate-buffered saline (PBS) solution to remove the excess MSNs. The cells were imaged via

fluorescence microscopy, which showed that the MSNs (green fluorescence, fluorescein) were located within the cell (red fluorescence, WGA-Alexa Fluor 594 stain) (Figure 2.9 A). The Tf modification on the cellular uptake resulted in enhanced uptake, shown qualitatively by the increase of cellular fluorescence by the Tf-targeted MSNs. Flow cytometry was performed to confirm and quantify the observed enhanced uptake of Tf-modified nanovalves inside the MiaPaCa-2 cells. As shown in Figure 2.9 B, the amount of internalized Tf-MSNs is significantly higher than that of the MSNs without targeting agent. These results are explained by the overexpression of transferrin receptor (TfR) on the MiaPaCa-2 cancer cells, which facilitates the recognition and binding of the Tf-modified MSNs, thereby increasing the intracellular uptake.

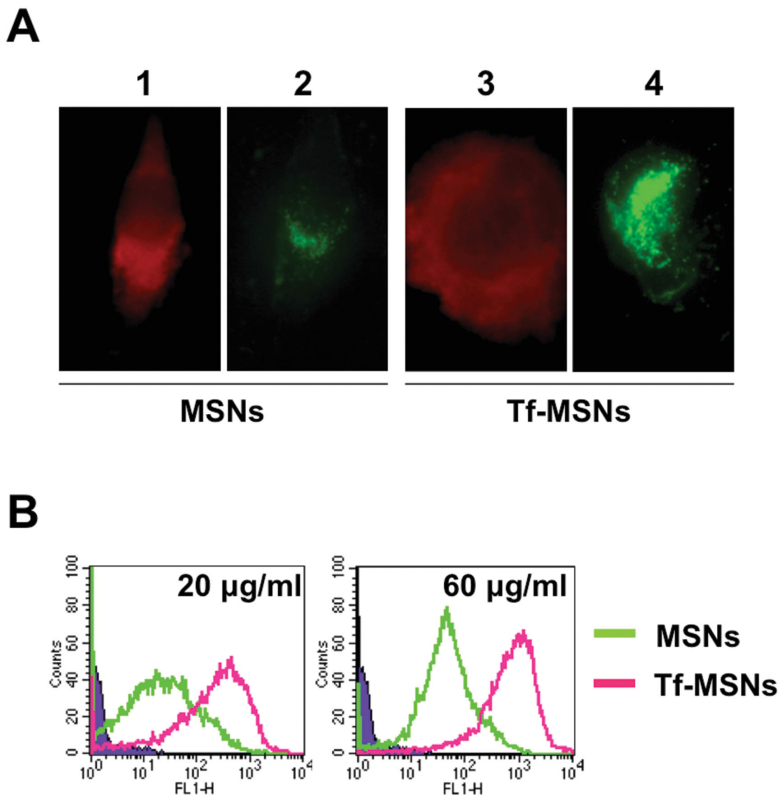

Figure 2.9. A) Fluorescence microscopy images of cell (panels 1, 3) and MSNs (panels 2, 4) show increased fluorescence of the Tf-MSNs than the untargeted MSN, indicative of higher endocytosis of Tf-MSN; and B) Flow cytometry of targeted and untargeted MSNs at two different concentrations show Tf-MSNs have a significantly higher uptake.

Intracellular release of fluorescent dyes

The MSNs were loaded with fluorescent model cargo molecules to demonstrate the autonomous activation and function of the nanovalves in biological conditions, after the enhanced cellular uptake of Tf-modified MSNs was established. For this purpose, two fluorescent dyes were used. Membrane impermeable propidium iodide (PI), and membrane permeable Hoechst 33342 (Hoe) were used as guest molecules in MSNs with and without the targeting protein. As PI is impermeable to lysosome membranes, it is unable to stain the cell nuclei if the nanovalves open inside the acidic lysosomes. Conversely, once Hoe is released, it can cross the lysosomal membrane easily and stain the nuclei. If PI is released into cytosol, it will stain the nuclei by intercalating into the DNA. Two cell lines (HFF, PANC-1) were cultured overnight with dye-loaded MSNs on a Lab-Tek chamber slide system (Nalgel Nunc International) to allow for cellular uptake, cargo release, and staining. As shown in the Supplemental Information, the Hoechst dye was released and the cell nuclei were stained bright blue, for the both sets of MSNs (Figure 2.10 A). It should be noted that the Tf-NV-MSNs show a brighter staining that is indicative of enhanced uptake by targeting. Alternatively when PI is employed as cargo, there are no observable cell nuclei staining with the same length of treatment. Even though the acidic environment of the lysosomal compartments causes release of PI, all of the released PI molecules are confined in the lysosomes due to the membrane impermeable nature of PI.

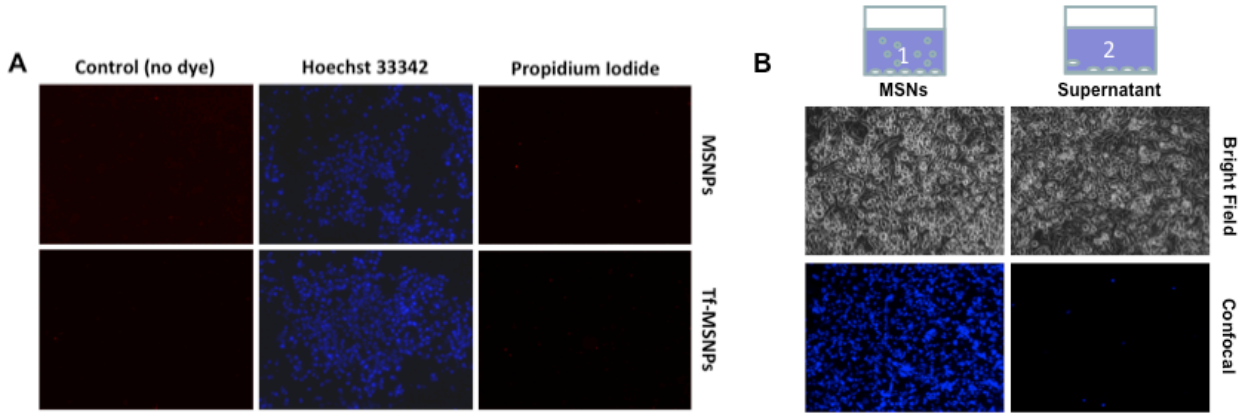

Figure 2.10. A) Fluorescence imaging of MSNs with Hoe and PI cargo, showing no leakage of dye. Hoe is membrane permeable and can stain of the nuclei (blue), whereas particles loaded with PI cannot (red). B) Bright and fluorescence images of cells incubated with Hoe-loaded MSNs and the MSNs' supernatant. The nuclei are stained only with treatment of Hoe-loaded MSNs, which demonstrate a non-leaky MSN system.

It is also possible the observed nuclei staining with Hoechst-loaded MSNs simply might be due to leakage of dye from the pores before the cellular uptake even occurs. To rule out this possibility, MiaPaCa-2 cells were incubated with dye-loaded MSNs for 3 hours (Chamber 1); the supernatant was collected, and then used to treat cells in another chamber (Chamber 2) for 30 minutes before being subjected to fluorescence microscopic examination. If the dye had leaked from the MSNs before their cellular uptake, the dye should be in the supernatant and would be able to stain the cells in Chamber 2. In Figure 2.10 B, the cells in Chamber 1 show brightly stained nuclei but there is no detectable staining in Chamber 2, proving that leakage is negligible.

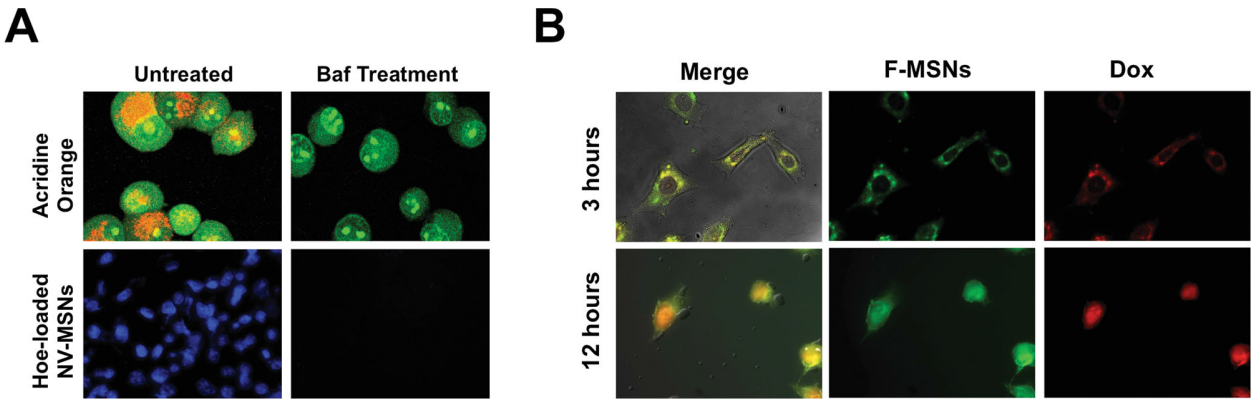

Figure 2.11. A) Cells (green) are treated with acridine orange to detect acidic organelles (orange). Once exposed to Bafilomycin (Baf), the organelles are no longer acidic and no orange fluorescence is seen. Hoechst-loaded NV-MSNs show nuclear staining of cells (blue) but after Baf treatment, the NVs are not activated and no staining is seen. B) Confocal images of Dox-loaded MSNs: the green channel represents the MSNs and the red channel shows doxorubicin. At 3 hours, the Dox is contained in the MSNs located inside the cell, but at 12 hours the nanovalves have been activated and the Dox has begun to stain the cell nuclei red.

These experiments prove that the NV-MSNs can release cargo in the lysosomes and stain the nuclei. However, the intracellular dye release observed is not necessarily due to the lower pH environment in the lysosomes; other unexpected stimuli could exist within a complex biological system. To prove the nanovalve activation is due to the acidic environment of the lysosome, the acidity of lysosomes was altered by using a proton inhibitor Bafilomycin A1 (Baf). Cells were treated with 160 nM Baf for 6 hours before the dye-loaded NV-MSNs were added to the cells. To examine the effect of Baf on the de-acidification of lysosomes, acridine orange (AO) staining was performed (Figure 2.11 A). AO is a fluorescent weak base that is frequently used as a probe for monitoring the acidification of organelles. In neutral or alkali environments, it emits a green fluorescence but when exposed to acidic compartments, it is ionized and it emits red light. In the untreated cells, red fluorescence was observed inside discrete cytoplasm organelles, indicating that the AO had accumulated in acidic organelles. However, the red fluorescence dramatically decreased after 6 hours

of Baf treatment, indicating that the Baf had increased the pH of the lysosomes in the MiaPaCa-2 cells. NV-MSNs loaded with Hoechst dye were added to the cells and incubated for an additional 12 hours before examination by fluorescence microscopy. As shown in Figure 2.11 A, the treatment with Baf completely prevented the release of Hoechst from nanovalves, demonstrated by the lack of nuclear staining, as compared to the bright staining of the cells unexposed to Baf. This directly proves that the intracellular release of dye from MSNs was triggered by the acidity of the lysosomes.

Intracellular Anticancer Drug Release from Nanovalves

The previous experiments with fluorescent cargoes clearly demonstrate the pH-activated intracellular cargo release. To prove the synergistic cell killing effects of applying both pore control and targeted delivery, Dox was loaded into the NV-MSNs and tested in cancer cells. MiaPaCa-2 cells were incubated with fluorescein-labeled NV-MSNs for a range of 3 to 24 hours, washed with PBS, fixed with cold methanol, and examined by fluorescence microscopy. The NV-MSNs (green fluorescence) incubated for 3 hours primarily co-localize with Dox (red fluorescence) and are distributed within lysosomes, primarily in the perinuclear areas (Figure 2.11 B). However after 12 hours of incubation, the red fluorescence of Dox no longer co-localized with green NV-MSNs but was observed in the nuclei. These images are indicative of the drug exiting the lysosome and entering the nucleus, which is essential for the drug to be effective at cell killing. Subsequently, the MSN systems were tested to determine if the Tf targeting agent and nanovalve functionalizations would deliver Dox more efficiently than with only the nanovalve on the surface. MiaPaCa-2 cells were treated with NV-MSNs (with and without transferrin) loaded with or without Dox for 72 hours. The cells that survived were counted with a WST-8 cell counting kit. Figure 2.12 shows the MSNs modified with the nanovalve alone did not induce proliferation suppression to cells, while Dox-loaded NV-MSNs showed a significant cytotoxic effect. The Tf-NV-MSNs were within statistical error at increasing cell cytotoxicity. The nanovalve is able to autonomously open and

deliver Dox in the presence of the bulky protein, while transferrin is increasing the cellular uptake of the MSNs to focus its delivery. These data demonstrate the synergistic effects at work to deliver cargo more effectively.

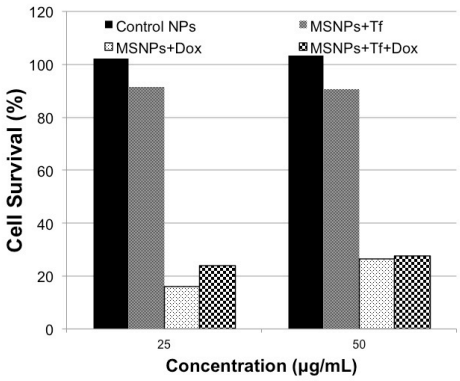

Figure 2.12. Cell proliferation assay was carried out with MiaPaCa-2 to observe the efficacy of the Tf-NV-MSN drug delivery system. The MSN-systems without drug did not induce proliferation suppression to cells at all. The Dox-loaded NV-MSNs and the Dox-loaded Tf-NV-MSNs were similarly effective concentrations.

In vivo Anticancer Effect of Doxorubicin-Loaded Nanovalves

Successful in the in vitro model, the MSN system was tested in an in vivo model to understand the effectiveness of the nanovalve and targeting functions in an animal model. To establish human cancer xenografts, 5 x 10^6 MiaPaCa-2 cells were subcutaneously injected into the right lateral abdominal wall of the SCID mice. Mice were randomly divided into the treatment groups in each experiment after the tumors approximately 3 mm in diameter were palpable. Four mice bearing subcutaneous tumors approximately 8 mm in diameter were injected via tail vein with Dox-loaded MSNs, suspended in saline solution. After 4 and 24 hours, the mice were anesthetized, placed in the chamber of a Maestro-2 in vivo imaging system, and optic light and green fluorescent images were obtained. As shown in Figure 2.13 A, a strong green fluorescence signal was detected in tumors of the mice treated with MSNs at 4 hours and 24 hours after the injection, indicating the accumulation of nanoparticles in tumors.

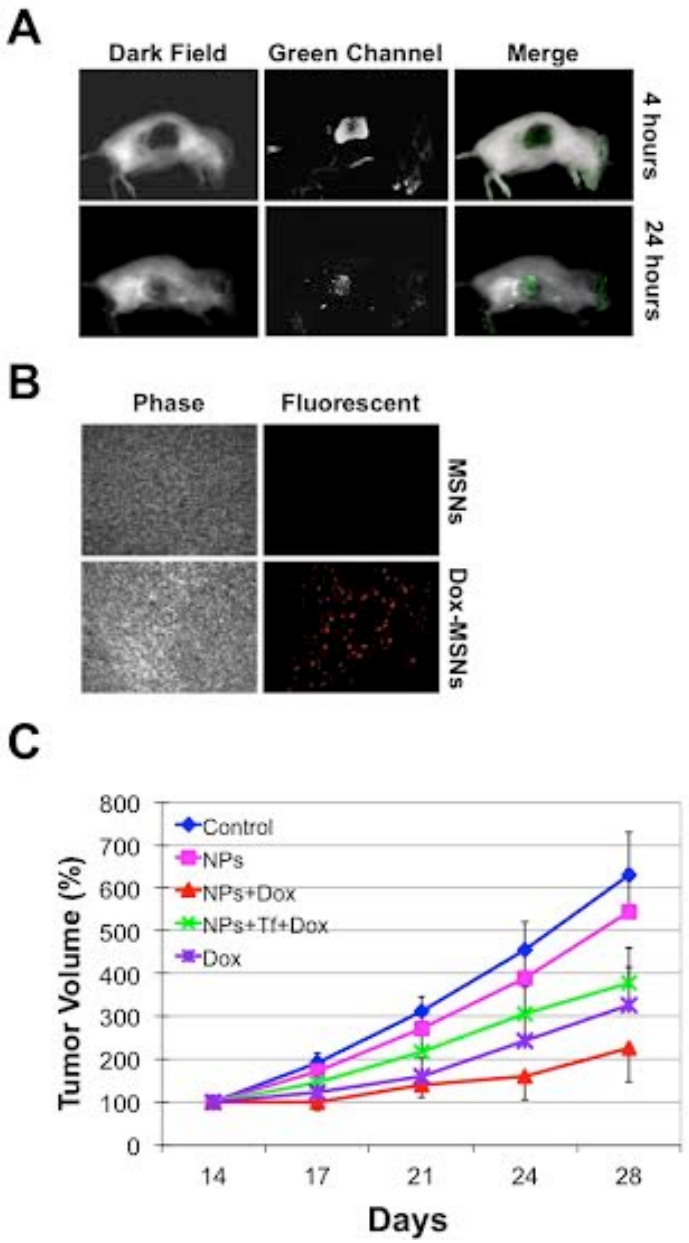

Figure 2.13. A) Biodistribution of MSNs in mice with xenograft tumors. SCID mice bearing subcutaneous human pancreatic tumors were injected via tail vein with MSNs. 4 and 24 hours later, the mice were anesthetized, subjected to Maestro 2 in vivo imaging system for green fluorescent (MSNs) images. B) Tumors were collected, processed, and analyzed with a fluorescence microscope. Red fluorescence indicates doxorubicin in the tumors. C) 25 SCID mice with established xenografts of MiaPaCa-2 were randomly divided to 5 groups (n=5), and the intraperitoneal injections of MSN solutions began once the average tumor diameter reached 3 mm (14th day after inoculation). All injections were done twice per week until the end of the experiment (the 28th day). The average tumor volumes are shown as means ± the standard deviation (SD).

After euthanasia, the tumors were collected and all tissues were analyzed by fluorescence imaging. The red fluorescence signal was observed from the tumors in the mice treated with Dox-loaded MSNs, but no signal was observed in mice treated with unloaded MSNs (Figure 2.13 B). Next, 25 SCID mice with established xenografts of Mia-PaCa-2 were randomly divided into 5 groups (n = 5), and intraperitoneal injections of MSN solutions began after the average tumor diameter reached 3 mm (14^{th} day after inoculation). Animals in the first group received saline solution as control, Group 2 was treated with free Dox, Group 3 was treated with unloaded NV-MSNs, Group 4 was treated with NV-MSNs loaded with Dox, and Group 5 was treated with Tf-NV-MSNs loaded with Dox (the final concentrations of Dox were the same as Group 2). All injections were done twice per week until the end of the experiment (the 28^{th} day). The average body weights are unchanged, which shows that there is no significant toxicity of MSN systems to the mice (Figure 2.14). The tumors in the control group (Group 1) and unloaded NV-MSN group (Group 3) kept growing, showing that the MSNs themselves did not affect the tumor growth in mice (Figure 2.13 C). Tumor growth inhibition was significant with the administration of free Dox (Group 2). The mice treated with Dox-loaded NV-MSNs (Group 4) and Dox-loaded Tf-NV-MSNs delivered to the mice in Group 5 also showed significant tumor suppression, demonstrating the effective autonomous delivery of Dox inside the tumor. Targeting effects are negligible, as the average tumor volume is within the statistical error of the untargeted MSNs.

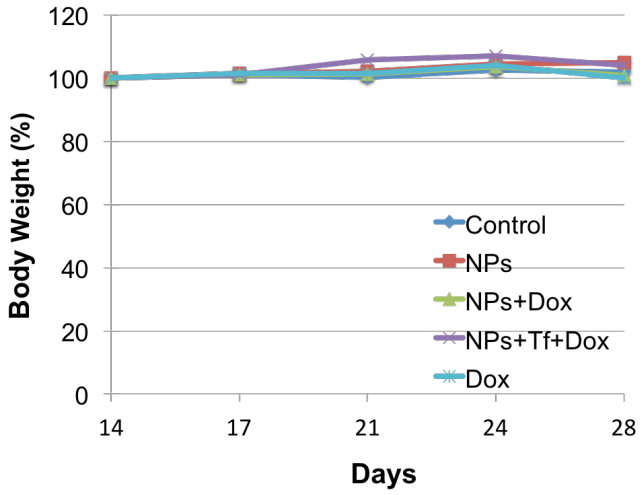

Figure 2.14. Average body weight changes in all groups. Consistent weight shows there is no significant toxicity of the MSN-based systems to the SCID mice.

The results of the hematology and serology examinations are summarized in Table 2.1. The blood test from the mice of Group 2 and 4 showed mild bone marrow suppression without significant alteration of liver function or renal functions, which indicates the safety of the whole experiment. These in vivo experiments demonstrate that the nanovalve-modified MSNs are adept at trapping and autonomously releasing cargo in xenograft tumors. The similarity between the therapeutic efficacies of the targeted and untargeted nanoparticles suggests complex in vivo effects. Possibilities include a simple screening effect in which local proteins block the transferrin protein from being sensed by the Tf receptors of cancer cells, or complex interactions with blood cells, such as erythrocytes and macrophages, that can prevent the Tf-NV-MSNs from reaching the tumor site and passing through intraepithelial gap of capillaries in the tumors.[40] Another possible explanation is that two competing effects are at play: the active targeting of the protein and the delayed release of cargo (Figure 2.4 B). As previously discussed, it is probable that the targeting is active, but the impeded release greatly reduces the delivery of cargo and its efficacy. Further in vivo studies are necessary to evaluate the exact nature of this phenomenon in order to optimize the effect of

transferrin targeting to enhance tumor shrinkage. This study demonstrates that both types of pH-sensitive MSNs are more effective for in vivo delivery of doxorubicin than the free drug counterpart.

Table 2.1. Hematology and serology examination summary of SCID mice.

列1	ALB	ALT	AST	BUN	CA	CHOL	CK	CO2	CREAT	DBILI	GGT	GLU	LDH	PHOS	TBILI	TP	WBC	NE
	g/dL	U/L	U/L	mg/dL	mg/dL	mg/dL	U/L	mEq/L	mg/dL	mg/dL	U/L	mg/dL	U/L	mg/dL	mg/dL	g/dL	K/uL	K/uL
control1		28	65														95.66	73.83
control2	2.4	30	126	23	0.5	17		2.7	0.06	0.8		96		0.2	0.7	1.7	33	18.14
control3	0.1	30	97	21		6			0.23	0.5	4		897		0.5	5.7	31.28	23
NPs1		21	91	17						0.3					0.6	0.9	16.9	8.05
NPS2		49	184	20											0.4		16.9	8.05
NP+Dox1	3.3	32	139	19	10.1	56	497	15.7	0.12	0.7	2	25		16.3	0.6	5.1	7.6	3.72
NP+Dox2		26	105	18	0.5	70	368	17.9		0.4	3		950	10.2	0.5	5.5	20.34	15.54
NP+Tf+Dox1		20	209							0.3							87.48	61.44
NP+Tf+Dox2		23	116							0.8	4		1263		0.6	5.5	183.86	116.6
NP+Tf+Dox3		25	135	20						0.4					0.5		89.35	61.67
Dox1		19	182	25						1					0.9		2.88	1.17
DOx2		30	150	17						0.5	0		903		0.4	5.4	26.82	20.16

2.5 Conclusion

We have designed and optimized a multifunctional MSN system that has demonstrated the operation of a pH-sensitive nanovalve in conjunction with transferrin as a targeting agent. Abiotic studies of the MSN system show efficient loading and pH-activated release of doxorubicin in the presence of the large Tf protein, and the release profiles demonstrate that the release kinetics are slower than that of MSNs without the protein. Cellular studies prove that the delivery of cargo is due to the pH activation of the nanovalves in the acidic lysosomes. Fluorescence microscopy images show that membrane permeable cargo can stain the nuclei, while cargo that is membrane impermeable remains in the endosome. The activation of the nanovalve is due to the acidic nature of the endosome: treatment of Baf to prevent the acidification of the lysosomal also prevents valve opening and cargo release.

The cell cytotoxicity assays show the MSN delivery of Dox is more effective than free drug, and targeting by Tf increases its efficacy, especially at low concentrations. In vivo studies were carried out to demonstrate the effective pH-responsive MSNs in SCID mice. The effect of targeting was negligible, which can be attributed to the phenomena of delayed delivery of local proteins

shielding the effect of transferrin in the body. To our knowledge, this is the first operation of a pH-sensitive nanovalve-MSN system in vivo.[41] This study demonstrates that autonomously operating nanovalves functioned as designed in the presence of a bulky protein-targeting agent in not only solution, but also in vitro and in vivo models.

2.6 References

(1) Argyo, C.; Weiss, V.; Bräuchle, C.; Bein, T. *Chem. Mater.* **2013**.

(2) Ambrogio, M. W.; Thomas, C. R.; Zhao, Y.-L.; Zink, J. I.; Stoddart, J. F. *Acc. Chem. Res.* **2011**, *44*, 903–913.

(3) Angelos, S.; Liong, M.; Choi, E.; Zink, J. I. *Chem. Eng. J.* **2008**, *137*, 4–13.

(4) Li, Z.; Barnes, J. C.; Bosoy, A.; Stoddart, J. F.; Zink, J. I. *Chem. Soc. Rev.* **2012**, *41*, 2590–2605.

(5) Tarn, D.; Ashley, C. E.; Xue, M.; Carnes, E. C.; Zink, J. I.; Brinker, C. J. *Acc. Chem. Res.* **2013**, *46*, 792–801.

(6) Trewyn, B. G.; Slowing, I. I.; Giri, S.; Chen, H.-T.; Lin, V. S.-Y. *Acc. Chem. Res.* **2007**, *40*, 846–853.

(7) Wu, S.-H.; Hung, Y.; Mou, C.-Y. *Chem. Commun. (Camb).* **2011**, *47*, 9972–9985.

(8) Xia, T.; Kovochich, M.; Liong, M.; Meng, H.; Kabehie, S.; George, S.; Zink, J. I.; Nel, A. E. *ACS Nano* **2009**, *3*, 3273–3286.

(9) Lu, J.; Liong, M.; Li, Z.; Zink, J. I.; Tamanoi, F. *Small* **2010**, *6*, 1794–1805.

(10) He, Q.; Shi, J. *Adv. Mater.* **2013**, 1–21.

(11) Lu, J.; Choi, E.; Tamanoi, F.; Zink, J. I. *Small* **2008**, *4*, 421–426.

(12) Thomas, C. R.; Ferris, D. P.; Lee, J.-H.; Choi, E.; Cho, M. H.; Kim, E. S.; Stoddart, J. F.; Shin, J.-S.; Cheon, J.; Zink, J. I. *J. Am. Chem. Soc.* **2010**, *132*, 10623–10625.

(13) Meng, H.; Xue, M.; Xia, T.; Ji, Z.; Tarn, D. Y.; Zink, J. I.; Nel, A. E. *ACS Nano* **2011**, *5*, 4131–4144.

(14) Zheng, Q.; Lin, T.; Wu, H.; Guo, L.; Ye, P.; Hao, Y.; Guo, Q.; Jiang, J.; Fu, F.; Chen, G. *Int. J. Pharm.* **2014**, *463*, 22–26.

(15) Chen, X.; Cheng, X.; Soeriyadi, A. H.; Sagnella, S. M.; Lu, X.; Scott, J. A.; Lowe, S. B.; Kavallaris, M.; Gooding, J. J. *Biomater. Sci.* **2014**, *2*, 121.

(16) Cui, Y.; Xu, Q.; Chow, P. K.-H.; Wang, D.; Wang, C.-H. *Biomaterials* **2013**, *34*, 8511–8520.

(17) Li, C.; Yang, D.; Ma, P.; Chen, Y.; Wu, Y.; Hou, Z.; Dai, Y.; Zhao, J.; Sui, C.; Lin, J. *Small* **2013**, *9*, 4150–4159.

(18) Luo, Z.; Cai, K.; Hu, Y.; Zhang, B.; Xu, D. *Adv. Healthc. Mater.* **2012**, *1*, 321–325.

(19) Popat, A.; Liu, J.; Lu, G. Q. (Max); Qiao, S. Z. *J. Mater. Chem.* **2012**, *22*, 11173.

(20) Zhang, Q.; Wang, X.; Li, P.-Z.; Nguyen, K. T.; Wang, X.-J.; Luo, Z.; Zhang, H.; Tan, N. S.; Zhao, Y. *Adv. Funct. Mater.* **2013**.

(21) Zhao, Z.; Meng, H.; Wang, N.; Donovan, M. J.; Fu, T.; You, M.; Chen, Z.; Zhang, X.; Tan, W. *Angew. Chem. Int. Ed. Engl.* **2013**, *52*, 7487–7491.

(22) Lu, J.; Li, Z.; Zink, J. I.; Tamanoi, F. *Nanomedicine* **2011**, *8*, 212–220.

(23) Yanes, R. E.; Tarn, D.; Hwang, A. A; Ferris, D. P.; Sherman, S. P.; Thomas, C. R.; Lu, J.; Pyle, A. D.; Zink, J. I.; Tamanoi, F. *Small* **2013**, *9*, 697–704.

(24) Gao, F.; Li, L.; Liu, T.; Hao, N.; Liu, H.; Tan, L.; Li, H.; Huang, X.; Peng, B.; Yan, C.; Yang, L.; Wu, X.; Chen, D.; Tang, F. *Nanoscale* **2012**, *4*, 3365–3372.

(25) Mackowiak, S. A; Schmidt, A.; Weiss, V.; Argyo, C.; von Schirnding, C.; Bein, T.; Bräuchle, C. *Nano Lett.* **2013**.

(26) Inoue, T.; Cavanaugh, P. G.; Steck, P. A; Brünner, N.; Nicolson, G. L. *J. Cell. Physiol.* **1993**, *156*, 212–217.

(27) Ryschich, E.; Huszty, G.; Knaebel, H. P.; Hartel, M.; Büchler, M. W.; Schmidt, J. *Eur. J. Cancer* **2004**, *40*, 1418–1422.

(28) Ferris, D. P.; Lu, J.; Gothard, C.; Yanes, R.; Thomas, C. R.; Olsen, J.-C.; Stoddart, J. F.; Tamanoi, F.; Zink, J. I. *Small* **2011**, *7*, 1816–1826.

(29) Fang, W.; Wang, Z.; Zong, S.; Chen, H.; Zhu, D.; Zhong, Y.; Cui, Y. *Biosens. Bioelectron.* **2014**, *57C*, 10–15.

(30) Gao, Q.; Xu, Y.; Wu, D.; Sun, Y.; Li, X. *J. Phys. Chem. C* **2009**, *113*, 12753–12758.

(31) Yhee, J. Y.; Lee, S. J.; Lee, S.; Song, S.; Min, H. S.; Kang, S.-W.; Son, S.; Jeong, S. Y.; Kwon, I. C.; Kim, S. H.; Kim, K. *Bioconjug. Chem.* **2013**, *24*, 1850–1860.

(32) Liu, H.; Liu, T.; Wu, X.; Li, L.; Tan, L.; Chen, D.; Tang, F. *Adv. Mater.* **2012**, *24*, 755–761.

(33) Liu, G.; Mao, J.; Jiang, Z.; Sun, T.; Hu, Y.; Jiang, Z.; Zhang, C.; Dong, J.; Huang, Q.; Lan, Q. *Cancer Biother. Radiopharm.* **2013**, *28*, 691–696.

(34) Shah, N.; Chaudhari, K.; Dantuluri, P.; Murthy, R. S. R.; Das, S. *J. Drug Target.* **2009**, *17*, 533–542.

(35) Du, L.; Liao, S.; Khatib, H. A; Stoddart, J. F.; Zink, J. I. *J. Am. Chem. Soc.* **2009**, *131*, 15136–15142.

(36) Mross, K.; Niemann, B.; Massing, U.; Drevs, J.; Unger, C.; Bhamra, R.; Swenson, C. E. *Cancer Chemother. Pharmacol.* **2004**, *54*, 514–524.

(37) Gabizon, A. A. *Cancer Invest.* **2001**, *19*, 424–436.

(38) Fava, A.; Iliceto, A.; Camera, E. *J. Am. Chem. Soc.* **1957**, *79*, 833–838.

(39) Dong, J.; Xue, M.; Zink, J. J. I. *Nanoscale* **2013**, *5*, 10300–10306.

(40) Salvati, A.; Pitek, A. S.; Monopoli, M. P.; Prapainop, K.; Bombelli, F. B.; Hristov, D. R.; Kelly, P. M.; Åberg, C.; Mahon, E.; Dawson, K. A. *Nat. Nanotechnol.* **2013**, *8*, 137–143.

(41) Chen, Y.; Chen, H.; Shi, J. *Adv. Mater.* **2013**, *25*, 3144–3176.

CHAPTER 3

Delivery of Cargo Using

Large Pore Nanoparticles

3.1 Abstract

The delivery of small molecules and therapeutics has been well established by mesoporous silica nanoparticles, however the delivery of large biomolecules (DNA, siRNA, mRNA, proteins, etc.) has not. The primary mode of delivery is adsorption on the surface of nanoparticles, instead of being contained and protected inside a nanoparticle structure. Large pore nanoparticles (LPNPs) are synthesized and their biological compatibility is tested in order to design large cargo delivery system. Chitosan, an abundant and economic biopolymer, is attempted to be used as a capping system for the LPNPs. Three different synthetic approaches are used to covalently attach the polymer to the surface. The method of using amine-functionalized LPNPs with NHS/EDC coupling with chitosan is the most successful. The chitosan-LPNP system is tested for loading, however incompatibility with loading cargo and opening the polymer are in conflict and the design is compromised. Although promising, further redesign and testing are needed to optimize the system for delivery.

3.2 Introduction

Mesoporous silicate nanomaterials are an attractive delivery system for small molecules, as they are synthesized at a low cost, biocompatible, and easily functionalized. They are fabricated via a colloidal, sol-gel synthesis, in which amorphous silica is formed in the presence of an alkaline aqueous solution. The nanoparticles' ordered structure is variable, dictated by the concentrations of silica precursor, base, and water, with the addition of templating agents.[1,2] The diversity in surfactants used in the sol-gel fabrication process enables a wide range of nanoparticle morphologies, which in a broader sense, templating agents can range from surfactants, co-surfactants, vesicles, polymer, to inorganic cores, which provide a multitude of choices when choosing the appropriate delivery system for application.[2–9] Most prolific is the MCM-41-type of mesoporous silica nanoparticle (MSN), which has been used by many for drug delivery systems.[10–16] MCM-41 nanoparticles are templated by a binary surfactant system, using cetyltrimethylammonium bromide (CTAB), to form 2-dimensional hexagonal wormlike structure in the silica.[17,18] They have proven to show great success in the delivery of small molecule therapeutics and delivery of large biomolecules on the surface, however their dimensions (~2 nm diameter pores) make it difficult or nearly impossible to protect and deliver large cargo or proteins (> 3 nm).

Alternative MSNs with diverse structures have been synthesized and studied, however most are not suitable for drug delivery because of large and/or irregular particle sizes. Swelling agents have been implemented into the CTAB micellular structure to increase the pore sizes, but have significant drawbacks. MCM-41 nanoparticles can be expanded up to 10 nm pore diameters, however the ordered structure is lost and thereby is difficult to control for delivery.[19,20] SBA-15, synthesized in acidic conditions, utilizes Pluronic 123 as a templating agent to produce a hexagonal array of ~ 6-30 nm tunable pore diameters.[19–21] Although the SBA-15 pore size is appropriate for

larger cargos, the particle size is on the order of microns, which is unsuitable for *in vitro* drug delivery.

Fluorocarbon surfactants are typically used for high-temperature synthesis, due to their stability at high temperatures (> 200 °C). They are difficult to use for MSN synthesis because the fluorocarbons are rigid and primarily hydrophobic, which make the ordered micellular structure form very slowly.[22] However, when used in conjunction with nonionic triblock copolymers, can produce highly ordered, porous, and stable silica structures.[23–25] These materials can form large pore nanoparticles (LPNPs) at precise conditions, which can be used as a platform for larger cargo delivery systems.

Due to the large pore size of these nanoparticles, our typical supramolecular machines would be incompatible in size. In this work, we attempted two different methods to control the pores of LPNPs by a pH-sensitive mechanism, to deliver a rifampicin, a bactericidal antibiotic. Rifampicin (RIF) is largely used as an antibiotic for treating tuberculosis, however has been difficult to effectively trap and release as cargo. We have utilized electrostatic attraction as a method of adsorbing the negatively charged RIF onto the surface of positively charged PEI-coated MSNs to deliver an effective quantity in vitro.[26] However in vivo delivery has proven difficult, due to the low loading, slow leakage, and poor dispersability in saline solutions. Our initial endeavor utilized an alternative pH-sensitive biopolymer— chitosan, derived from the chitin that can be found in most shrimp and crustaceans, to block the pore.[27] Chitosan was chosen for its beneficial properties; the biopolymer is very abundant and can be made using green chemistry techniques. Furthermore, chitosan has antibacterial properties and is sensitive to pH.[27] Its sensitivity is derived from the amine groups on the glucosamine polymers—as the amines are protonated in acidic solution (pKa ~ 6.3), the chitosan becomes more soluble in aqueous solutions.[28] Many synthetic iterations were tested, however none of the materials functioned as a gatekeeper.

We also attempted a larger molecular machine, a megagate, designed by Min Xue that could be used to block the pores of SBA-15 and protect the porcine liver esterase (PLE) stored inside the particle.[29] However the RIF cargo and the megagate cap were incompatible in solution, and almost impossible to load. Herein, we describe several synthetic potential approaches for capping the LPNPs with chitosan for biological study. We show the nanoparticles can be functionalized with alkoxysilanes and even chitosan, however the loading is very poor. Preliminary biological studies show that the LPNPs can be labeled and cause very little cytotoxicity, which demonstrate their potential as a large cargo carrier.

3.3 Materials and Methods

Materials

All reagents were used as received without further purification. 3-Aminopropyltriethoxysilane (APTES, 99%), cetyltrimethylammonium bromide (CTAB, 90%), fluorescein isothiocyanate (FITC, 90%), 4-(2-hydroxyethyl)-1-piperazineethanesulfonic acid (HEPES buffer, 0.05 M), and 3-(trihydroxysilyl)propyl methylphosphonate monosodium aqueous solution (HTMP, 42%), mesitylene, and chitosan (low molecular weight), and mesitylene were purchased from Sigma. 3-(trimethoxysilyl)butyl aldehyde (TMSBA, 90%), (3-glycidoxypropyl)trimethoxysilane (GPTMS) and 3-aminopropyltrimethoxysilane (APTES, 90%), tetraethyl orthosilicate (TEOS, 90%) were obtained from Gelest. Fluorocarbon surfactant (FC-4) was received from Yick-Vick. Pluronic P65 was generously donated from BASF Chemicals.

General Methods

Transmission electron microscopy (TEM) images were obtained using a JEM1200-EX (JEOL) instrument. UV-vis spectra were collected by a Cary 500 UV-vis-NIR spectrophotometer. N_2 adsorption/desorption isotherms were obtained at 77 K on a Quandrchrome Surface Area and Pore Size Analyzer. Thermogravimetric analysis (TGA) was performed by a Pyris Diamond

TG/DTA (Perkin-Elmer Instruments). DLS and zeta potentials were measured by ZetaSizer Nano (Malvern Instruments Ltd., Worcestershire, U.K.).

Synthesis of LPNPs

Two surfactants, Pluronic P65 (0.25 g) and FC-4 (0.7 g), were dissolved in a dilute, aqueous HCl solution (35 mL, 0.02 M) overnight. To increase the pore diameter, mesitylene (870 μL) was added to the solution and vigorously stirred for at least 4 hours at room temperature. The silica precursor, TEOS (2 mL) was slowly added drop-wise, and left to react overnight at room temperature. The as-synthesized solution was transferred to an autoclave and heated to 100 °C for 24 hours. Particles were collected by centrifugation and the surfactant was removed by calcination (550 °C) or Soxhlet extraction for 3 days.

Chitosan attachment via epoxide-terminated LPNPs

Using a modified procedure, the LPNPs (100 mg) were first functionalized with the epoxide-terminated silane, GPTMS (50 μL) by refluxing in dry toluene overnight.[30] Subsequently, chitosan (100 mg, low molecular wt) was dissolved in 10 mL of aqueous 3% v/v acetic acid (HAc) solution. The epoxide-terminated LPNPs were suspended in dry ethanol and the chitosan solution was slowly added drop-wise. The solution was allowed to sit in a sealed vial at room temperature for at least 24 h while mixing. The nanoparticles were collected by centrifugation and washed with ethanol.

Chitosan attachment via aldehyde-terminated LPNPs

As synthesized LPNPs (100 mg) were suspended in 10 mL toluene and 150 μL of 3-(trimethoxysilyl)butyl aldehyde was added, and reacted overnight under nitrogen. The aldehyde-modified LPNPs (CHO-LPNPs) were washed with methanol several times and resuspended in PBS buffer (pH 5). The suspension of CHO-LPNP was slowly added into chitosan solution (2% wt/wt, acetic acid, pH 5) and stirred for 4 hours. $NaBH_3CN$ (60 mg) was added and left to stir overnight.

The LPNPs were washed with pH 5 PBS buffer twice to remove the excess polymer and resuspended in the desired solution.

Chitosan attachment via carboxcylic-terminated LPNPs

LPNPs (100 mg) were first derivitized with 3-aminopropyltrimethoxysilane (50 μL, APTES) in anhydrous toluene (10 mL). The solution was left to react overnight at reflux and under nitrogen. The solution was cooled and washed with toluene and methanol. The NH_2-terminated LPNPs were converted to carboxcylic acids by treatment with maleic anhydride. The COOH-terminated LPNPs were suspended in a PBS buffer and an EDC/NHS mixture (EDC = 0.2 M, NHS = 0.2 M) in 25 mL of PBS (pH 5) was put in to activate the carboxylic group of silica nanoparticles. The mixture was allowed to settle for 2 h to attain stable suspension at ambient temperature, and chitosan solution (low molecular weight, 2% wt) in an acetic acid solution (2%) was added drop-wise. The mixture was stirred for another 12 hours at room temperature and washed with PBS buffer (pH 5). The resulting LPNPs were washed with water and methanol.

Loading and Capping

Particles were loaded with RIF by suspending chit-LPNPs in a slightly acidic water solution (pH 4, 10 mg/mL) solution for 2 days. Once loaded, particles were capped by adjusting the pH to 7.4. Particles were washed in PBS buffer.

PEG Coating

To improve dispersion, the loaded chitosan-coated LPNPs (25 mg) were suspended in water (3 mL), and activated PEG was added (25 mg). The solution was stirred overnight at room temperature, washed with water several times.

Fluorescent Labeling

Amine-functionalized nanoparticles were labeled with fluorescein for imaging purposes. Fluorescein isothiocyanate (FITC, 2 mg) was dissolved in dry ethanol (1.5 mL) and the amine-

functionalized LPNPs were added. The mixture was left to react under nitrogen overnight and washed with ethanol.

3.4. Results & Discussion

In this study, LPNPs were synthesized in a modified procedure to produce nanoparticles with sizable pores to hold and protect large biological molecules.[24] Although there have been many instances of biological molecule delivery via nanoparticles, the biomolecule has primarily resided on the outside of the nanoparticle. Our aim is to be able to synthesize nanoparticles that have pores large enough to hold biomolecules, and design a system to release the biomolecule on demand. In particular, we focused on rifampicin (RIF), a first-line antibiotic used in the treatment of tuberculosis (Figure 3.1 A). In our approaches, we used the positively charged poly(ethylene imine) (PEI) polymer to electrostatically adsorb the negatively charged RIF to the surface of MSNs. Results have shown that although the RIF is able to delivered in vitro, the loading capacity is low and can incur some toxicity when used in high doses.

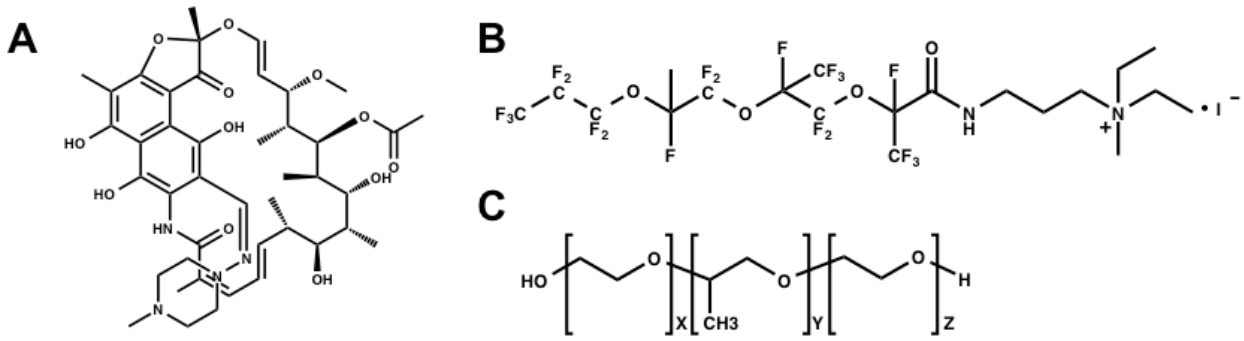

Figure 3.1. The structures of A) rifampicin (RIF), model cargo used for delivery; B) fluorocarbon (FC-4) and C) general structure of Pluronic (F127) surfactants used in LPNP synthesis.

In order to synthesize the LPNPs, two cosurfactants (FC-4 and Pluronic P65) were dissolved in a slightly acidic solution overnight (Figure 3.1 B&C). The swelling agent, mesitylene, was added and left to stir for at least 4 hours at room temperature, and finally TEOS was added and the

solution was left to react overnight. Subsequently the solution was autoclaved at 100 °C to age the silica structure. In order to remove the templating surfactants, the nanoparticles were subjected to calcination or Soxhlet extraction to produce large pored nanoparticles. Analysis by TEM showed the nanoparticles were ranging from 80 – 130 nm in diameter by TEM (Figure 3.2 A&B).

The surfactant was removed from LPNPs by the two extraction methods, calcination and Soxhlet extraction, which were tested by FT-IR (Figure 3.2 C&D). As seen in the FT-IR spectra, characteristic peaks from the surfactant molecules are no longer present in the spectrum of the calcined LPNPs, however some residual peaks are still seen in the Soxhlet extraction. More specifically, peaks are seen at ~2900 and 3500 cm^{-1}, due to the –CH bonds and –OH respectively of the Pluronic 65, which is made up of poly(propylene oxide) and poly(ethylene oxide) chains. The C-F bond stretches in the fluorocarbon polymer are seen at 1200 cm^{-1}, but disappear after surfactant extraction. Although Soxhlet extraction was the preferred method to prevent the formation of toxic siloxane bonds, the removal of the surfactant seems to be more efficient and effective with calcination.[31]

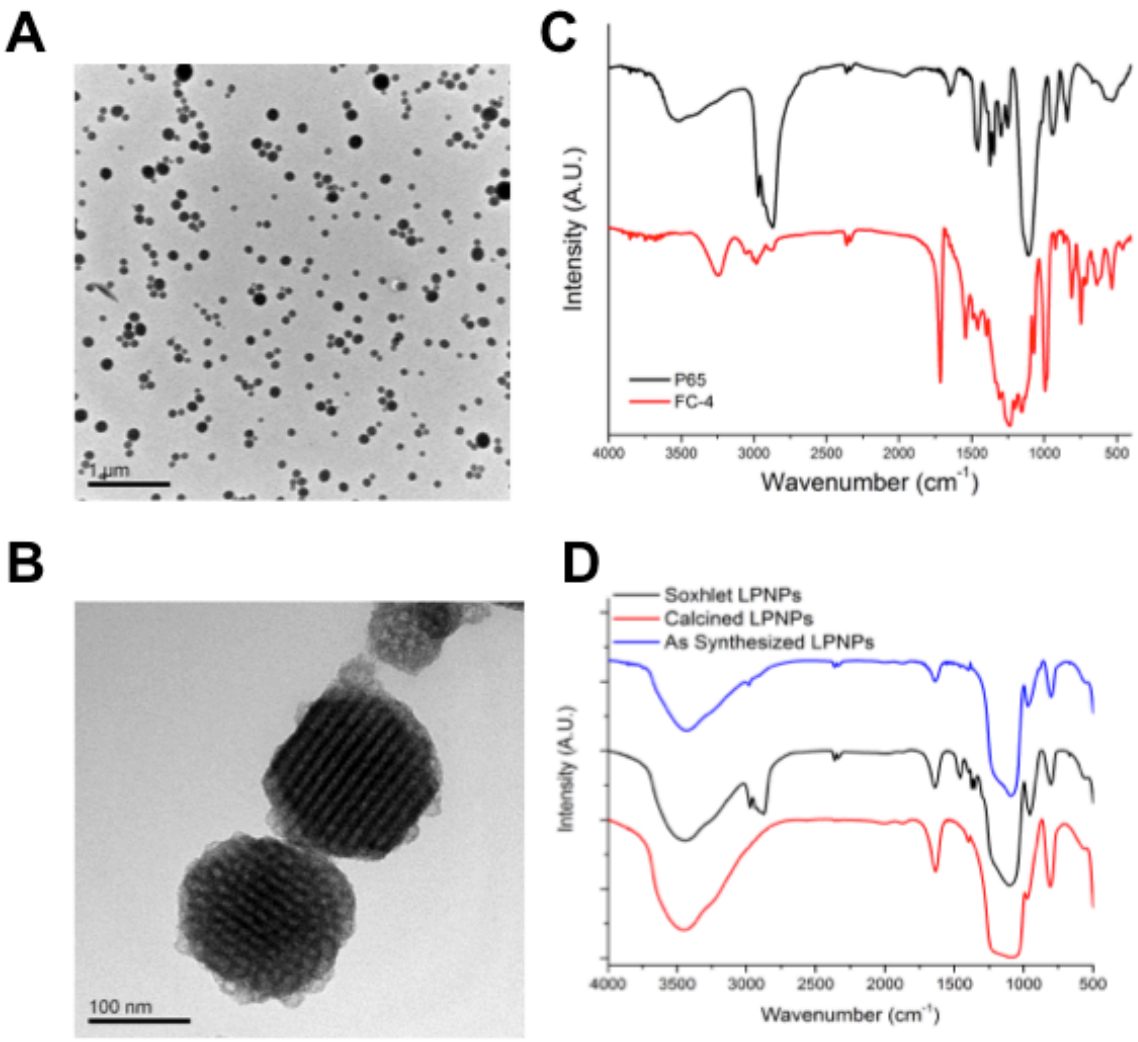

Figure 3.2. A) and B) are transmission electron microscope (TEM) images of LPNPs; C) FT-IR spectra of the two surfactants used, FC-4 and Pluronic P65; D) KBr pellet of as synthesized nanoparticles (blue trace), Soxhlet extracted (black trace), and calcined LPNPs (red trace), with the surfactants (red trace).

Further characterizations were carried out to determine the properties of the LPNPs. TGA analysis was used to further test the extraction methods. The Soxhlet extracted LPNPs had a weight loss to that of unextracted LPNPs, giving further evidence that calcination is a more effective removal of surfactants (Figure 3.3 A). Measurement by DLS showed the hydrodynamic radius was approximately 200 nm, which is suitable for biological studies. Nitrogen adsorption/desorption studies of the samples before and after showed the nanoparticles had a very porous structure, with

surface area of approximately 700 m^2/g after extraction (Figure 3.3 C). The BHJ calculations found that the primary pore size was approximately 10 nm, compatible with the biological molecules we aim to deliver (Figure 3.3 D).

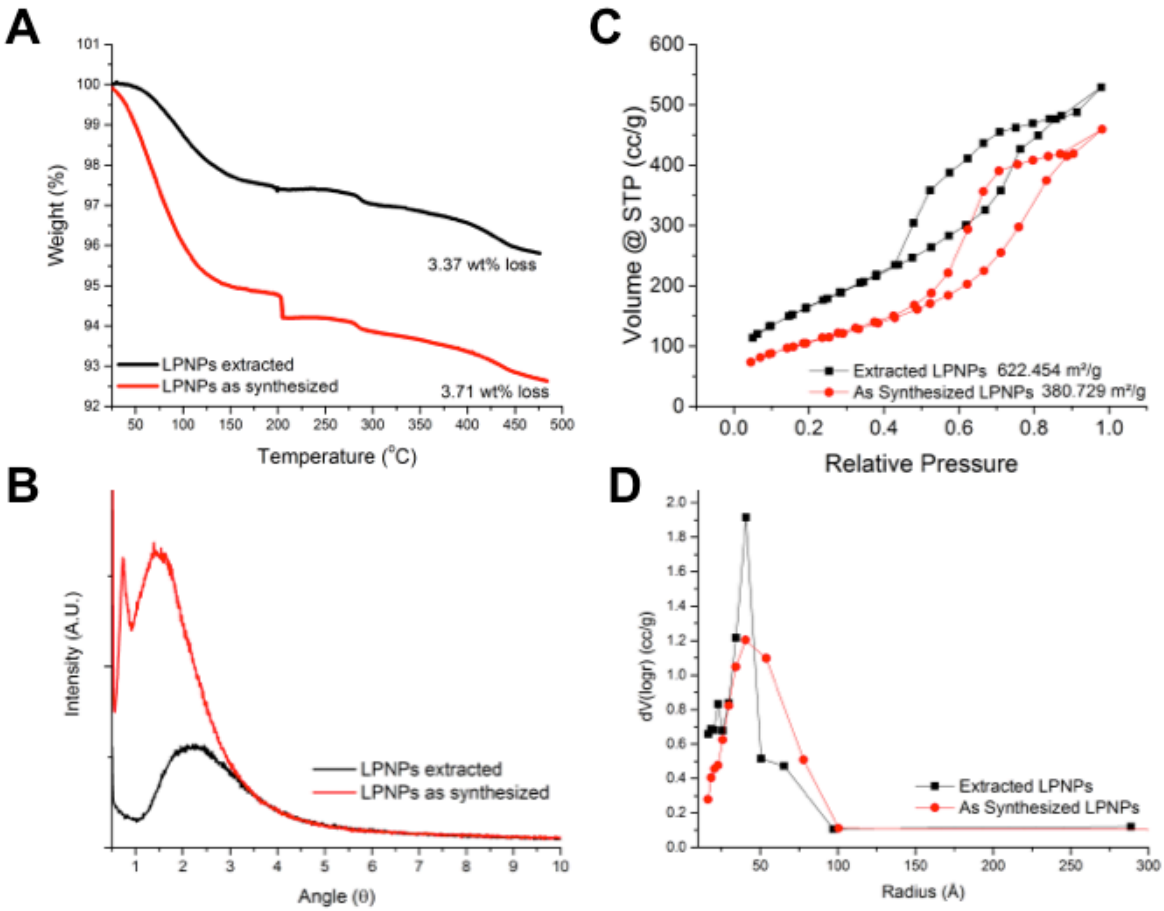

Figure 3.3. A) TGA B) XRD, C) Nitrogen adsorption/desorption curves of extracted (black trace) and as synthesized (red trace) LPNP samples. Surface area of extracted LPNPs is 622.4 m^2/g while as synthesized materials have 380.7 m^2/g, demonstrating the effects of the surfactant inside the pore on measurements. D) graphs shows the primary pore diameter of the LPNPs are ~10 nm, which sharply increase after extraction.

As these LPNPs were to be used in biological systems, the nanoparticles were labeled with fluorescein and tested in various cell lines for cell toxicity. Initial studies in MiaPaCa-2 cells showed that the nanoparticles were nontoxic and were endocytosed as evidenced by fluorescence imaging. The fluorescein-labeled LPNPs (green) are seen to co-localize with the cell nucleus (blue) and within

the cell membrane (red) (Figure 3.5 A). As these nanoparticles were about twice as large as the typical MCM-41-type of nanoparticle used, we wanted to test stability in biological solutions. The LPNPs were functionalized with typical MSN surface modifications, negatively charged phosphonate or a positively charged poly(ethylene imine) coating, which are typically used to help dispersability in biological media. The cells had a very high tolerance of phosphonated LPNPs in toxicity studies, however that could also be attributed to little to no endocytosis of the LPNPs as a false positive (Figure 3.5 B). The material was also tested in macrophages (THP-1) as the cargo to be delivered was aimed to treat *M. tuberculosis* bacteria that reside inside the macrophage. Fluorescence imaging showed the labeled nanoparticles (green) were easily taken up by the cells, shown by the co-localization of the cell nucleus (blue) and the cell (red) (Figure 3.6). The bare FITC-labeled LPNPs were taken up well by THP-1 cells, however PEI-MSN are taken up better than the uncoated or phosphonate coated particles (Figure 3.7). Greater uptake of positively charged particles than uncoated or negatively coated particles is consistent with ionic interaction of our typical MSNs coated in a positive charge with negatively charged cell surface. There is some cytotoxicity from the 100 mg/mL dose of PEI-LPNPs that was not apparent with the uncoated or phosphonate coated MSN or lower concentrations of PEI-LPNPs.

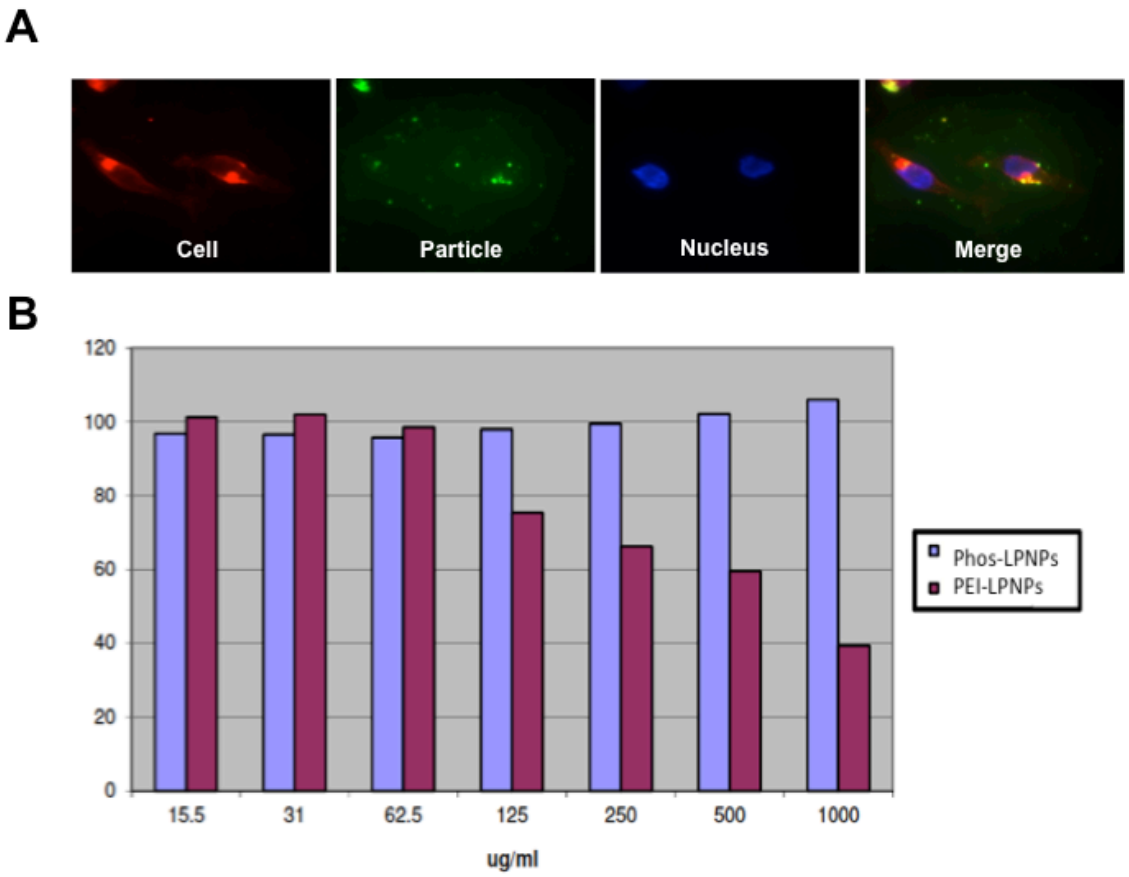

Figure 3.5. A) MiaPaCa-2 cells incubated with fluorescein-labeled Phos-LPNP (green), nucleus is stained with DAPI (blue), cell membrane is stained with Lysotracker Red (red); B) Cell toxicity study of LPNPs functionalized with phosphonate and PEI that show cells can tolerate a large quantity of Phos-LPNPs.

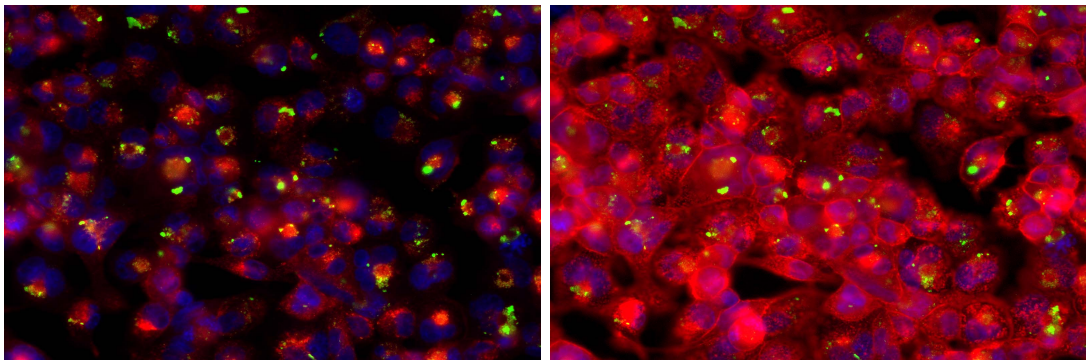

Figure 3.6. THP-1 cells incubated with 12.5 μg/ml PEI-LPNP-FITC (green). Blue = DAPI. On the left, red = LAMP-1 (lysosomes); on the right, red = WGA-647 (plasma membranes).

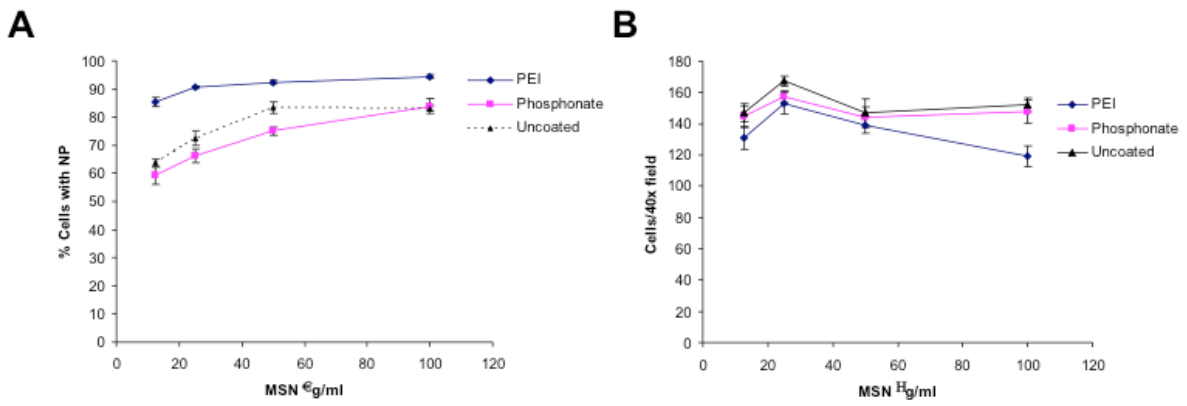

Figure 3.7 A) Percentage of cells with one or more green fluorescent dots, PEI-coated LPNPs are taken up by a higher % of THP-1 cells than are the uncoated or phosphonate coated MSN. B) THP-1 cells per 40x microscope field, appears to be some toxicity from the 100 mg/mL dose of PEI-LPNP, reflected in fewer cells per field. This toxicity is not seen at the lower doses.

Although many nanomachines have been studied to show an improved stimuli-responsive delivery system, the LPNPs are not ideal as a platform for these nano gatekeepers. The nanoparticle pores are too large for the typical supramolecular chemistries being used. Instead, we had several attempts at using chitosan as a pH-sensitive polymer cap. Chitosan is insoluble at pHs greater than 6, which has been used to make stable chitosan nanoparticles.[32,33] However at pH under 5, the chitosan is easily soluble, due to the protonated amine groups. The polymer expands in solution that can enable cargo to diffuse out. However, the chitosan proved to be difficult to covalently attach to the surface. We will discuss three different approaches used to covalently attach chitosan onto the surface of the LPNPs.

Initially, the LPNPs were functionalized with an aldehyde-terminated silane, to utilize the amine-aldehyde reaction to form an imine bond. In order promote the forming of the imine bond, the reaction was left to stir for at least 24 hours or longer. Once the imine bond formed, the bond was reduced to form a stable tertiary amine bond (Figure 3.6 A).

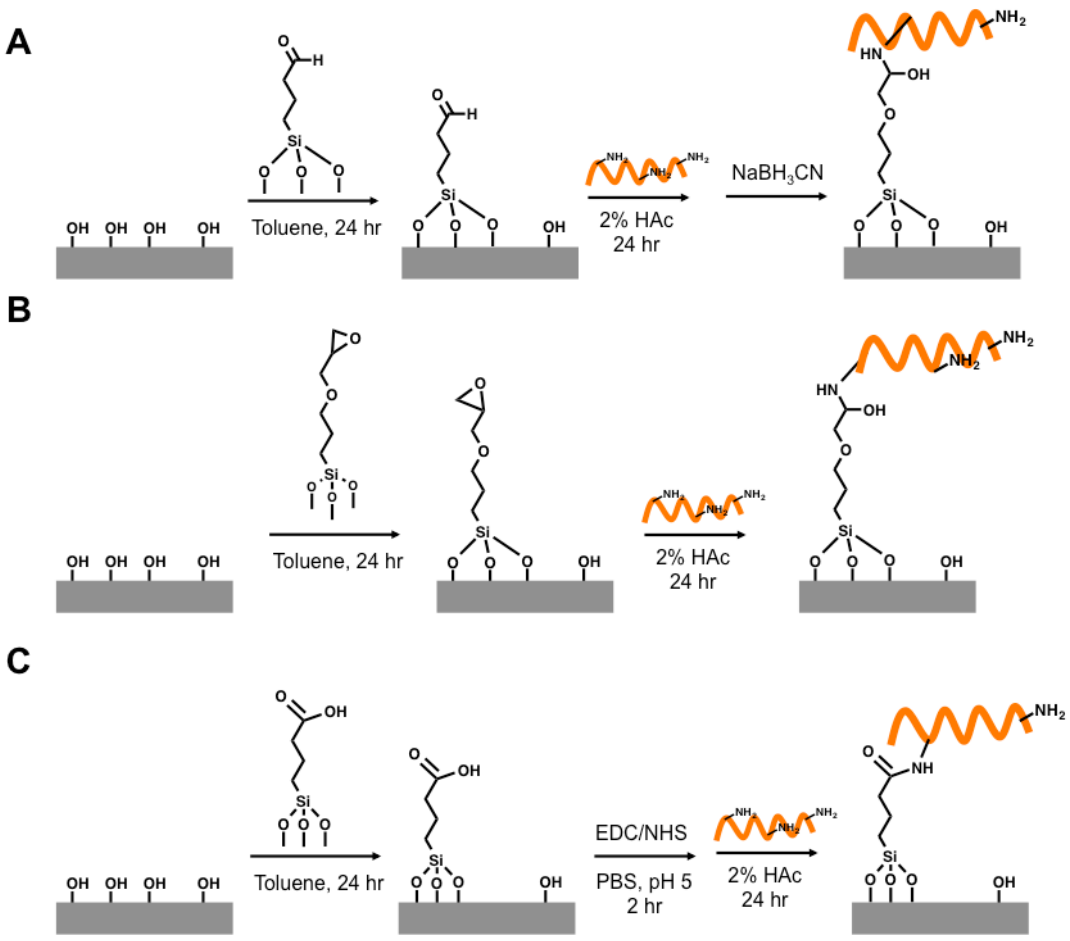

Figure 3.8. The three synthetic approaches for attaching chitosan to the silica surface of LPNPs. A) using aldehydes to react with amines on the chitosan to form an imine bond, that is later reduced by $NaBH_3CN$; B) attaching an epoxide-terminated silane, which will be attached by the amines on the chitosan; C) functionalizing the surface of the nanoparticle with carboxylic acid-terminated silanes to use the well-known EDC/NHS coupling to form a stable amide bond.

Although proven in some literature in forming chitosan nanoparticles with glutaraldehyde, this approach was not successful. Analysis by FT-IR did not show any presence of chitosan. In a second approach, an epoxide-terminated silane was attached to the surface of the LPNPs. The epoxide will be attacked by the amines on the chitosan, and was seen in a previously published literature method for thin films.[30] The epoxide-amine reaction was unsuccessful, most likely due to the low reactivity of epoxides in acid (Figure 3.8 B). Finally, the most successful approach was to first functionalize

the nanoparticles with amines, and subsequently convert the amines into carboxylic acids using maleic acid (Figure 3.8 C). The carboxcylic acid and the amines of the chitosan were then attached using the well-known EDC/NHS coupling to form a stable amide bond.

First, the conversion of amines to carboxcylic acid groups was confirmed by FT-IR. As seen in Figure 3.9 A, the sharp amine stretch is prominent at 2900 cm^{-1} (red trace), and decreases after conversion to carboxcylic acid groups (black trace). Furthermore, the carbonyl stretch at 1700 cm^{-1} (black trace) is more prominent. The attachment of chitosan was monitored by FT-IR, which showed the amine stretches grow in around 2900 cm^{-1} and 1000 – 1500 cm^{-1} (Figure 3.9 B). Further testing via ^{13}C and ^{29}Si solid state NMR is necessary to confirm the attachment of the chitosan onto the surface.

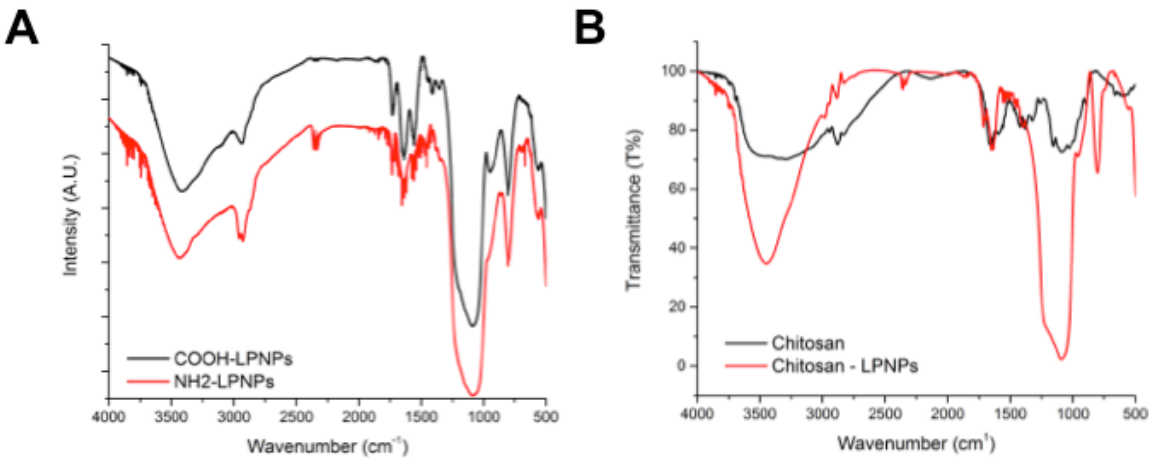

Figure 3.9. FT-IR spectra of A) amine surface functionalizations on LPNPs (red trace) and the conversion of amine groups to carboxcylic acid (black trace) with maleic acid; B) pure chitosan and chitosan-modified LPNPs.

The chitosan-modified LPNPs were then tested with our desired therapeutic, rifampicin (RIF), a first line therapeutic used to treat *M. tuberculosis*. Nanoparticles were loaded with RIF at an acidic solution (pH 4-5), in order to solubilize the chitosan polymer so the pores could be accessible

for the RIF to diffuse into the silica matrix. The LPNPs were loaded for 24 hours and washed with PBS buffer. Unfortunately, the system was highly leaky and a great deal of the RIF was washed away. The RIF that was trapped by the chitosan was very difficult to remove. Analysis by UV-Vis showed the acidic release of the LPNPs had almost to difference from that in the neutral solution.

3.5 Summary

Initial attempts for a large pore nanoparticle system to protect and subsequently deliver large biomolecules are reported. The LPNPs are biologically compatible and can be easily functionalized by typical means, similar to MSNs. However, typical nanomachines as capping agents are not compatible, which made it necessary to move to a different capping mechanism. Chitosan was chosen due to its antibacterial and pH-sensitive properties, as well as its low cost and abundance. The therapeutic of choice to be delivered was difficult to load; however some loading and release were possible. It is probable the quantity of chitosan was not enough to cover the surface of the nanoparticles in its entirety, or the interactions between the silica, chitosan, and rifampicin were not optimal. Although chitosan was not an optimal capping agent, the large pore nanoparticles were able to hold cargo. It is necessary for further redesign of the system to understand the interactions between the materials or test new materials towards a new capping agent, to pursue this viable delivery system.

3.6. References

(1) Brinker, C. J.; Scherer, G. W. *Sol-gel science: the physics and chemistry of sol-gel processing*; Academic Pr, 1990.

(2) Wu, S.-H.; Mou, C.-Y.; Lin, H.-P. *Chem. Soc. Rev.* **2013**, *42*, 3862–3875.

(3) Xing, R.; Lehmler, H.; Knutson, B.; Rankin, S. *Langmuir* **2009**, *25*, 6486–6492.

(4) Areva, S.; Boissière, C.; Grosso, D.; Asakawa, T.; Sanchez, C.; Lindén, M. *Chem. Commun. (Camb).* **2004**, 1630–1631.

(5) Che, S.; Liu, Z.; Ohsuna, T.; Sakamoto, K. *Nature* **2004**, *429*, 281–284.

(6) Lu, A.-H.; Salabas, E. L.; Schüth, F. *Angew. Chem. Int. Ed. Engl.* **2007**, *46*, 1222–1244.

(7) Yang, M.; Wang, G.; Yang, Z. *Mater. Chem. Phys.* **2008**, *111*, 5–8.

(8) Han, L.; Wei, H.; Tu, B.; Zhao, D. *Chem. Commun. (Camb).* **2011**, *47*, 8536–8538.

(9) Liong, M.; Lu, J.; Kovochich, M.; Xia, T.; Ruehm, S. G.; Nel, A. E.; Tamanoi, F.; Zink, J. I. *ACS Nano* **2008**, *2*, 889–896.

(10) Guo, R.; Li, L.-L.; Zhao, W.-H.; Chen, Y.-X.; Wang, X.-Z.; Fang, C.-J.; Feng, W.; Zhang, T.-L.; Ma, X.; Lu, M.; Peng, S.-Q.; Yan, C.-H. *Nanoscale* **2012**, *4*, 3577–3583.

(11) Hom, C.; Lu, J.; Liong, M.; Luo, H.; Li, Z.; Zink, J. I.; Tamanoi, F. *Small* **2010**, *6*, 1185–1190.

(12) Wu, S.-H.; Hung, Y.; Mou, C.-Y. *Chem. Commun. (Camb).* **2011**, *47*, 9972–9985.

(13) Yang, P.; Gai, S.; Lin, J. *Chem. Soc. Rev.* **2012**, *41*, 3679–3698.

(14) Dong, J.; Xue, M.; Zink, J. J. I. *Nanoscale* **2013**, *5*, 10300–10306.

(15) Hwang, A. A.; Lu, J.; Tamanoi, F.; Zink, J. I. *Small* **2014**, 319–328.

(16) Vivero-Escoto, J. L.; Slowing, I. I.; Trewyn, B. G.; Lin, V. S.-Y. *Small* **2010**, *6*, 1952–1967.

(17) Grün, M.; Lauer, I.; Unger, K. K. *Adv. Mater.* **1997**, *9*, 254–257.

(18) Di Renzo, F.; Cambon, H.; Dutartre, R. *Microporous Mater.* **1997**, *10*, 283–286.

(19) Corma, A.; Kan, Q.; Navarro, M. T.; Pérez-Pariente, J.; Rey, F. *Chem. Mater.* **1997**, *9*, 2123–2126.

(20) Sayari, A.; Yang, Y.; Kruk, M.; Jaroniec, M. *J. Phys. Chem. B* **1999**, *103*, 3651–3658.

(21) Sayari, A; Liu, P.; Kruk, M.; Jaroniec, M. *Chem. Mater.* **1997**, *9*, 2499–2506.

(22) Xiao, F. *Curr. Opin. Colloid Interface Sci.* **2005**, *10*, 94–101.

(23) Han, Y.; Li, D.; Zhao, L.; Song, J.; Yang, X.; Li, N.; Di, Y.; Li, C.; Wu, S.; Xu, X.; Meng, X.; Lin, K.; Xiao, F.-S. *Angew. Chem. Int. Ed. Engl.* **2003**, *42*, 3633–3637.

(24) Han, Y.; Ying, J. Y. *Angew. Chem. Int. Ed. Engl.* **2004**, *44*, 288–292.

(25) Wang, C.; Du, Y.; Li, D.; Guan, X.; Li, F.; Xiao, F.-S. *J. Colloid Interface Sci.* **2008**, *319*, 370–373.

(26) Clemens, D. L.; Lee, B.-Y.; Xue, M.; Thomas, C. R.; Meng, H.; Ferris, D.; Nel, A. E.; Zink, J. I.; Horwitz, M. A. *Antimicrob. Agents Chemother.* **2012**, *56*, 2535–2545.

(27) Rinaudo, M. Chitin and chitosan: Properties and applications. *Prog. in Poly. Sci.*, **2006**, *31*, 603–632.

(28) Riva, R.; Ragelle, H.; Des Rieux, A.; Duhem, N.; Jérôme, C.; Préat, V. *Adv. in Poly. Sci.*, **2011**, *244*, 19–44.

(29) Xue, M.; Zink, J. I. *J. Am. Chem. Soc.* **2013**, *135*, 17659–17662.

(30) Wu, J.; Sailor, M. J. *Adv. Funct. Mater.* **2009**, *19*, 733–741.

(31) Tarn, D.; Ashley, C. E.; Xue, M.; Carnes, E. C.; Zink, J. I.; Brinker, C. J. *Acc. Chem. Res.* **2013**, *46*, 792–801.

(32) Rampino, A.; Borgogna, M.; Blasi, P.; Bellich, B.; Cesàro, A. *Int. J. Pharm.* **2013**, *455*, 219–228.

(33) Zhao, L.; Shi, L.; Zhang, Z. *Brazilian J.* … **2011**, *28*, 353–362.

CHAPTER 4

Exocytosis Mechanism of MSNs and the Effects of the Protein Corona

4.1 Overview

Utilizing various surface-modified, magnetic core MSNs (mag@MSNs) and incubating them will various cell lines, we seek to understand their biological fate in a two-part study. First, the exocytosis of phosphonate-modified mag@MSNs is studied for a multitude of cell lines (A549, MDA-MB 231, and MDA-MB 435), presented in Sections 4.2-4.5. The inhibition or acceleration of lysosomal exocytosis can achieve MSN exocytosis regulation, which can enhance the effects of the delivery of camptothecin, an anticancer drug. Lysosomal exocytosis is identified as the mechanism responsible for MSN exocytosis. Second, a proteomic approach is taken to analyze MSNs-bound proteins extracted from cancer cells to develop these nanoparticles as an analytical tool is presented in Sections 4.6-4.9. Mag@MSNs modified with positive or negative charges were endocytosed by various cell lines (A549, HFF, or MCF7), isolated, and analyzed by mass spectrometry. Negatively charged particles possessed a more extensive network of proteins within their protein corona regions when incubated with cancerous cell lines, while the highly positive particles were not shown to have a significant corona in cancerous cell lines. Unique proteins were identified from MSNs incubated with cancer cell lines (A549 and MCF7) in comparison to MSNs incubated with normal cell lines (HFF). Ultimately, these data indicate the promising potential of MSNs as diagnostic tools due to the varying composition of their protein coronas attributed to the different cell lines.

I would like to acknowledge my collaborators, Dr. Jie Lu, Dr. Fuyuhiko Tamanoi, Dr. Carly Ferguson, Dr. Rolando Yanes, and Dr. Joseph Loo for the work presented in this chapter. The first part of this work presented in 4.2-4.5 has been adopted from the previously published article, Yanes, R. E.; Tarn, D.; Hwang, A. A; Ferris, D. P.; Sherman, S. P.; Thomas, C. R.; Lu, J.; Pyle, A. D.; Zink, J. I.; Tamanoi, F. Involvement of Lysosomal Exocytosis in the Excretion of Mesoporous Silica Nanoparticles and Enhancement of the Drug Delivery Effect by Exocytosis Inhibition. *Small* **2013**, *9*, 697–704.

4.2 Effect of Lysosomal Exocytosis on Mesoporous Silica Nanoparticles and Enhancement of the Drug Delivery Effect

Advances in nanotechnology have resulted in the development of new nanoparticles that have the potential to revolutionize medicine. Many nanomaterials have been engineered that promise to enhance drug delivery efficacy to target tissues, reduce side effects, and provide a delivery vehicle for hydrophobic anticancer drugs or imaging agents. Among these materials, mesoporous silica nanoparticles (MSNs) have received much attention because of their large surface area, large internal pore volume, tunable pore size, and stability.[1–4] We as well as others have shown that MSNs can serve as efficient drug delivery and imaging vehicles for theranostic medicine.[1,2,5–13] MSNs are biocompatible and easily taken up by cancer cells via energy-dependent endocytosis, of which the majority co-localize within the endo/lysosome compartments.[14–18] Their biocompatibility, biodistribution and their efficacy to inhibit tumor growth have been demonstrated in animal studies.[19–21]

MSN chemistry has been well developed to allow the customization of external surface and internal packaging, yielding marked success as drug delivery vehicles. The multiple surface modifications, such as phosphonate and polyethylenimine (PEI) have allowed for dual-delivery functions: internal packaging of anti-cancer drugs and electrostatic attraction of siRNA to target multi-drug resistant cancer cells. MSNs' utility as drug delivery vehicles has been shown effective in vitro and in vivo in multiple studies ranging from tumor suppression to treatment of multi-drug resistant cancers.[7,20] The surface modifications also allow for cell-specific targeting of MSNs, as shown by Lu et al in folate receptor targeting of cancer cells by conjugation of MSNs and folic acid. Additionally, unique packaging and release chemistries allow for the incorporation of molecules, such as membrane-impenetrable proteins and DNA, for delivery across previously unreachable areas

of the cell.[22,23] MSNs have also been employed as imaging markers due to their easily modified surface chemistry, allowing the inclusion of fluorescent dyes such as fluorescein.[24]

While the uptake of MSNs by cancer cells has been investigated in a number of studies, little is known about their ultimate fate inside the cells.[5,14,25–27] Recent literature has reported that MSNs are exocytosed from cells, however the cellular mechanism responsible for this event has not been not addressed.[28] Possible mechanisms of MSN exocytosis discussed in literature are presented in Scheme 4.1, where endocytosed nanoparticles co-localize to the lysosome and they could either enter the Golgi Apparatus for excretion or undergo lysosomal exocytosis.[21,25,26,29] In the previously mentioned study, MSN exocytosis was observed with nanoparticles that are not surface-modified.[30] Considering that coating the outer surface of MSNs with 3-(trihydroxysilyl)propyl methylphosphonate has been shown to improve nanoparticle dispersibility[14] and MSNs used for cancer therapies are have targeting or delivery functions on the external particle surface, the exocytosis study calls for the use of surface modified MSNs.

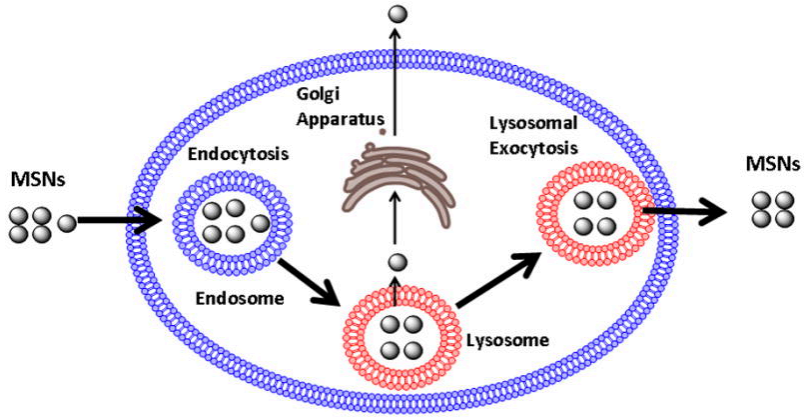

Scheme 4.1. MSN endocytosis and possible mechanisms of exocytosis. Endocytosed MSNs mainly co-localize to the lysosome. We examined two exocytosis pathways that could be responsible for MSN exocytosis, excretion through the Golgi apparatus and lysosomal exocytosis.

In this two-part study, we seek to understand the biological affects once MSNs are endocytosed. First, we examine MSNs with different surface modifications and show that

phosphonate-modified nanoparticles (Phos-MSNs) mainly use lysosomal exocytosis to exit cells. Phos-MSNs incubated with cancer cells (A549, MDA-MB 231, MDA-MB 435) can be recovered after their excretion from cells, which is mediated by fusion of lysosomes to the plasma membrane. We demonstrate that Phos-MSN exocytosis can be regulated by changing lysosomal exocytosis. Since drug release from Phos-MSNs occurs via diffusion, the resident time of the Phos-MSNs inside the cells may influence the drug release inside the cell, and we show that decreasing exocytosis improves the cytotoxicity.

4.3 Materials and Methods

Materials

All reagents were used as received without further purification. Acetonitrile (ACN), ammonium bicarbonate (ABC), anhydrous toluene, deoxycholic acid (DCA), dithiothreitol (DTT), ethanol, ethyl acetate (EA), fetal bovine serum (FBS), formic acid (FA), iodoacetamide (IAN), triethylAmine (99.5%, EMD), ethanol (200 proof, Pharmaco-AAPER), L-glutamine, methanol, penicillin, phosphate-buffered saline (PBS), polyethylene imine (PEI 1.8 kDA), streptomycin, cetyltrimethylammonium bromide (CTAB, 90%), α-cyclodextrin (α-CD, 98%), fluorescein isothiocyanate (FITC, 90%), tetraethyl orthosilicate (TEOS, 90%), and 3-(trihydroxysilyl)propyl methylphosphonate monosodium aqueous solution (HTMP, 42%) were purchased from Sigma. Ammonium nitrate and hydrochloric acid (HCl) were purchased from Fisher Scientific. Trypsin (Porcine) was purchased from Promega. 3-aminopropyltriethoxysilane (APTES, 99%) and N-(2-aminoethyl)3-aminopropyl trimethoxysilane were purchased from Gelest.

General Methods

Transmission electron microscopy (TEM) images were obtained using a JEM1200-EX (JEOL) instrument. UV-vis spectra were collected by a Cary 500 UV-vis-NIR spectrophotometer.

DLS and zeta potentials were measured by ZetaSizer Nano (Malvern Instruments Ltd., Worcestershire, U.K.).

Synthesis of Functionalized Fluorescently-Labeled MSNs

In a typical synthesis, cetyltrimethylammonium bromide (CTAB, 250 mg, 0.7 mmol) was mixed with NaOH solution (875 μL, 2 M) and H_2O (120 mL). The mixture solution was heated to 80 °C. Fluorescein isothiocyanate (2.7 mg) was dissolved in absolute EtOH (1.5 mL) and mixed with 3-aminopropyltriethoxysilane (APTES, 6 μL) for 2 hours. After the temperature had stabilized, tetraethyl orthosilicate (1.2 mL) was mixed with the ethanolic FITC-APTES solution and added to the CTAB solution. For phosphonate-coated nanoparticles, 3-(trihydroxysilylpropyl) methylphosphonate (315 μL, Phos) was added to the solution after 15 minutes. The solution was stirred vigorously at 80 °C for 2 hours. The synthesized nanoparticles were collected by centrifugation and washed with MeOH. For PEI coating, as-synthesized nanoparticles (30 mg) were suspended in a 3 mL solution of PEI (weight 0.8 kD) and ethanol (2.5 mg/mL). Particles were stirred for 30 minutes and washed three times with ethanol to remove excess PEI. For folate modified MSNs, folic acid (50 mg) was first dissolved in 5 mL DMSO and APTES (250 uL) was added to the solution. Next, *N*-hydroxysuccinimde (0.15 mg) and 1-(3-dimethylaminopropyl)-3-ethylcarbodiimide hydrochloride (0.25 mg) were added to the mixture and stirred for 2 hours. The previous solution was then added to a suspension of MSN (100 mg) and toluene (20 mL), and stirred for 20 hours at room temperature. Materials were washed twice with toluene.

Synthesis of Functionalized Iron-Core MSNs (mag@MSNs)

As previously reported by C.R. Thomas et al. J. Am. Chem. Soc. 2010, magnetic nanoparticles with Zn ion doped were synthesized using the method developed by Jang et al.[51] A typical synthesis to produce $Zn_{0.4}Fe_{2.6}O_4$ nanoparticles is as follows: $ZnCl_2$ (30 mg), $FeCl_2$ (40 mg), and $Fe(acac)_3$ (353 mg) were placed in a 50 mL three-neck round-bottom flask in the presence of

surfactants (oleic acid and oleylamine) in octyl ether. The reaction mixture was heated at 300 °C for 1 hour and the reaction products were cooled to room temperature. Upon addition of ethanol, a black powder precipitated and was isolated by centrifugation. The isolated nanoparticles were dispersed in toluene. Nanocrystals have 15 nm size with narrow size distribution ($\sigma < 5\%$). Zinc-doped iron oxide nanocrystals were dissolved in chloroform at a concentration of 50 mg/mL. One milliliter of the iron oxide nanocrystals in chloroform was added to a solution of 100 mg cetyl trimethylammonium bromide (CTAB, Aldrich, 95%) in 5 mL of water. The mixture was sonicated and the chloroform was boiled off from the solution with rapid stirring. The CTAB-stabilized zinc-doped iron oxide nanocrystals were added to an 80 °C solution of 43 mL distilled water with 350 μL of 2.0 M NaOH, and 500 μL tetraethyl orthosilicate (TEOS, Aldrich, 98%) was slowly added. After 15 minutes, 125 μL 3-(hydroxysilylpropyl) methylphosphonate was added. Following two hours of rapid stirring at 80 °C, the magnetic-core silica nanoparticles were collected by centrifugation and washed with ethanol and water. The CTAB was removed by dispersing the as-synthesized materials in a solution containing 133.3 mg ammonium nitrate and 50 mL 95% ethanol. This mixture was heated to 60 °C for 15 minutes, then the particles were collected by centrifugation and washed with ethanol. The fluorescent functionality for optical monitoring of the nanoparticles in cells, fluorescein isothiocyanate, was attached to the mesoporous silica framework. 3 mg fluorescein isothiocyanate (FITC, Sigma, 90%) was dissolved in 1 mL ethanol, and 12 μL 3-aminopropyltriethoxysilane (3-APTES, Aldrich, 98%) was added. This solution was reacted under nitrogen for 2 hours, then added to the 80 °C solution of aqueous sodium hydroxide. After 10 minutes, the CTAB-ZnNC solution was added, and the procedure followed in the same manner as above.

Cell Culture

The human cancer cell line A549 was obtained from American Type Culture Collection and was maintained in Dulbecco's modified Eagle's medium (DMEM; GIBCO) supplemented with 10% fetal bovine serum, 1% L-glutamine, 1% penicillin and 1% streptomycin stock solutions. Human cancer cell lines MDA-MB 231 and MDA-MB 435 were a gift from Dr. Neil O'Brien at UCLA and were maintained RPMI-1640 medium (CellGro) supplemented with 10% fetal bovine serum. The media were changed every three days, and the cells were passaged by trypsination before confluence. The human embryonic stem cell line H9 was cultured as previously described. Briefly, human embryonic stem cells were cultured in DMEM/F-12 medium supplemented with 20% Knock-out serum replacement (Gibco), 1% non-essential amino acids, 0.5% L-glutamine, 1% penicillin-streptomycin, 100 μM ß-mercaptoethanol, and 4 ng/mL bFGF. hESC cultures were maintained on feeder layers of inactivated murine embryonic fibroblasts (MEFs). For nanoparticle uptake experiments hESCs were plated on Matrigel (BD Biosciences) and fed with MEF-conditioned medium.

Human fibroblast cell line HFF, human lung cancer cell line A549, and human breast cancer cell line MCF7 were purchased from American Type Culture Collection. Each line was grown and maintained in Dulbecco's modified Eagle's medium (DMEM; GIBCO) with 10% FBS, 1% L-glutAmine, 1% penicillin, and 1% streptomycin.

Mag@MSN Transmission Electron Microscopy (TEM)

Cells were seeded in a 6-well plate at a confluency of 4 x 10^5 cells per well overnight. The next day, cells were treated with 20 μg/mL MSNs for two hours and then the media was changed with fresh growth media. After 24 hours incubation, the media from the six wells was collected and mixed in a culture flask. A NdFeB magnet was placed on the wall of the flask to immobilized the

nanoparticles, the media was removed and the nanoparticles were washed with PBS. TEM was performed on the isolated nanoparticles.

Fluorescent Microscopy for Lysosome Staining and Golgi Apparatus Staining

The fluorescence of the nanoparticles at an excitation wavelength of 488 nm was used to confirm the cellular uptake of the MSNs. The cells were incubated in an eight-well Lab-Tek chamber slide system (Nalgel Nunc International) with the nanoparticles and then washed with PBS to remove the nanoparticles that did not enter the cells. The cells were washed with PBS, fixed with 4% paraformaldehyde for 15 minutes, permeabilized with 0.2% Triton X-100 in PBS for 10 minutes, and blocked with 1% BSA in PBS for 1 hour. Anti-LAMP1 (Abcam ab24170) antibody was added (2 μg/mL) and incubated overnight at 4 °C. Staining with secondary antibody tagged with DyLight 594 (Abcam ab96885) was done for 1 hour at room temperature. The cells were then stained with DAPI solution for nuclear staining and pictures were taken using a fluorescent microscope.

For Golgi apparatus staining, cells were seeded in a four-well chamber slide and treated with Exo 1 (50 μM) and Brefeldin A (5 μM) for 6 hours. Cells were prepared similar to the lysosome staining procedure previously described. Anti-golgin 97 antibody (Invitrogen CDF4) was used for staining (5 μg/mL). Staining with secondary antibody tagged with FITC was done for two hours at room temperature.

Nanoparticle-Cell Incubation

Cells were seeded at a confluency of 400,000 cells in 2 mL of media per well in 6-well plates and incubated overnight. Zn-doped mag@MSNs (Bare, Amine, phosphonate or PEI coated) were added to the cells at 80 mg/mL and incubated for 2 hours. Media was removed and treated for nanoparticle isolation. Cells were washed twice with PBS, suspended in fresh growth media, and further incubated for 24 hours to allow nanoparticle exocytosis. Media was collected, with three 6-well plates used for each MSNs coating within each of the three cell lines for a total of 36 mL.

Mag@MSNs isolation was conducted by utilizing a neodymium magnet in a 25 mL cell culture flask for each sample condition. From each 36 mL solution, 6 mL were incubated with the magnet for 1 hour, followed by careful extraction of media, avoiding perturbance of the magnet. This was repeated until nanoparticle isolation was completed on all 36 mL of media. Nanoparticles were washed two times with PBS, resuspended in 1 mL PBS, isolated with a magnetic rack, and resuspended in 50 mL PBS.

MSN Exocytosis Measurement by Flow Cytometry

Cells were seeded in a six-well plate at a confluency of 4 x 10^5 cells per well overnight. Cells were incubated with 20 μg/mL of MSN (or iron core MSN) for 2 hours, then washed with PBS and either incubated in growth media for different time points or treated with inhibitors for 6 hours (LY294002 250 nM, Nocodazole 10 μM, Cytochalasin D 20 μM, Bafilomycin A1 100 nM). After incubation, cells were trypsonized, washed with 0.05% tryphan blue solution to decrease the background fluorescence and washed two more times with PBS. Flow cytometry was performed measuring the green fluorescent inside the cells, which corresponds to the fluorescence of the MSNs.

ICP-OES Analysis

A549 cells were seeded in a 6-well plate at a confluency of 4 x 10^5 cells per well. Cells were treated with 40 μg/mL MSNs for two hours and then the media was removed and the cells washed with PBS two times. Fresh growth media was added to the cells and incubated for 24 hours. The cell media was collected, the cells washed with 2 mL of PBS, and the PBS wash was combined with the cell media for ICP-OES analysis. In a typical ICP-OES run, cell culture washes were digested by adding an equal volume of 70% nitric acid (Aldrich), and heated at 80 °C for 3 hours. Digested solutions were sonicated for 15 minutes with stirring to ensure sample homogeneity and diluted to a 5% nitric acid concentration. Runs were standardized through serial dilutions of a stock solution of

1000 μg/mL silicon in 5% nitric acid (Fisher). Samples were run on a Thermo Jarrell Ash IRIS 1000 ICP-OES instrument, and silicon concentration determined through monitoring the emission at 251.611 nm.

β-Hexosaminidase Assay

Cells were seeded in a twelve-well plate at a confluency of 3 x 10^5 cells per well overnight. The media was removed from the wells, the cells were washed with PBS and fresh media was added to the wells. The cells were incubated for 6 hours with or without inhibitors (LY294002 250 nM, Nocodazole 10 μM, Cytochalasin D 20 μM, Bafilomycin A1 100 nM). The media (supernatant) was collected and the cells were lysed with 0.1% Triton X 100 in DMEM. The β-hexosaminidase assay was performed in a 96-well plate by mixing 50 μL of 2 mg/mL 4-nitrophenyl N-acetyl-β-D-galactosaminide in 0.1 M citrate buffer (pH 4.5) with 75 μL of supernatant or cell lysate and incubating for 1 hour at 37 °C. After the incubation, 100 μL of 0.2 M borate buffer (pH 9.8) was added to the mixture to stop the reaction. The absorbance was read at 405 nm using a plate reader. Percentage values were obtained by dividing the reading from the supernatant with that of the cell lysate.

Cell Killing Assay

Cells were seeded in a 96-well plate at a confluency of 5 x 10^3 cells per well overnight. The next day, cells were treated with Bafilomycin A1 (12.5 nM), U1866A (2.5 μM), CPT-loaded MSNs, and the combinations of MSN-CPT and Bafilomycin A1 or U18666A for 24 hours. Cells were washed with PBS and incubated in DMEM with 10% WST-8 solution (Dojindo Co) for 3 hours. The absorbance of each well was measured at 450 nM in a plate reader.

4.4 Results & Discussion

Initial studies to understand the nanoparticle exocytosis began with examining the uptake of fluorescein labeled, phosphonated MSNs (Phos-MSN) into lung cancer cell line A549 by flow cytometry analysis. Fluorescein-labeled MSNs were synthesized by a co-condensing fluorescein isothiocyanate via a sol-gel method and the surface was modified with 3-(trihydroxysilyl)propyl methylphosphonate to make the surface more negatively charged and easily disperse in media (Figure 4.1 A).[4,5,31] Each particle has an average diameter of ~100 nm and pores with diameters of 2-3 nm. As shown in Figure 4.1 B, the green fluorescence of Phos-MSNs can be detected inside the cell 2 hours after their addition into the media. The fluorescence largely co-localizes with the staining of anti-LAMP1 antibody, suggesting that they are inside the lysosomes. Upon further incubation, the fluorescent signal inside the cell decreased, indicative of MSNs being exocytosed (Figure 4.2). To quantify Phos-MSN fluorescence inside the cells by flow cytometry, A549 cells were incubated with MSNs for 2 hours, and washed twice with PBS before adding fresh media for further incubation (6, 24, and 48 hours). As seen in Figure 4.1 C, the fluorescence inside the cells increased after incubation with MSNs for 2 hours due to nanoparticle uptake, but this fluorescence dramatically decreased after 6 hours and reached almost basal level after 24 and 48 hours, suggesting particles had completely exited the cells. There was a progressive decrease in fluorescence, 65%, 82%, and 95%, inside the cells after 6, 24, and 48 hours, respectively (Figure 4.1 C). Quantitative results were obtained with ICP-OES, in which the silicon (Si) concentration inside the cells was measured after Phos-MSN endocytosis and compared to the Si concentration in the cell media after 24 hours to detect of exocytosed MSNs. We discovered that a total mass of 5 μg of Si was endocytosed by 4 x 10^5 cells after 2 hours of treatment with MSNs, while 4.7 μg of Si were exocytosed and detected in the cell media 24 hours later (Figure 4.1 D).

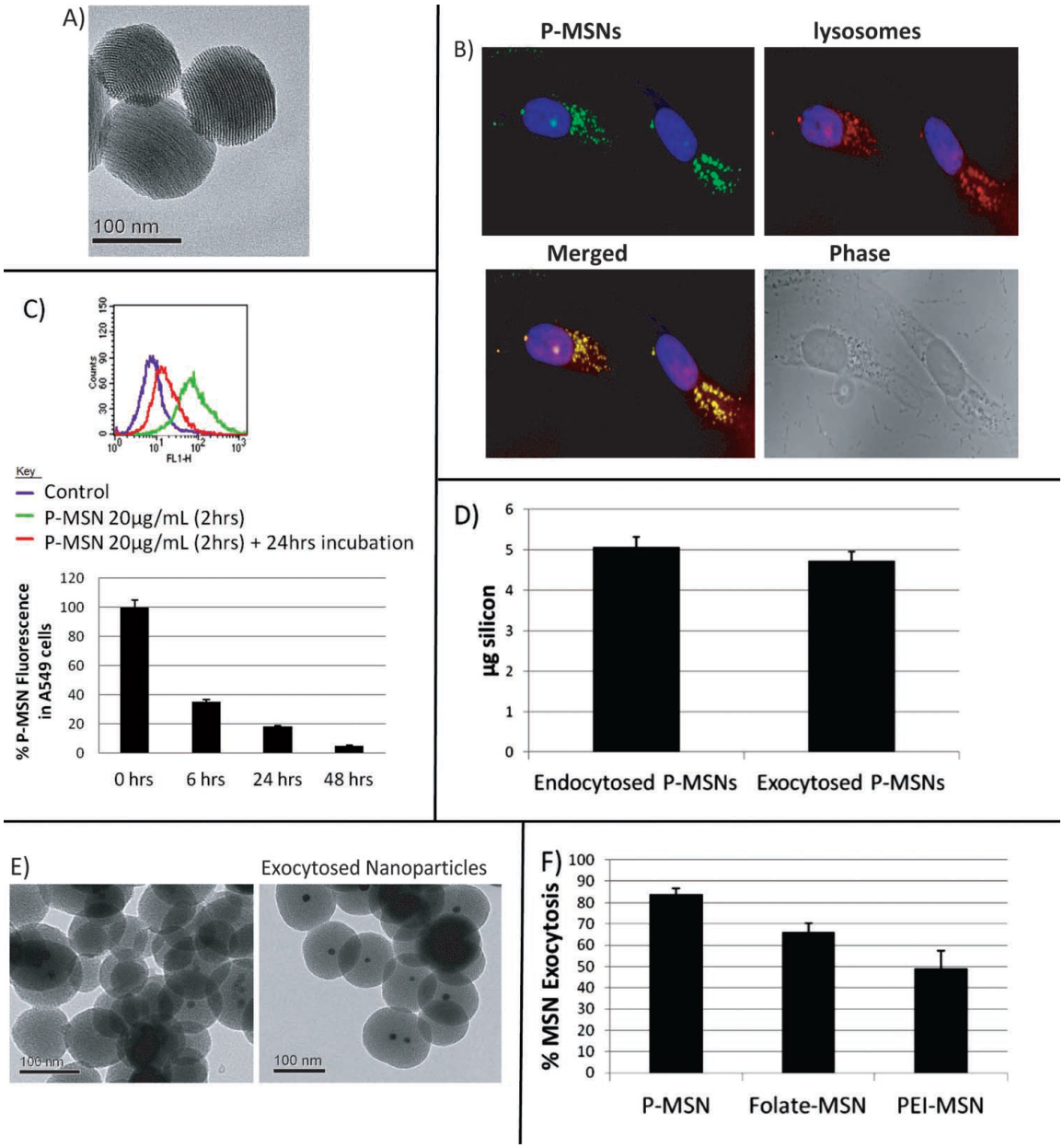

Figure 4.1. Exocytosis of MSNs from A549 cells. A) TEM pictures of phosphonate modified MSNs used for exocytosis experiments; B) Fluorescent microscopy analysis detecting the Phos-MSNs' fluorescence inside the cells after 2 hours treatment with the nanoparticles and staining of lysosomes with lyso-Tracker Red. MSNs (green), Lysosomes (red), Nucleus (blue); C) Flow cytometry analysis of A549 cells treated with MSNs for 2 hours, washed with PBS, and incubated for an additional 6, 24, and 48 hours; D) ICP-OES analysis of MSNs endocytosed by A549 cells after 2 hours and MSN exocytosis after 24 hours; E) TEM images of zinc-doped iron core MSNs (mag@MSNs) before being added to cells (left) and collected with a magnet after being exocytosed by cells (right); F) ICP-OES analysis to measure the exocytosis of phosphonated, PEI-coated, and folate modified mag@MSNs.

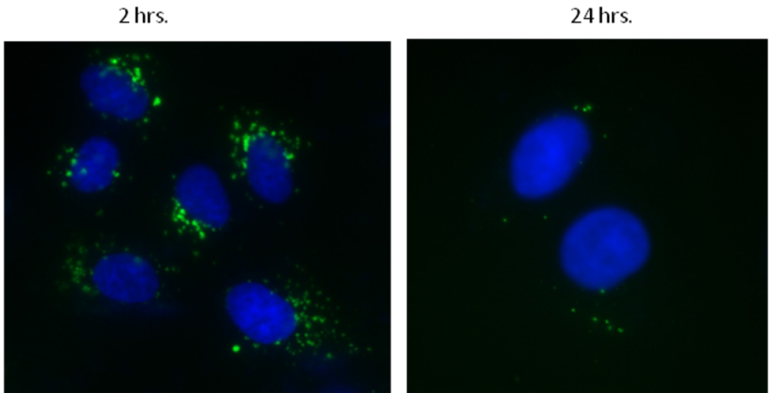

Figure 4.2. The fluorescence of MSNs inside A549 cells, after 24 hours incubation, is much less when compared to the fluorescence seen after 2 hours.

In order to examine the nanoparticles after exocytosis, MSNs containing magnetic cores were synthesized (mag@MSN) that could be easily recovered by magnetic manipulation.[32] These nanoparticles were prepared by forming a mesoporous silica shell around the zinc-doped iron oxide nanocrystal core (Figure 4.1E, left), which have similar size and the same surface modifications (fluorescein and phosphonate attachment) as MSNs used in the previous experiments.[8,15] Phos-mag@MSNs were endocytosed and excreted from A549 cells in a similar manner as seen with Phos-MSNs without zinc-doped iron oxide core (Figure 4.3). The exocytosed mag@MSNs were collected from the media using a neodymium (NdFeB) magnet. TEM analysis of the exocytosed iron oxide core MSNs (Figure 4.1 E, right panel) show intact and organized pores, similar in appearance with the Phos-MSNs added to the media (Figure 4.1 E, left panel). These results demonstrate the Phos-MSNs excreted from cells can be collected and their structural integrity is preserved.

Specialized types of surface-modified MSNs that have been developed for delivery were also tested. In particular, PEI-coated MSNs that are used for siRNA delivery, as well as MSNs modified with folate used to target tumors.[11,17,25] The specialized MSNs were also exocytosed, but at a slower rate (Figure 4.1 F). PEI- or folate-coated MSNs were incubated with A549 cells and the amount of MSNs that had been exocytosed after 6 hours was quantitatively compared to Phos-MSNs by ICP-

OES. After 6 hours of incubation, 84% of the Phos-MSNs had been exocytosed from the cells, compared to 66% of the folate-MSNs and 49% of the PEI-MSNs, respectively (Figure 4.1 F). This suggests that although different surface modifications can affect the exocytosis rate of MSNs, they are still able to exit the cells. For the remainder of this part of the work, we chose Phos-MSNs to focus on to investigate the exocytosis mechanism.

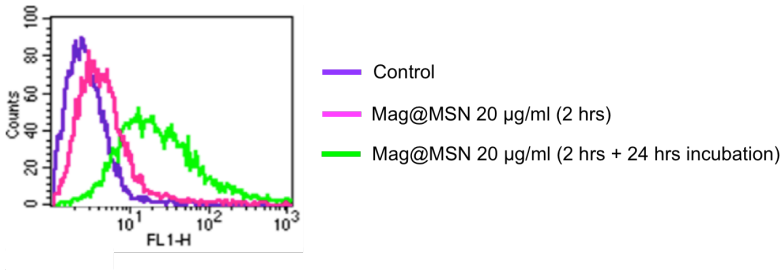

Figure 4.3. Flow cytometry analysis of zinc-doped iron core MSNs (mag@MSN) demonstrates that they are exocytosed from A549 cells.

A number of human cell lines were tested to compare the exocytosis of Phos-MSNs among them. The cell lines screened were lung cancer cell line A549, and breast cancer cell lines MDA-MB231, MCF-7 and MDA-MB435, the pancreatic cancer cell line PANC-1, as well as the human embryonic stem cell line H9. The various cells were subjected to the same procedure as initial studies with A549. Briefly, cells were incubated with fluorescently labeled Phos-MSNs for 2 hours and washed with PBS to remove the remaining Phos-MSNs. Flow cytometry was performed immediately after MSN uptake and after 24 hours incubation, to determine the percentage of nanoparticles exocytosed. Results shown in Figure 4.4 demonstrate there are variations in the rate of Phos-MSN exocytosis among different cell lines. The highest exocytosis efficiency begins with A549 cells having the highest excretion at 87% followed by MDA-MB231 (81%), PANC-1 (75%), MCF-7 (61%), MDA-MB 435 (36%), and H9 (4%). The H9 cells had the lowest Phos-MSN exocytosis, suggesting Phos-MSNs remain inside embryonic stem cells for days and are slow to exocytose with

respect to other cell lines. These results are consistent with reports that MSNs can be used to label human mesenchymal stem cells, which can be tracked *in vivo* for several days after transplantation into mice.[26–28]

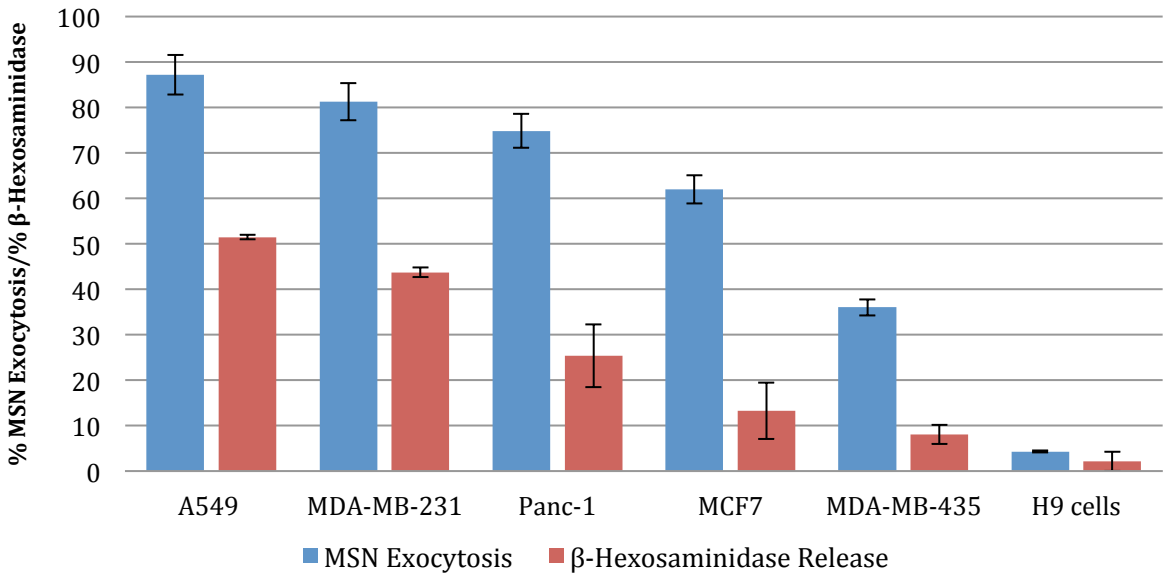

Figure 4.4. Correlation of phosphonated MSN exocytosis and lysosomal exocytosis. The exocytosis of MSNs based on flow cytometry analysis in different cell lines and correlation with lysosomal exocytosis by measurement of β-hexosaminidase release from A549 cells.

To further delve into the understanding of cell exocytosis, it is necessary to understand the internal functions inside the cell, such as lysosomal exocytosis. Lysosomal exocytosis is the fusion of the lysosomal membrane with the plasma membrane, resulting in the release of lysosome components out of the cell. This mechanism has been observed in a variety of cells and is thought to be involved in membrane repair, acquisition of metastatic potential in cancer cells, and resistance to autophagy-induced cell death.[33,34] The fusion of lysosomes with the plasma membrane has been reported in hepatocytes, fibroblasts, epithelial cells and cancer cells.[35] Lysosomal exocytosis can be detected by measuring the release of β-hexosaminidase, an enzyme that resides inside lysosomes, into the cell culture media. Enzyme assays for the release of β-hexosaminidase revealed that A549

cells and MDA-MB 231 cells have a relatively high rate of lysosomal exocytosis with 51% and 44% of the enzyme being released after 24 hours of incubation, respectively. Alternatively, the cell line PANC-1 had 25%, MCF-7 had 13%, while MDA-MB 435 and H9 had less than 10% enzyme secretion (Figure 4.4). The ability of these cells to secrete β-hexosaminidase correlates well with the order of excretion of MSNs, which suggests lysosomal exocytosis plays a critical role in these cell lines' exocytosis of MSNs.

The Golgi apparatus is integral in cell secretion, and its role in the exocytosis of Phos-MSNs was tested. A549 cells were treated with Exo1 and Brefeldin A, two compounds known to inhibit protein exocytosis by causing collapse of the Golgi apparatus.[36–39] Flow cytometry was performed 6 hours later to monitor the effects of the compounds on MSN exocytosis (Figure 4.5A, left panel). Our results show that treated cells were able to exocytose MSNs as efficiently as the control cells, although the Golgi had collapsed by treatment with Brefeldin A or Exo1 (Figure 4.5A, right panel) as demonstrated by Anti-golgin 97 staining and fluorescence microscopy. These results suggest that disruption of the Golgi apparatus does not have a significant effect on MSN excretion by cells.

Our results support the idea that Phos-MSNs are first localized in the lysosome and then exocytosed by lysosomal exocytosis. However, there are observations of a minor population of MSNs that does not co-localize with the lysosomes.[7,25,27,40] This observation is likely dependent on the type and quantity of MSNs used, time of incubation, and cell lines utilized. Further work is necessary to examine whether they represent a minor population of MSNs that escape lysosomes and if they utilize a different pathway for their exocytosis.

Subsequently, inhibitors of lysosomal exocytosis were used to further investigate Phos-MSN exocytosis and attempt to pinpoint the lysosomal exocytosis mechanism. Our results show that a number of reagents that inhibit lysosomal exocytosis, such as Cytochalasin D, Bafilomycin A1, Nocodazole and LY294002, also inhibit Phos-MSN exocytosis. As shown in Figure 4.5B, we found

that inhibition of lysosome acidification by Bafilomycin A1 can inhibit Phos-MSN exocytosis. We also found that Nocodazole, which inhibits microtubule formation, and Cytochalasin D that inhibits actin polymerization, both prevent Phos-MSN exocytosis. A probable explanation is that the actin polymerization and microtubule formation are required for transport of the lysosomes to the periphery and fusion with the plasma membrane.[41–43] Signaling through the lipid kinase PI3K is also important for lysosomal exocytosis as it leads to an increase in cytosolic Ca^{2+}, resulting in the fusion of lysosomes with the plasma membrane. The use of PI3 kinase inhibitors has been shown to decrease lysosomal exocytosis[44] and we found that LY294002, a PI3 kinase inhibitor, also causes inhibition of Phos-MSN exocytosis (Figure 4.5B).[45]

Because reagents were added to the cells only after the Phos-MSNs had been endocytosed, the inhibitors will only affect the exocytosis of the nanoparticles and not the endocytosis. To confirm that these inhibitors were in fact blocking lysosomal exocytosis, the release of β-hexosaminidase from cells was measured. After 6 hours incubation, the control cells secreted approximately 23% β-hexosaminidase, whereas the cells treated with LY294002 and Nocodazole secreted approximately 16% and 14%, respectively (Figure 4.6). Cells treated with Cytochalasin D and Bafilomycin A1, the secretion was less than 5% (Figure 4.6). There is good correlation between lysosomal exocytosis inhibition and its effects on Phos-MSN exocytosis, which further supports the majority of Phos-MSNs are excreted by lysosomal exocytosis.

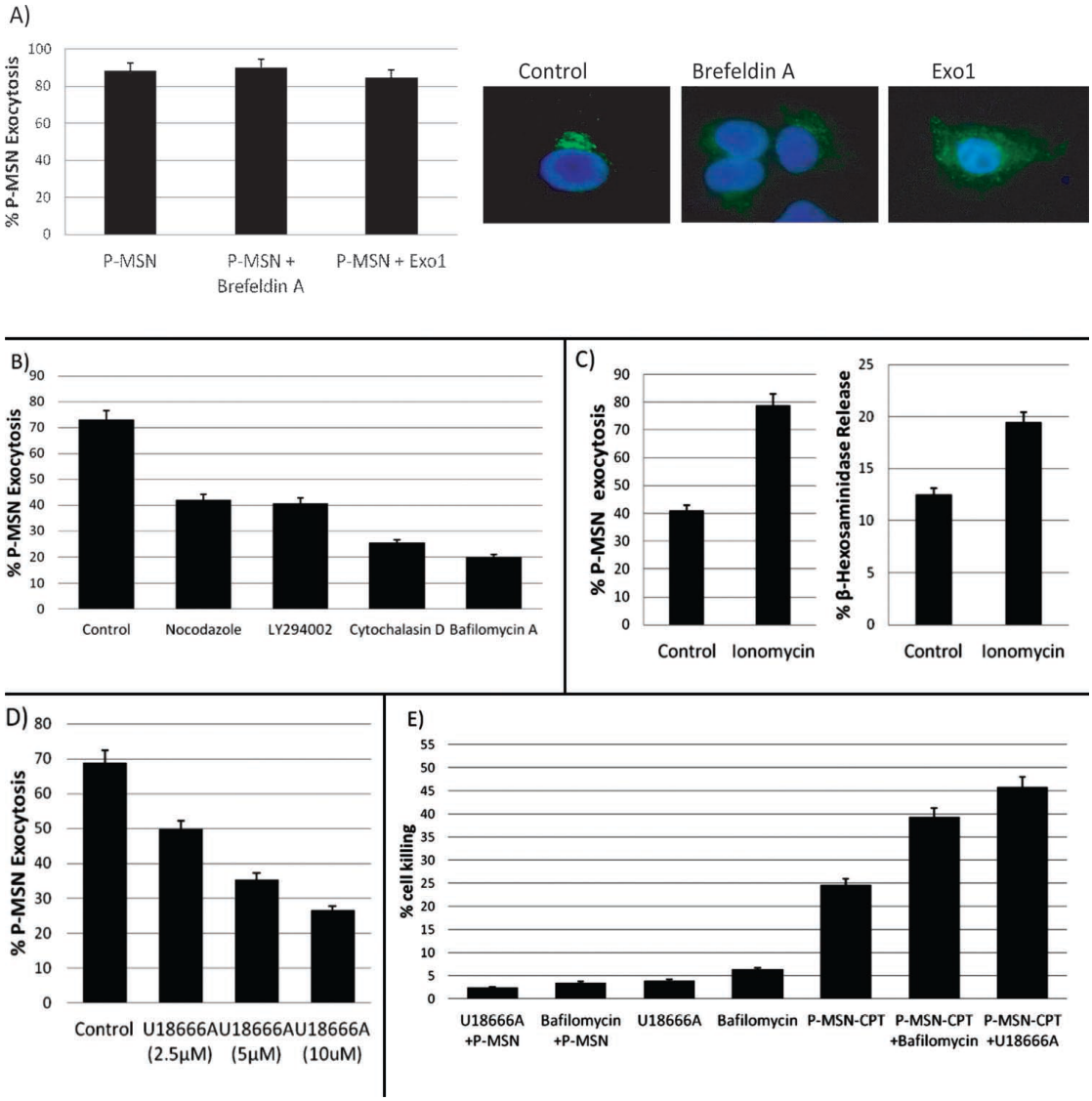

Figure 4.5. A) Measurement of Phos-MSN exocytosis by flow cytometry of A549 cells treated with Brefeldin A (10 μM) and Exo1 (50 μM) (left panel). Right panel shows that Brefeldin A and Exo1 disrupt the Golgi apparatus (stained with green anti-golgin 97); B) A549 cells were treated with Nocodazole (20 μM), Cytochalasin D (20 μM), Bafi lomycin A1 (100 nM), and LY294002 (2 μM). Flow cytometry was performed to determine the effect of these inhibitors on exocytosis; C) Cells treated Phos-MSNs for 2 hours and 10 μM Ionomycin was added for 2 hours to accelerate Phos-MSN exocytosis (left). Treatment with Ionomycin also increased the lysosomal exocytosis (right); D) Treatment with U18666A impeded Phos-MSNs exocytosis in a dose dependent manner; E) Cell killing enhancement of Phos-MSNs loaded with CPT by impeding Phos-MSN exocytosis with Bafilomycin A (12.5 nM) and U18666A (2.5 μM). Cells were treated with Phos-MSN loaded with CPT for a final concentration of 50 nM CPT and Bafilomycin A and U18666A for 24 hours.

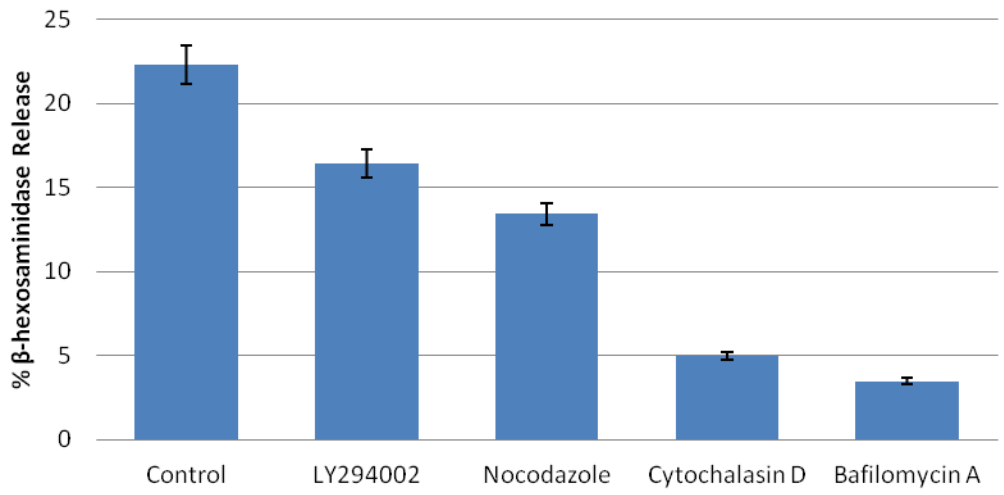

Figure 4.6. The release of β-hexosaminidase into the media of cells was measured as an indicator of lysosomal exocytosis. LY294002, Nocodazole, Cytochalasin D, and Bafilomycin A inhibit this process.

The fusion of the lysosomal membrane with the plasma membrane depends on synaptotagmin VII, which is a transmembrane protein that upon binding calcium, undergoes a conformational change that allows it to bind to the SNARE complex on the plasma membrane, facilitating membrane fusion.[45,46] To study the effects of increased intracellular calcium concentration on MSN exocytosis, cells were treated with Ionomycin, an ionophore that transports calcium into the cells. As shown in the left panel of Figure 4.5 C, the Ionomycin treatment accelerated MSN exocytosis by 80%, after only 2 hours of incubation. The increase in lysosomal exocytosis corresponded with the Ionomycin treatment, as evidenced by an increase in β-hexosaminidase release (Figure 4.5C, right panel). These results suggest that acceleration of lysosomal exocytosis also accelerates Phos-MSN exocytosis.

U18666A, a class 2 amphiphile known to alter cholesterol accumulation and affect different intracellular trafficking pathways, impedes MSN exocytosis in A549 cells. Treatment of cells with U18666A mimics the cellular effects of Niemann-Pick disease type C1 (NPC1), a neurodegenerative disease characterized by excess accumulation of cholesterol in the lysosomes.[47,48] This compound

can alter the calcium concentration in lysosomes.[49] A549 cells were pre-treated with U18666A for 18 hours and then MSNs were added for 2 hours. After rinsing the cells with PBS, the cells were incubated for an additional 6 hours. Treatment with U18666A markedly decreased MSN exocytosis in A549 cells in a concentration dependent manner (Figure 4.7). Furthermore, this compound also inhibited lysosomal exocytosis, which is further proof positive that lysosomal exocytosis is vital for Phos-MSN exocytosis (Figure 4.6).

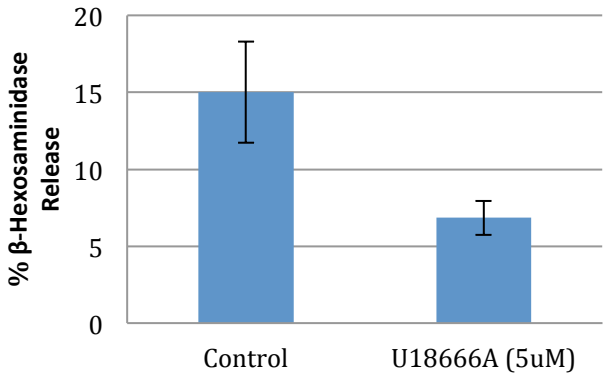

Figure 4.7. Inhibition of lysosomal exocytosis by U18666A in A549 cells. Cells were treated with U18666A for 6 hours and then β-hexosaminidase release was measured.

As the amount of time that the MSNs remain inside the cells could affect the drug delivery efficacy, we used MSNs loaded with camptothecin (CPT), a well-known anti-cancer drug. Longer MSN retention times would allow for more drug to be released inside the cells, thereby increasing cytotoxicity. Additionally, some cell lines carry out MSN exocytosis faster than others, which raises the possibility that slowing down the exocytosis of Phos-MSN could enhance its efficacy for drug delivery. In order to test this hypothesis, we treated the lung cancer A549 cells with CPT-loaded Phos-MSNs in the presence of Bafilomycin A1 or U18666A for 24 hours and cell killing assays were performed. As shown in Figure 4.5E, the cytotoxicity of the CPT-loaded Phos-MSNs increased significantly. These results When Phos-MSN exocytosis is inhibited by Bafilomycin A1 or U18666A, cell killing by camptothecin (CPT)-loaded Phos-MSNs is enhanced, which are in line with the idea

that longer retention time inside the cell enhances intracellular drug release that leads to more cell killing.

4.5 Conclusion

In summary, our results provide convincing evidence that Phos-MSNs are exocytosed from cells after cellular uptake and MSNs incubated with varied cell types resulted in the identification of several cell line-specific proteins. First, the exocytosis of Phos-MSNs is demonstrated by measuring the fluorescein fluorescence inside the cells through flow cytometry and by fluorescence microscopy, as well as by ICP-OES analysis. Mag@Phos-MSNs exocytosed from cells were recovered by using a magnet and TEM analysis showed that exocytosed particles are similar in shape and appearance to the particles before cellular uptake. We observed good correlation between Phos-MSN exocytosis and lysosomal exocytosis in different cell lines, and inhibition of lysosomal exocytosis decreased MSN exocytosis. Acceleration of lysosomal exocytosis with Ionomycin accelerated MSN exocytosis in A549 cells. These results suggest that MSNs primarily use lysosomal exocytosis to exit cells. Finally, we have shown that combining CPT-loaded MSNs with Bafilomycin A1 or U18666A enhances the cell-killing efficacy of the nanoparticles. The rate of MSN exocytosis is important for drug delivery and should be taken into account when designing surface modified MSNs for cancer therapy.

4.6 Protein Corona Composition of Surface-Modified Mesoporous Silica Nanoparticles

In a second study, magnetic core MSNs (mag@MSNs) of varied surface modifications are incubated with distinct human cell lines. Proteomic analyses confirmed that, while many proteins are present in the coronas of MSNs incubated with different cell lines (A549, HFF, or MCF7), there are clear differences in the protein coronas composition that are unique to each cell line. Additionally, we found that there are differences in corona composition dependent upon surface modification (both specific modifications and generalized zeta-potential classes) within a given cell line.

The protein corona is the evolution of multiple layer(s) of proteins that interact and bind to the nanoparticle surface. Layers within the protein corona identifying a longer-lived "hard" corona as well as a loosely attached layer of proteins that make up the "soft" corona.[51,52] This hard corona contains information from the biological fluid the NPs are first exposed to, while proteins from the second biological fluid are identified as well.[53] Existing concerns on how the corona might interfere with nanoparticle functions, such as cell targeting and drug delivery have arisen in recent literature.[54] Other groups have observed that protein binding does have an effect on nanoparticle distribution, however whether these effects are beneficial or harmful is still under debate.[55] Positive effects such as enhanced blood-brain barrier (BBB) crossing abilities have been identified, but consequences such as more rapid clearance by filtering and excretory organs are known to exist, as well.[55–58] Further studies have looked at myriad of NP types and probed corona composition in correspondence with nanoparticle size and surface composition, finding significant effects on corona composition attributed to differences in each of these properties. Gref et al observed that increasing the length (or MW) of poly(ethylene glycol) (PEG) chains on the surface of NPs resulted in a reduction in protein adsorption, prevention of uptake by cells, and overall, changing the wt % PEG resulted in some alteration in protein corona composition.[59] Lundqvist et al (2008) found that increasing the diameter of the nanoparticle itself can alter the protein corona.[51] These studies have indicated the potential importance of these findings in terms of uptake pathway and efficacy effects; however, we propose an alternative use for protein corona composition analysis that takes advantage of these distinct differences.

We synthesized mag@MSNs of various coatings to examine the protein corona that evolves on the surface of the silica. Unmodified silica was used a control, while the other coatings were chosen for their application in cell studies: phosphonated MSNs to enhance dispersability in various media, Amine coated to provide an alternate charge and different loading properties, and

poly(ethylene imine) coated that have been used in siRNA delivery.[10,60] The materials were grouped based on the overall surface charge, or ζ-potential, as the electrostatic charges are the primary distinguishing factor on the MSNs for proteins to adsorb onto the surface. Bare MSNs have a negative potential of -16 mV, while phosphonated MSNs (Phos-MSN) are -33 mV. Amine-coated MSNs (Amine-MSN) have a positive z-potential of +31 mV, while poly(ethylene imine)-coated MSNs (PEI-MSN) have a +50 mV. Samples were incubated with one of three cell lines: HFF, A549, and MCF7, exocytosed, collected with a magnet, and subjected to a trypsin digest. Mass spectrometry was run on the digested samples and data processing software was used to help identify proteins. As an alternate method of testing, the cells were subjected to a Western blot analysis.

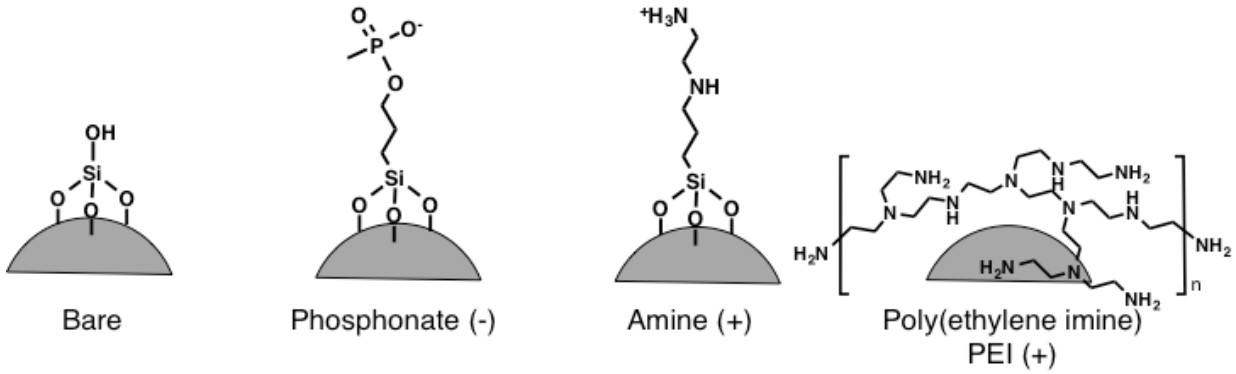

Figure 4.8 Surface coatings on MSNs used. Bare silica and phosphonate are both negatively charged, while amine and poly(ethylene imine) are positively charged.

4.7 Materials and Methods

Surface Functionalization of Mag@MSNs.

Mag@MSNs were functionalized with amines by suspending 100 mg in anhydrous toluene and N-(2-aminoethyl)3-aminopropyl trimethoxysilane (55 μL) was added. The solution was heated to 80 °C and left to react overnight. Materials were washed twice with each toluene, methanol, and water.[61] For the phosphonate coating, nanoparticles (100 mg) were suspended in water and

(trihydroxysilylpropyl)methylphosphonate (300 μL) was added to the solution to react overnight. The particles were collected via centrifugation and washed in water. For the electrostatic PEI coating, as-synthesized nanoparticles (30 mg) were suspended in a 3 mL solution of PEI (weight 1.8 kD) and ethanol (2.5 mg/mL). Particles were stirred for 30 minutes and washed three times with ethanol to remove excess PEI.

Protein Digest

Samples of Mag@MSNs in 50 mL PBS were placed in a magnetic rack to isolate protein-bound particles at room temperature (RT). After 20 minutes, 50 mL PBS were pipetted out, avoiding disturbance of isolated particles. Particles were resuspended in 90 mL mass spectrometry (MS)-grade H_2O for further washing, and placed into a magnetic rack for 20 minutes at RT. After 20 mintues, 90 mL MS-grade H_2O were pipetted out, avoiding disturbance of isolated particles. Particles were resuspended in 90 mL 200 mM ABC and 0.1% DCA in MS-grade H_2O.

Reducing agent DTT, at a concentration of 30 mM in 200 mM ABC and 0.1% DCA, was added to particle solutions to a final concentration of 3 mM DTT, and sample solutions were incubated at 95 ^{o}C for 30 minutes in the dark with moderate mixing (300 rpm). Alkylating agent IAN, at a concentration of 100 mM in 200 mM ABC and 0.1% DCA, was added to particle solutions to a final concentration of 7.4 mM IAN, and sample solutions were incubated at 37 ^{o}C for 1 hour in the dark with moderate mixing (300 rpm). To quench the reaction, 30 mM DTT in 200 mM ABC and 0.1% DCA was added to the solutions to a final concentration of 4 mM DTT. A quantity of 200 mM ABC and 0.1% DCA was added to bring the final reaction concentrations to 3.7 mM DTT and 6.5 mM IAN. Lyophilized trypsin was suspended in 10 mM HCl to a final concentration of 0.5 mg/mL Trypsin. Trypsin was added to sample solutions in a ratio of 1 mg trypsin: 100 mg protein and incubated overnight at 37 ^{o}C in the dark with moderate mixing (300 rpm). Sample solution tubes were placed into a magnetic rack at RT for 20 minutes to isolate

particles from the digested peptide mixture. Digest volume without Mag@MSNs was pipetted into a new tube.

Prior to MS analysis, DCA was removed from sample solutions. A volume of 125 mL 95.5% EA and 0.5% FA was added to the sample solution, lightly vortexed for 5 seconds, and a subsequent volume of 800 mL 100% EA was added. The solution was strongly vortexed for 10 s and centrifuged at 13,200 rpm for 10 minutes at RT. The top organic layer was removed, avoiding disturbance of the bottom aqueous layer. This procedure was repeated twice. The residual aqueous solution was dried down under vacuum at RT for 10 minutes in a Thermo Scientific SpeedVac®. Samples were subsequently resuspended in 50 mL 50% methanol in MS-grade H_2O. This procedure was repeated twice. Samples were resuspended in 40 mL 0.5% FA in MS-grade H_2O.

Mass Spectrometry

All samples were run on a Waters nanoACQUITY nano ultra-performance liquid chromatography (nanoUPLC) system (Manchester, UK). Separation was conducted with a UPLC symmetry C18 180 mm x 20 mm trap column and a nanoACQUITY UPLC BEH C18 75 mm x 150 mm reversed phase (RP) analytical column. MS-grade H_2O and 0.1% FA comprised the aqueous mobile phase (A). ACN and 0.1% FA comprised the organic mobile phase (B). A total of 5 mL per sample were injected onto the trap column, subjected to a 97% A and 3% B wash for 5 minutes, followed by injection onto the analytical column in 3% B. A 70 minutes 3-50% B gradient was used, followed by a 3 minutes 50-95% B gradient. A 15 minutes rinse with 95% B was followed by a 20 minutes re-equilibration period with 97% A.

The nanoACQUITY unit was interfaced with a Waters Xevo quadruopole time-of-flight (QTOF) mass spectrometer. Data acquisition was conducted in a data-independent (MS^E), positive ion mode over a 100-8000 m/z range. MSE involves a non-selective and continuous process

alternating between low and high collisional energies per second, allowing for observation of resulting precursor and associated fragment ion spectra and maximizing protein identification.

Data Analysis

Waters ProteinLynx Global Server 2.5.2 (PLGS) was used to process data. All data were searched against UniProtKB-SwissProt *Homo sapiens* (Human) database for protein identifications. Parameters were set to a minimum of 7 peptides per protein identification, 2 missed cleavages, 4% false positive rate, fixed carbamidomethyl modification of cysteine residues, and variable modifications, including: oxidation of methionine residues, deamidation of asparagine and glutAmine residues, and acetylation of lysine residues and the N-terminus.

Western Blot Analysis

HFF, A549 and MCF7 Cells incubated in appropriate media were collected and cell lysates were separated with gel electrophoresis on a polyacrylamide gel containing sodium dodecyl sulfate and then transferred to nitrocellulose membranes. The membranes were blocked with Tris-buffered saline (TBS) containing 5% (w/v) skimmed milk. After being washed with TBS containing 0.1% Tween 20 (SigmA), the membranes were incubated overnight at room temperature with MAPK125 antibody (Santa Cruz Biotechnology) diluted with TBS. After being washed, the membranes were incubated for 2 hours at room temperature with the second antibody (Santa Cruz Biotechnology). Bands were detected with an ECL system (Amersham Pharmacia Biotech).

4.8 Results and Discussion

Surface Modifacation Effects on Protein Binding

For the Bare MSNs, 30 proteins were identified from the HFF cells, while 68 proteins from the A549 cells, and 31 proteins were identified from incubation with MCF7 cells. The more negatively charged Phos-MSNs identified 44 proteins from HFF cells, 97 proteins were found from A549 cells, and only 1 protein was identified in the MCF7 cells. A total of 39 proteins were

identified from positively charged Amine-MSN incubated with HFF cells, 49 proteins were determined from A549 cells, and 2 proteins were characterized from MCF7 cells. PEI-MSNs incubated with HFF cells were able to determine 94 proteins, 6 proteins from PEI-MSN incubated with A549 cells, and 3 proteins from PEI-MSN incubated with MCF7 cells. The results are summarized in Table 4.1.

Table 4.1. Overview of the number of proteins identified from coronas of the surface-modified MSNs with various cell lines.

	Bare MSN	Phos-MSN	Amine-MSN	PEI-MSN
HFF	30	44	39	94
A540	68	97	49	6
MCF7	31	1	2	3

A total of 82 unique proteins were identified from positively charged Amine- and PEI-coated MSNs incubated with HFF cells, while 20 unique proteins were identified from negatively charged Bare and Phos-MSN incubated with HFF cells. A total of 34 proteins were identified from both positively and negatively charged MSNs incubated with HFF cells. Several actin, hemoglobin, and histone isoforms were identified bound to all four MSNs types, with no apparent difference in histone identification from positively versus negatively charged particles. Several elongation factors were found bound to three MSNs types (Amine-, Bare-, and Phos-MSNs); and, two POTE ankyrin isoforms (E and F) were found bound to Amine- and Phos-MSNs. A detailed list of the proteins identified can be found in Appendix One.

Mag@MSNs that were incubated with A549 cells were found to have 8 unique proteins were identified from positively charged Amine- and PEI-coated MSNs, 61 unique proteins from negatively charged Bare and Phos-MSN, and 47 proteins were identified from both positively and negatively charged MSNs. Several actin and histone isoforms were identified bound to three MSNs

types (Amine-, Bare-, and Phos- MSNs). Only one protein was identified from PEI-MSN incubated with A549 cells. While actin was equally present on each of the three surface modified particles, histones were much more abundant on the negatively charged nanoparticles. This is likely due to the positively charged characteristics of the histone proteins. Lactate dehydrogenase, pyruvate kinase, and glyceraldehyde-3-phosphate dehydrogenase were detected in digests from both positively and negatively charged particles. Additionally, several elongation factors and POTE ankyrin protein isoforms were detected in all three particle types as well. These POTE isoforms were not the same as those identified from HFF cells. Finally, Mag@MSNs incubated with MCF7 cells had 2 proteins were identified from Amine- and PEI-coated MSNs, 30 proteins from Bare and Phos-MSN, and 3 proteins were identified from both positively and negatively charged MSNs. All data is summarized Figure 4.9.

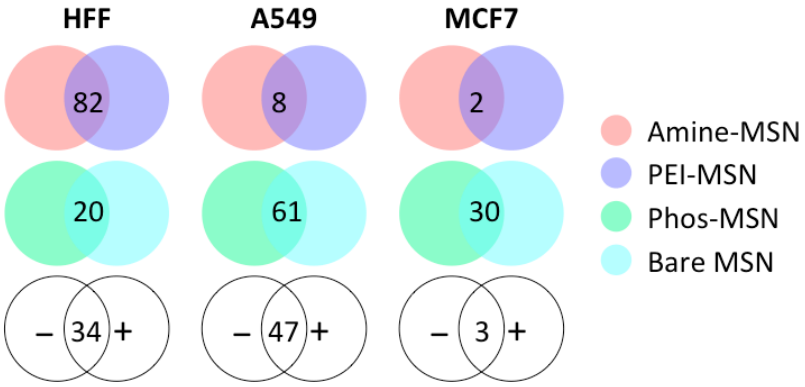

Figure 4.9. Unique proteins, grouped by charge, identified from surface-modified mag@MSNs incubated with HFF, A549, and MCF7 cells.

Protein Localization

A subcellular localization prediction database, WoLF PSORT was used to determine potential locations of identified proteins within the cell. The percentages of proteins identified in each of the subcellular locations (cytoplasm, cytoskeleton, endoplasmic reticulum, mitochondrion, nucleus, secreted, and transmembrane) were calculated. Isoelectric point (pI) was also examined,

however, no significant difference in average protein pI was found between the various particle types or cell types.

Of the positively charged Amine-MSNs and PEI-MSNs incubated with HFF cells, 38% were identified as cytoplasmic proteins, 20% as cytoskeletal proteins, 2% as endoplasmic reticulum-associated proteins, 2% as mitochondrial proteins, 20% as nuclear proteins, and 18% as secretory proteins. No transmembrane proteins were identified from positively charged samples incubated with HFF cells. Negatively charged Bare MSNs and Phos-MSNs behaved differently: 21% were identified as cytoplasmic proteins, 21% as cytoskeletal proteins, 1.9% as mitochondrial proteins, 27% as nuclear proteins, and 23% as secretory proteins. No endoplasmic reticulum-associated proteins or transmembrane proteins were identified.

A549 cells incubated with positively charged MSNs (Amine- and PEI-) had 38% of cytoplasmic proteins, 20% of cytoskeletal proteins, 2% of endoplasmic reticulum-associated proteins, 2% of mitochondrial proteins, 20% of nuclear proteins, 18% of secretory proteins, and no transmembrane proteins were identified. Negatively charged MSNs (Bare and Phos-) identified 46% of cytoplasmic proteins, 12% of cytoskeletal proteins, 2% of mitochondrial 32% of nuclear proteins, 7% of secretory proteins, and 0.7% of transmembrane proteins, while no endoplasmic reticulum-associated proteins were detected.

Finally, surface-modified MSNs incubated with MCF7 cells had the most varying results between the negative and positively charged MSN groups. Positively charged MSNs were able to identify 40% of cytoplasmic proteins, 20% of cytoskeletal proteins, 40% secretory proteins, while the endoplasmic reticulum-associated proteins, mitochondrial proteins, nuclear proteins, and transmembrane proteins were not identified. The negatively charged groups, Bare MSNs and Phos-MSNs, were able to identify 56% of cytoplasmic proteins, 6% of cytoskeletal proteins, mitochondrial proteins, and nuclear proteins each, and 25% of the secretory proteins. Endoplasmic reticulum-

associated proteins and transmembrane proteins were not identified from negatively charged Bare MSNs and Phos-MSN incubated with MCF7 cells.

A549 Cell Line Associated Proteins

A total of 116 proteins were identified from all particles incubated with A549 cells. A total of 12 proteins were identified only in particles incubated with A549 cells. Of these 12 proteins, 3 were found to be disease-associated based on literature searches: organic solute carrier partner protein (OSCP1), POTE ankyrin protein (POTEI and POTEJ), and pyruvate kinase (KPYM).

Though preliminary, OSCP1 has been indicated to be involved in interactions associated with several cancer types.[62] POTEI and POTEJ (POTE2b) have both been found to be expressed in lung cancer, though no mechanism has be implicated.[62] KPYM, a glycolytic enzyme, has been shown to be upregulated in lung tumors.[63] This indicated overactive glycolysis processes, a hallmark of cancerous cells. Though none of these have been indicated as prognostic markers, their differential identification from A549 cells over other cell types indicate their potential.

MCF7 Cell Line Associated Proteins

A total of 34 proteins were identified from all particles incubated with MCF7 cells, while 15 proteins were identified only in particles incubated with MCF7 cells. Of these 15 proteins, 4 were found to be disease-associated based on literature searches: ADP/ATP translocase (ADT2 and ADT3), anterior gradient protein (AGR2), phosphatidylinositol kinase (PI4K2A), and vimentin (VIME).

ADT2 and ADT3 are ADP/ATP translocase enzymes, facilitating ADP/ATP exchange across the inner membrane of the mitochondria. ADT2, or ANT2, has been specifically shown as indicative of levels of cancer aggression, with increased levels associated with enhanced glycolysis.[64] This leads to proliferation, unlike the overexpression of ADT3, which leads to apoptosis.[65,66] ADT2 was found to be upregulated in MCF7 cell lines, and knockdown of this enzyme resulted in cell

death.[67] AGR2 has been previously shown to be associated with breast cancer tumors as well as many other cancers, specifically with lower grade, less aggressive tumors.[68] It was also shown to induce metastasis, and is present in higher concentrations in malignant tumors versus benign tumors.[68] Previous studies have suggested AGR2 as a prognostic marker in breast cancer due to its association with unfavorable patient survival.[69] PI4K2A has previously been shown to be upregulated in many cancer cell lines, including MCF7.[70] Though not conducted in breast cancer patients, a recent study detected upregulation of PIK42A in liver cancer patients and has been suggested as a prognosis marker.[71] VIME has been shown to be associated with breast cancer, as well, and is suggested to be involved in enhancement of invasive capabilities.[72,73]

Mitogen-Activated Protein Kinase

One protein was identified in MSNs incubated with both A549 and MCF7 cells. This protein was mitogen-activated protein kinase 12 (MAPK12), identified from Amine-MSN in A549 cells and Phos-MSN in MCF7 cells. A Western blot analysis confirmed the presence of MAPK12 in both A549 and MCF7 cells, with a higher intensity band in MCF7 cells indicating it is present in higher concentrations, as shown in Figure 4.10. Also of note, MAPK12 was detected by Western blot analysis in HFF cells; however, MAPK12 was not identified from MSNs incubated with HFF cells.

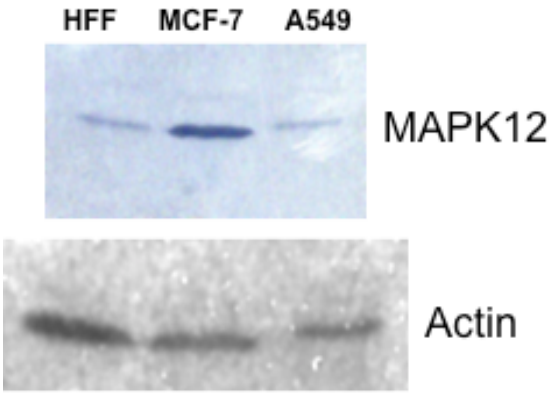

Figure 4.10. A Western Blot of HFF, MCF7, and A549 cell lysates shows that A) MAPK12 is present in all three cell lines, B) Actin control.

MAP kinases in general are involved in complex signaling cascades, involving p38, ERK1, and ERK2.[74] They have largely been associated with cancer processes, and points along the MAPK pathway have been targeted in cancer therapeutic development.[75,76] MAPK12 upregulation has been implicated as an effector in gastric, pancreatic, breast, and bladder cancers, among others; and, other MAP kinases have been suggested to be included as part of prognostic panels in various types of cancers.[77,78] The selective binding of MAPK12 by MSNs incubated with A549 and MCF7 cells suggests further exploration is necessary, as this could be a promising prognostic marker.

Fetal Bovine Serum Protein Identification

Previous studies have suggested nanoparticles can be incubated with one biological sample, transferred to another biological medium, further incubated, and analyzed for protein content that will yield identifications characteristic of both the first and second sample.[14,15] Digested protein coronae from MSNs incubated with HFF cells were found to contain 163 proteins (Amine-MSN), 44 proteins (Bare-MSN), and 66 proteins (PEI-MSN). No FBS-associated proteins were identified from Phos-MSN incubated with HFF cells. Digested protein coronae from MSNs incubated with A549 cells were found to contain 9 proteins (Amine-MSN), 20 proteins (Bare-MSN), 19 proteins (Phos-MSN), and 17 proteins (PEI-MSN). Digested protein coronae from MSNs incubated with MCF7 cells were found to contain 74 proteins (Amine-MSN) and 1 protein (Phos-MSN). No FBS-associated proteins were identified from Bare-MSN or PEI-MSN incubated with MCF7 cells.

4.9 Conclusion

In our second study, MSNs incubated with varied cell types resulted in the identification of several cell line-specific proteins. When compared to MSNs incubated with normal cells (HFF), those MSNs incubated with two diseased cell lines (A549 and MCF7) were found to contain distinct protein coronae. These data suggest that cell lines are distinguishable based on the proteins that

adhere to endocytosed nanoparticles. Previous experiments have shown that when MSNs incubated with two different biological samples sequentially, proteins are retained from both the first and second media. This was observed due to the presence of FBS-associated proteins in protein coronae analyzed from MSNs incubated with various cell lines.

The presence of disease-associated proteins in the protein coronae of MSNs incubated with A549 and MCF7 cell lines suggests that particles are able to bind to a large number of proteins, not just those that are most abundant. Furthermore, these data indicate MSNs as promising tools for prognostic and diagnostic tests. Biocompatibility and fast clearance from the body have been shown in animal models when utilizing MSNs as drug delivery vehicles, thus MSNs utility as diagnostic tools should be further explored.

4.10 References

(1) Slowing, I. I.; Vivero-Escoto, J. L.; Wu, C.-W.; Lin, V. S.-Y. *Adv. Drug Deliv. Rev.* **2008**, *60*, 1278–1288.

(2) Vallet-Regí, M.; Balas, F.; Arcos, D. *Angew. Chem. Int. Ed. Engl.* **2007**, *46*, 7548–7558.

(3) Kresge, C. T.; Leonowicz, M. E.; Roth, W. J.; Vartuli, J. C.; Beck, J. S. *Nature* **1992**, *359*, 710–712.

(4) Huh, S.; Wiench, J. W.; Yoo, J.-C.; Pruski, M.; Lin, V. S.-Y. *Chem. Mater.* **2003**, *15*, 4247–4256.

(5) Lu, J.; Liong, M.; Zink, J. I.; Tamanoi, F. *Small* **2007**, *3*, 1341–1346.

(6) Lu, J.; Choi, E.; Tamanoi, F.; Zink, J. I. *Small* **2008**, *4*, 421–426.

(7) Meng, H.; Liong, M.; Xia, T.; Li, Z.; Ji, Z.; Zink, J. I.; Nel, A. E. *ACS Nano* **2010**, *4*, 4539–4550.

(8) Thomas, C. R.; Ferris, D. P.; Lee, J.-H.; Choi, E.; Cho, M. H.; Kim, E. S.; Stoddart, J. F.; Shin, J.-S.; Cheon, J.; Zink, J. I. *J. Am. Chem. Soc.* **2010**, *132*, 10623–10625.

(9) Zhu, C.-L.; Lu, C.-H.; Song, X.-Y.; Yang, H.-H.; Wang, X.-R. *J. Am. Chem. Soc.* **2011**, *133*, 1278–1281.

(10) Liong, M.; Lu, J.; Kovochich, M.; Xia, T.; Ruehm, S. G.; Nel, A. E.; Tamanoi, F.; Zink, J. I. *ACS Nano* **2008**, *2*, 889–896.

(11) Mortera, R.; Vivero-Escoto, J.; Slowing, I. I.; Garrone, E.; Onida, B.; Lin, V. S.-Y. *Chem. Commun. (Camb).* **2009**, 3219–3221.

(12) Trewyn, B. G.; Slowing, I. I.; Giri, S.; Chen, H.-T.; Lin, V. S.-Y. *Acc. Chem. Res.* **2007**, *40*, 846–853.

(13) Bottini, M.; Cerignoli, F.; Mills, D. M.; D'Annibale, F.; Leone, M.; Rosato, N.; Magrini, A.; Pellecchia, M.; Bergamaschi, A.; Mustelin, T. *J. Am. Chem. Soc.* **2007**, *129*, 7814–7823.

(14) Lu, J.; Liong, M.; Sherman, S.; Xia, T.; Kovochich, M.; Nel, A. E.; Zink, J. I.; Tamanoi, F. *Nanobiotechnology* **2007**, *3*, 89–95.

(15) Lee, C.-H.; Cheng, S.-H.; Huang, I.-P.; Souris, J. S.; Yang, C.-S.; Mou, C.-Y.; Lo, L.-W. *Angew. Chemie* **2010**, *122*, 8390–8395.

(16) He, Q.; Zhang, Z.; Gao, F.; Li, Y.; Shi, J. *Small* **2011**, *7*, 271–280.

(17) Meng, H.; Xue, M.; Xia, T.; Ji, Z.; Tarn, D. Y.; Zink, J. I.; Nel, A. E. *ACS Nano* **2011**, *5*, 4131–4144.

(18) Sauer, A. M.; Schlossbauer, A.; Ruthardt, N.; Cauda, V.; Bein, T.; Bräuchle, C. *Nano Lett.* **2010**, *10*, 3684–3691.

(19) Lu, J.; Li, Z.; Zink, J. I.; Tamanoi, F. *Nanomedicine* **2012**, *8*, 212–220.

(20) Lu, J.; Liong, M.; Li, Z.; Zink, J. I.; Tamanoi, F. *Small* **2010**, *6*, 1794–1805.

(21) Mamaeva, V.; Rosenholm, J. M.; Bate-Eya, L. T.; Bergman, L.; Peuhu, E.; Duchanoy, A.; Fortelius, L. E.; Landor, S.; Toivola, D. M.; Lindén, M.; Sahlgren, C. *Mol. Ther.* **2011**, *19*, 1538–1546.

(22) Slowing, I. I.; Trewyn, B. G.; Lin, V. S.-Y. *J. Am. Chem. Soc.* **2007**, *129*, 8845–8849.

(23) Qin, F.; Zhou, Y.; Shi, J.; Zhang, Y. *J. Biomed. Mater. Res. A* **2009**, *90*, 333–338.

(24) Kim, J.; Kim, H.; Lee, N.; Kim, T. *Angew. Chemie …* **2008**.

(25) Ferris, D. P.; Lu, J.; Gothard, C.; Yanes, R.; Thomas, C. R.; Olsen, J.-C.; Stoddart, J. F.; Tamanoi, F.; Zink, J. I. *Small* **2011**, *7*, 1816–1826.

(26) Gan, Q.; Dai, D.; Yuan, Y.; Qian, J.; Sha, S.; Shi, J.; Liu, C. *Biomed. Microdevices* **2012**, *14*, 259–270.

(27) Huang, X.; Teng, X.; Chen, D.; Tang, F.; He, J. *Biomaterials* **2010**, *31*, 438–448.

(28) Slowing, I. I.; Vivero-Escoto, J. L.; Zhao, Y.; Kandel, K.; Peeraphatdit, C.; Trewyn, B. G.; Lin, V. S.-Y. *Small* **2011**, *7*, 1526–1532.

(29) Slowing, I.; Trewyn, B. G.; Lin, V. S.-Y. *J. Am. Chem. Soc.* **2006**, *128*, 14792–14793.

(30) Liu, H.-M.; Wu, S.-H.; Lu, C.-W.; Yao, M.; Hsiao, J.-K.; Hung, Y.; Lin, Y.-S.; Mou, C.-Y.; Yang, C.-S.; Huang, D.-M.; Chen, Y.-C. *Small* **2008**, *4*, 619–626.

(31) Bagwe, R. P.; Hilliard, L. R.; Tan, W. *Langmuir* **2006**, *22*, 4357–4362.

(32) Meng, H.; Xue, M.; Xia, T.; Zhao, Y.-L.; Tamanoi, F.; Stoddart, J. F.; Zink, J. I.; Nel, A. E. *J. Am. Chem. Soc.* **2010**, *132*, 12690–12697.

(33) Gerasimenko, J.; Gerasimenko, O.; Petersen, O. *Curr. Biol.* **2001**, 971–974.

(34) Castino, R.; Démoz, M.; Isidoro, C. *J. Mol. …* **2003**, 337–348.

(35) Rodríguez, A.; Webster, P. *J. cell …* **1997**, *137*, 93–104.

(36) Feng, Y.; Yu, S.; Lasell, T. K. R.; Jadhav, A. P.; Macia, E.; Chardin, P.; Melancon, P.; Roth, M.; Mitchison, T.; Kirchhausen, T. *Proc. Natl. Acad. Sci. U. S. A.* **2003**, *100*, 6469–6474.

(37) Peyroche, A.; Antonny, B.; Robineau, S.; Acker, J. *Mol. Cell* **1999**, *3*, 275–285.

(38) Dascher, C.; Balch, W. *J. Biol. Chem.* **1994**, 1437–1448.

(39) Strous, G.; Kerkhof, P. Van. *J. Biol.* … **1993**, *268*, 2341–2347.

(40) Huang, D.-M.; Hung, Y.; Ko, B.-S.; Hsu, S.-C.; Chen, W.-H.; Chien, C.-L.; Tsai, C.-P.; Kuo, C.-T.; Kang, J.-C.; Yang, C.-S.; Mou, C.-Y.; Chen, Y.-C. *FASEB J.* **2005**, *19*, 2014–2016.

(41) Cordonnier, M.; Dauzonne, D. *Mol. Biol.* … **2001**, *12*, 4013–4029.

(42) Ono, K.; Wang, X.; Han, J. *Mol. Cell. Biol.* **2001**, *21*, 8276–8288.

(43) Rodríguez, A.; Martinez, I.; Chung, A. *J. Biol.* … **1999**, *274*, 16754–16759.

(44) Carini, R.; Castino, R.; De Cesaris, M. G.; Splendore, R.; Démoz, M.; Albano, E.; Isidoro, C. *J. Cell Sci.* **2004**, *117*, 1065–1077.

(45) Martinez, I.; Chakrabarti, S. *J. cell* … **2000**, *148*, 1141–1149.

(46) Flannery, A. R.; Czibener, C.; Andrews, N. W. *J. Cell Biol.* **2010**, *191*, 599–613.

(47) Lange, Y.; Ye, J.; Steck, T. L. *J. Biol. Chem.* **1998**, *273*, 18915–18922.

(48) Sparrow, S.; Carter, J.; Ridgway, N. *Neurochem.* … **1999**, *24*, 69–77.

(49) Lloyd-Evans, E.; Morgan, A. J.; He, X.; Smith, D. a; Elliot-Smith, E.; Sillence, D. J.; Churchill, G. C.; Schuchman, E. H.; Galione, A.; Platt, F. M. *Nat. Med.* **2008**, *14*, 1247–1255.

(50) Nel, A. E.; Mädler, L.; Velegol, D.; Xia, T.; Hoek, E. M. V; Somasundaran, P.; Klaessig, F.; Castranova, V.; Thompson, M. *Nat. Mater.* **2009**, *8*, 543–557.

(51) Lundqvist, M.; Stigler, J.; Elia, G.; Lynch, I.; Cedervall, T.; Dawson, K. a. *Proc. Natl. Acad. Sci. U. S. A.* **2008**, *105*, 14265–14270.

(52) Casals, E.; Pfaller, T.; Duschl, A.; Oostingh, G. J.; Puntes, V. F. *Small* **2011**, *7*, 3479–3486.

(53) Lundqvist, M.; Stigler, J.; Cedervall, T. *ACS* … **2011**, 7503–7509.

(54) Aggarwal, P.; Hall, J. B.; McLeland, C. B.; Dobrovolskaia, M. a; McNeil, S. E. *Adv. Drug Deliv. Rev.* **2009**, *61*, 428–437.

(55) Owens, D. E.; Peppas, N. a. *Int. J. Pharm.* **2006**, *307*, 93–102.

(56) Göppert, T. M.; Müller, R. H. *J. Drug Target.* **2005**, *13*, 179–187.

(57) Kreuter, J. *Adv. Drug Deliv. Rev.* **2001**, *47*, 65–81.

(58) Olivier, J. *NeuroRx* **2005**, *2*, 108–119.

(59) Gref, R.; Lück, M.; Quellec, P. *Colloids Surfaces B …* **2000**, *18*, 301–313.

(60) Xia, T.; Kovochich, M.; Liong, M.; Meng, H.; Kabehie, S.; George, S.; Zink, J. I.; Nel, A. E. *ACS Nano* **2009**, *3*, 3273–3286.

(61) Yanes, R. E.; Tarn, D.; Hwang, A. a; Ferris, D. P.; Sherman, S. P.; Thomas, C. R.; Lu, J.; Pyle, A. D.; Zink, J. I.; Tamanoi, F. *Small* **2013**, *9*, 697–704.

(62) Nikas, J. B.; Low, W. C. *Cancer Inform.* **2012**, *11*, 1–14.

(63) Bera, T. K.; Saint Fleur, A.; Lee, Y.; Kydd, A.; Hahn, Y.; Popescu, N. C.; Zimonjic, D. B.; Lee, B.; Pastan, I. *Cancer Res.* **2006**, *66*, 52–56.

(64) Chevrollier, A.; Loiseau, D.; Chabi, B.; Renier, G.; Douay, O.; Malthièry, Y.; Stepien, G. *J. Bioenerg. Biomembr.* **2005**, *37*, 307–316.

(65) Le Bras, M.; Borgne-Sanchez, A.; Touat, Z.; El Dein, O. S.; Deniaud, A.; Maillier, E.; Lecellier, G.; Rebouillat, D.; Lemaire, C.; Kroemer, G.; Jacotot, E.; Brenner, C. *Cancer Res.* **2006**, *66*, 9143–9152.

(66) Yang, Z.; Cheng, W.; Hong, L. *Mol. Biol. …* **2007**, *18*, 4681–4689.

(67) Jang, J.-Y.; Choi, Y.; Jeon, Y.-K.; Kim, C.-W. *Breast Cancer Res.* **2008**, *10*, R11.

(68) Fritzsche, F. R.; Dahl, E.; Pahl, S.; Burkhardt, M.; Luo, J.; Mayordomo, E.; Gansukh, T.; Dankof, A.; Knuechel, R.; Denkert, C.; Winzer, K.-J.; Dietel, M.; Kristiansen, G. *Clin. Cancer Res.* **2006**, *12*, 1728–1734.

(69) Barraclough, D. L.; Platt-Higgins, A.; de Silva Rudland, S.; Barraclough, R.; Winstanley, J.; West, C. R.; Rudland, P. S. *Am. J. Pathol.* **2009**, *175*, 1848–1857.

(70) Li, J.; Lu, Y.; Zhang, J.; Kang, H.; Qin, Z.; Chen, C. *Oncogene* **2010**, *29*, 2550–2559.

(71) Ilboudo, A.; Nault, J.-C.; Dubois-Pot-Schneider, H.; Corlu, A.; Zucman-Rossi, J.; Samson, M.; Le Seyec, J. *BMC Cancer* **2014**, *14*, 7.

(72) Fu, C.-H.; Lin, R.-J.; Yu, J.; Chang, W.-W.; Liao, G.-S.; Chang, W.-Y.; Tseng, L.-M.; Tsai, Y.-F.; Yu, J.-C.; Yu, A. L. *Stem Cells* **2014**, *32*, 2048–2060.

(73) Sommers, C.; Heckford, S.; Skerker, J. *Cancer Res.* **1992**, 5190–5197.

(74) Wagner, E. F.; Nebreda, A. R. *Nat. Rev. Cancer* **2009**, *9*, 537–549.

(75) Lord, C. J.; Ashworth, A. *Curr. Opin. Pharmacol.* **2008**, *8*, 363–369.

(76) Sebolt-Leopold, J. S.; Herrera, R. *Nat. Rev. Cancer* **2004**, *4*, 937–947.

(77) Tao, K.; Fang, M.; Alroy, J.; Sahagian, G. G. *BMC Cancer* **2008**, *8*, 228.

(78) Mitra, A. P.; Pagliarulo, V.; Yang, D.; Waldman, F. M.; Datar, R. H.; Skinner, D. G.; Groshen, S.; Cote, R. J. *J. Clin. Oncol.* **2009**, *27*, 3929–3937.

APPENDIX ONE

Tables of Proteins Identified in Protein Corona

by Mass Spectrometry Analysis

Table 4.2. Proteins identified from MSNs incubated with HFF cells.

Particle Type	Protein ID	Protein Name	Subcellular Localization
Amine-MSN	ACTA	Actin_ aortic smooth muscle	Cytoplasm
Amine-MSN	ACTB	Actin_ cytoplasmic 1	Cytoplasm
Amine-MSN	ACTBL	Beta-actin-like protein 2	Cytoplasm
Amine-MSN	ACTBM	Putative beta-actin-like protein 3	Cytoplasm
Amine-MSN	ACTC	Actin_ alpha cardiac muscle 1	Cytoplasm
Amine-MSN	ACTG	Actin_ cytoplasmic 2	Cytoplasm
Amine-MSN	ACTH	Actin_ gamma-enteric smooth muscle	Cytoplasm
Amine-MSN	ACTS	Actin_ alpha skeletal muscle	Cytoplasm
Amine-MSN	ATPA	ATP synthase subunit alpha_ mitochondrial	Cytoskeleton
Amine-MSN	CEP89	Centrosomal protein of 89 kDa	Cytoskeleton
Amine-MSN	DESM	Desmin	Cytoskeleton
Amine-MSN	EF1A1	Elongation factor 1-alpha 1	Cytoskeleton
Amine-MSN	EF1A2	Elongation factor 1-alpha 2	Cytoskeleton
Amine-MSN	EF1A3	Putative elongation factor 1-alpha-like 3	Cytoskeleton
Amine-MSN	ENPL	Endoplasmin	Cytoskeleton
Amine-MSN	H4	Histone H4	Nucleus
Amine-MSN	HBA	Hemoglobin subunit alpha	Nucleus
Amine-MSN	HS71L	Heat shock 70 kDa protein 1-like	Cytoplasm
Amine-MSN	HS90A	Heat shock protein HSP 90-alpha	Cytoplasm
Amine-MSN	HS90B	Heat shock protein HSP 90-beta	Cytoplasm
Amine-MSN	HSP71	Heat shock 70 kDa protein 1A/1B	Cytoplasm
Amine-MSN	HSP72	Heat shock-related 70 kDa protein 2	Cytoplasm
Amine-MSN	HSP76	Heat shock 70 kDa protein 6	Cytoplasm
Amine-MSN	HSP77	Putative heat shock 70 kDa protein 7	Cytoplasm
Amine-MSN	HSP7C	Heat shock cognate 71 kDa protein	Cytoplasm
Amine-MSN	NUCL	Nucleolin	Secretory
Amine-MSN	POTEE	POTE ankyrin domain family member E	Secretory
Amine-MSN	POTEF	POTE ankyrin domain family member F	Secretory
Amine-MSN	RL40	Ubiquitin-60S ribosomal protein L40	Secretory
Amine-MSN	RS27A	Ubiquitin-40S ribosomal protein S27a	Secretory
Amine-MSN	TBA1A	Tubulin alpha-1A chain	Secretory
Amine-MSN	TBA1B	Tubulin alpha-1B chain	Secretory
Amine-MSN	TBA1C	Tubulin alpha-1C chain	Secretory
Amine-MSN	TBA3C	Isoform 2 of Tubulin alpha-3C/D chain	Secretory
Amine-MSN	TBA3E	Tubulin alpha-3E chain	Secretory
Amine-MSN	TBB5	Tubulin beta chain	Secretory
Amine-MSN	UBB	Polyubiquitin-B	Secretory
Amine-MSN	UBC	Polyubiquitin-C	Secretory
Amine-MSN	VTNC	Vitronectin	Secretory
Bare-MSN	ACTA	Actin_ aortic smooth muscle	Cytoplasm
Bare-MSN	ACTB	Actin_ cytoplasmic 1	Cytoplasm
Bare-MSN	ACTBL	Beta-actin-like protein 2	Cytoplasm
Bare-MSN	ACTBM	Putative beta-actin-like protein 3	Cytoplasm
Bare-MSN	ACTC	Actin_ alpha cardiac muscle 1	Cytoplasm
Bare-MSN	ACTG	Actin_ cytoplasmic 2	Cytoplasm
Bare-MSN	ACTH	Actin_ gamma-enteric smooth muscle	Cytoplasm
Bare-MSN	ACTS	Actin_ alpha skeletal muscle	Cytoplasm
Bare-MSN	AL3A2	Isoform 2 of Fatty aldehyde dehydrogenase	Cytoskeleton
Bare-MSN	APOA1	Apolipoprotein A-I	Cytoskeleton
Bare-MSN	APOE	Apolipoprotein E	Cytoskeleton
Bare-MSN	EF1A1	Elongation factor 1-alpha 1	Cytoskeleton
Bare-MSN	EF1A2	Elongation factor 1-alpha 2	Cytoskeleton
Bare-MSN	EF1A3	Putative elongation factor 1-alpha-like 3	Cytoskeleton
Bare-MSN	GELS	Gelsolin	Cytoskeleton

Bare-MSN	H4	Histone H4	Nucleus
Bare-MSN	HBA	Hemoglobin subunit alpha	Nucleus
Bare-MSN	HBAZ	Hemoglobin subunit zeta	Nucleus
Bare-MSN	HBB	Hemoglobin subunit beta	Nucleus
Bare-MSN	HBD	Hemoglobin subunit delta	Nucleus
Bare-MSN	HBE	Hemoglobin subunit epsilon	Nucleus
Bare-MSN	HBG1	Hemoglobin subunit gamma-1	Cytoplasm
Bare-MSN	HBG2	Hemoglobin subunit gamma-2	Cytoplasm
Bare-MSN	IBP2	Insulin-like growth factor-binding protein 2	Secretory
Bare-MSN	POTEE	POTE ankyrin domain family member E	Secretory
Bare-MSN	POTEF	POTE ankyrin domain family member F	Secretory
Bare-MSN	QCR7	Cytochrome b-c1 complex subunit 7	Mitochondria
Bare-MSN	SNAI3	Zinc finger protein SNAI3	Secretory
Bare-MSN	VTNC	Vitronectin	Secretory
Bare-MSN	WIPF3	WAS/WASL-interacting protein family member 3	Secretory
PEI-MSN	ACTA	Actin_ aortic smooth muscle	Cytoplasm
PEI-MSN	ACTB	Actin_ cytoplasmic 1	Cytoplasm
PEI-MSN	ACTBL	Beta-actin-like protein 2	Cytoplasm
PEI-MSN	ACTBM	Putative beta-actin-like protein 3	Cytoplasm
PEI-MSN	ACTC	Actin_ alpha cardiac muscle 1	Cytoplasm
PEI-MSN	ACTG	Actin_ cytoplasmic 2	Cytoplasm
PEI-MSN	ACTH	Actin_ gamma-enteric smooth muscle	Cytoplasm
PEI-MSN	ACTS	Actin_ alpha skeletal muscle	Cytoplasm
PEI-MSN	ALBU	Serum albumin	Cytoskeleton
PEI-MSN	ANR35	Ankyrin repeat domain-containing protein 35	Cytoskeleton
PEI-MSN	APOA1	Apolipoprotein A-I	Cytoskeleton
PEI-MSN	APOE	Apolipoprotein E	Cytoskeleton
PEI-MSN	GOG8I	Golgin subfamily A member 8I	Cytoskeleton
PEI-MSN	H2A1	Histone H2A type 1	Cytoskeleton
PEI-MSN	H2A1A	Histone H2A type 1-A	Cytoskeleton
PEI-MSN	H2A1B	Histone H2A type 1-B/E	Cytoskeleton
PEI-MSN	H2A1C	Histone H2A type 1-C	Nucleus
PEI-MSN	H2A1D	Histone H2A type 1-D	Nucleus
PEI-MSN	H2A1H	Histone H2A type 1-H	Nucleus
PEI-MSN	H2A1J	Histone H2A type 1-J	Nucleus
PEI-MSN	H2A2A	Histone H2A type 2-A	Nucleus
PEI-MSN	H2A2B	Histone H2A type 2-B	Nucleus
PEI-MSN	H2A2C	Histone H2A type 2-C	Nucleus
PEI-MSN	H2A3	Histone H2A type 3	Nucleus
PEI-MSN	H2AJ	Histone H2A.J	Nucleus
PEI-MSN	H2AV	Isoform 2 of Histone H2A.V	Nucleus
PEI-MSN	H2AX	Histone H2A.x	Nucleus
PEI-MSN	H2AZ	Histone H2A.Z	Nucleus
PEI-MSN	H2B1A	Histone H2B type 1-A	Nucleus
PEI-MSN	H2B1B	Histone H2B type 1-B	Nucleus
PEI-MSN	H2B1C	Histone H2B type 1-C/E/F/G/I	Nucleus
PEI-MSN	H2B1D	Histone H2B type 1-D	Nucleus
PEI-MSN	H2B1H	Histone H2B type 1-H	Nucleus
PEI-MSN	H2B1J	Histone H2B type 1-J	Nucleus
PEI-MSN	H2B1K	Histone H2B type 1-K	Nucleus
PEI-MSN	H2B1L	Histone H2B type 1-L	Nucleus
PEI-MSN	H2B1M	Histone H2B type 1-M	Nucleus
PEI-MSN	H2B1N	Histone H2B type 1-N	Nucleus
PEI-MSN	H2B1O	Histone H2B type 1-O	Nucleus
PEI-MSN	H2B2E	Histone H2B type 2-E	Nucleus
PEI-MSN	H2B2F	Histone H2B type 2-F	Nucleus
PEI-MSN	H2B3B	Histone H2B type 3-B	Nucleus
PEI-MSN	H2BFS	Histone H2B type F-S	Nucleus

PEI-MSN	H31	Histone H3.1	Nucleus
PEI-MSN	H31T	Histone H3.1t	Nucleus
PEI-MSN	H32	Histone H3.2	Nucleus
PEI-MSN	H33	Histone H3.3	Nucleus
PEI-MSN	H4	Histone H4	Nucleus
PEI-MSN	HBA	Hemoglobin subunit alpha	Nucleus
PEI-MSN	HBB	Hemoglobin subunit beta	Nucleus
PEI-MSN	HBD	Hemoglobin subunit delta	Nucleus
PEI-MSN	HBE	Hemoglobin subunit epsilon	Nucleus
PEI-MSN	HBG1	Hemoglobin subunit gamma-1	Cytoplasm
PEI-MSN	HBG2	Hemoglobin subunit gamma-2	Cytoplasm
PEI-MSN	ITIH2	Inter-alpha-trypsin inhibitor heavy chain H2	Secretory
PEI-MSN	KCD18	BTB/POZ domain-containing protein KCTD18	Secretory
PEI-MSN	MBB1A	Myb-binding protein 1A	Secretory
PEI-MSN	NPM	Nucleophosmin	Secretory
PEI-MSN	NUSAP	Nucleolar and spindle-associated protein 1	Secretory
PEI-MSN	PGS1	Biglycan	Secretory
PEI-MSN	POTEE	POTE ankyrin domain family member E	Secretory
PEI-MSN	POTEF	POTE ankyrin domain family member F	Secretory
PEI-MSN	PRRX2	Paired mesoderm homeobox protein 2	Secretory
PEI-MSN	RED	Protein Red	Secretory
PEI-MSN	RL40	Ubiquitin-60S ribosomal protein L40	Secretory
PEI-MSN	RLA1	60S acidic ribosomal protein P1	Secretory
PEI-MSN	RLA2	60S acidic ribosomal protein P2	Secretory
PEI-MSN	RN214	RING finger protein 214	Secretory
PEI-MSN	RS27A	Ubiquitin-40S ribosomal protein S27a	Secretory
PEI-MSN	TBA1A	Tubulin alpha-1A chain	Secretory
PEI-MSN	TBA1B	Tubulin alpha-1B chain	Secretory
PEI-MSN	TBA1C	Tubulin alpha-1C chain	Secretory
PEI-MSN	TBA4A	Tubulin alpha-4A chain	Secretory
PEI-MSN	THRB	Prothrombin	Secretory
PEI-MSN	UBB	Polyubiquitin-B	Secretory
PEI-MSN	UBC	Polyubiquitin-C	Secretory
PEI-MSN	VTNC	Vitronectin	Secretory
PEI-MSN	VWA3A	von Willebrand factor A domain-containing protein 3A	Secretory
PEI-MSN	ZBT25	Zinc finger and BTB domain-containing protein 25	Secretory
PEI-MSN	ZC3HD	Isoform 2 of Zinc finger CCCH domain-containing protein 13	Secretory
Phos-MSN	ACTA	Actin_ aortic smooth muscle	Cytoplasm
Phos-MSN	ACTB	Actin_ cytoplasmic 1	Cytoplasm
Phos-MSN	ACTC	Actin_ alpha cardiac muscle 1	Cytoplasm
Phos-MSN	ACTG	Actin_ cytoplasmic 2	Cytoplasm
Phos-MSN	ACTH	Actin_ alpha cardiac muscle 1	Cytoplasm
Phos-MSN	ACTS	Actin_ cytoplasmic 2	Cytoplasm
Phos-MSN	AL3A2	Actin_ gamma-enteric smooth muscle	Cytoskeleton
Phos-MSN	APOE	Actin_ alpha skeletal muscle	Cytoskeleton
Phos-MSN	CCD50	Coiled-coil domain-containing protein 50	Cytoskeleton
Phos-MSN	CLIC2	Chloride intracellular channel protein 2	Cytoskeleton
Phos-MSN	EF1A1	Elongation factor 1-alpha 1	Cytoskeleton
Phos-MSN	EF1A2	Elongation factor 1-alpha 2	Cytoskeleton
Phos-MSN	EF1A3	Putative elongation factor 1-alpha-like 3	Cytoskeleton
Phos-MSN	GELS	Gelsolin	Cytoskeleton
Phos-MSN	H2A1	Histone H2A type 1	Cytoskeleton
Phos-MSN	H2A1B	Histone H2A type 1-B/E	Cytoskeleton
Phos-MSN	H2A1C	Histone H2A type 1-C	Nucleus
Phos-MSN	H2A1D	Histone H2A type 1-D	Nucleus
Phos-MSN	H2A1H	Histone H2A type 1-H	Nucleus
Phos-MSN	H2A1J	Histone H2A type 1-J	Nucleus
Phos-MSN	H2A2A	Histone H2A type 2-A	Nucleus

Phos-MSN	H2A2C	Histone H2A type 2-C	Nucleus
Phos-MSN	H2A3	Histone H2A type 3	Nucleus
Phos-MSN	H2AJ	Histone H2A.J	Nucleus
Phos-MSN	H33	Histone H3.3	Nucleus
Phos-MSN	HBA	Hemoglobin subunit alpha	Nucleus
Phos-MSN	HBB	Hemoglobin subunit beta	Nucleus
Phos-MSN	HBD	Hemoglobin subunit delta	Nucleus
Phos-MSN	HBE	Hemoglobin subunit epsilon	Nucleus
Phos-MSN	HBG1	Hemoglobin subunit gamma-1	Cytoplasm
Phos-MSN	HBG2	Hemoglobin subunit gamma-2	Cytoplasm
Phos-MSN	HRG	Histidine-rich glycoprotein	Cytoplasm
Phos-MSN	IBP2	Insulin-like growth factor-binding protein 2	Secretory
Phos-MSN	PDE9A	High affinity cGMP-specific 3'_5'-cyclic phosphodiesterase 9A	Secretory
Phos-MSN	POTEE	POTE ankyrin domain family member E	Secretory
Phos-MSN	POTEF	POTE ankyrin domain family member F	Secretory
Phos-MSN	SEMG1	Semenogelin-1	Secretory
Phos-MSN	SSH1	Protein phosphatase Slingshot homolog 1	Secretory
Phos-MSN	VTNC	Vitronectin	Secretory
Phos-MSN	ZNHI2	Zinc finger HIT domain-containing protein 2	Secretory

Table 4.3. Human proteins identified from MSNs incubated with A549 cells.

Particle Type	Protein ID	Protein Name	Subcellular Localization
Amine-MSN	ACTA	Actin_ aortic smooth muscle	Cytoplasm
Amine-MSN	ACTB	Actin_ cytoplasmic 1	Cytoplasm
Amine-MSN	ACTBL	Beta-actin-like protein 2	Cytoplasm
Amine-MSN	ACTC	Actin_ alpha cardiac muscle 1	Cytoplasm
Amine-MSN	ACTG	Actin_ cytoplasmic 2	Cytoplasm
Amine-MSN	ACTH	Actin_ gamma-enteric smooth muscle	Cytoplasm
Amine-MSN	ACTS	Actin_ alpha skeletal muscle	Cytoplasm
Amine-MSN	AL1A1	Retinal dehydrogenase 1	Cytoplasm
Amine-MSN	ALDH2	Aldehyde dehydrogenase_ mitochondrial	Mitochondria
Amine-MSN	ANXA1	Annexin A1	Nucleus
Amine-MSN	EF1A1	Elongation factor 1-alpha 1	Cytoskeleton
Amine-MSN	EF1A2	Elongation factor 1-alpha 2	Cytoskeleton
Amine-MSN	EF1A3	Putative elongation factor 1-alpha-like 3	Cytoskeleton
Amine-MSN	ENOA	Alpha-enolase	Cytoplasm
Amine-MSN	ENOA	Alpha-enolase	Cytoplasm
Amine-MSN	G3P	Glyceraldehyde-3-phosphate dehydrogenase	Cytoplasm
Amine-MSN	H12	Histone H1.2	Nucleus
Amine-MSN	H13	Histone H1.3	Nucleus
Amine-MSN	H14	Histone H1.4	Nucleus
Amine-MSN	KPYM	Pyruvate kinase isozymes M1/M2	Cytoplasm
Amine-MSN	LDHA	L-lactate dehydrogenase A chain	Mitochondria
Amine-MSN	MK12	Mitogen-activated protein kinase 12	Cytoplasm
Amine-MSN	OSCP1	Protein OSCP1	Transmembrane
Amine-MSN	POTEE	POTE ankyrin domain family member E	Secretory
Amine-MSN	POTEF	POTE ankyrin domain family member F	Secretory
Amine-MSN	POTEI	POTE ankyrin domain family member I	Secretory
Amine-MSN	POTEJ	POTE ankyrin domain family member J	Secretory
Amine-MSN	PROF1	Profilin-1	Cytoplasm
Amine-MSN	TBA1A	Tubulin alpha-1A chain	Secretory
Amine-MSN	TBA1B	Tubulin alpha-1B chain	Secretory
Amine-MSN	TBA1C	Tubulin alpha-1C chain	Secretory
Bare-MSN	ACTA	Actin_ aortic smooth muscle	Cytoplasm
Bare-MSN	ACTB	Actin_ cytoplasmic 1	Cytoplasm
Bare-MSN	ACTBL	Beta-actin-like protein 2	Cytoplasm
Bare-MSN	ACTBM	Putative beta-actin-like protein 3	Cytoplasm
Bare-MSN	ACTC	Actin_ alpha cardiac muscle 1	Cytoplasm
Bare-MSN	ACTG	Actin_ cytoplasmic 2	Cytoplasm
Bare-MSN	ACTH	Actin_ gamma-enteric smooth muscle	Cytoplasm
Bare-MSN	ACTS	Actin_ alpha skeletal muscle	Cytoplasm
Bare-MSN	AK1BA	Aldo-keto reductase family 1 member B10	Cytoplasm
Bare-MSN	AL1A1	Retinal dehydrogenase 1	Cytoplasm
Bare-MSN	ALDH2	Aldehyde dehydrogenase_ mitochondrial	Mitochondria
Bare-MSN	ANXA1	Annexin A1	Nucleus
Bare-MSN	ANXA2	Annexin A2	Nucleus
Bare-MSN	AXA2L	Putative annexin A2-like protein	Nucleus
Bare-MSN	EF1A1	Elongation factor 1-alpha 1	Cytoskeleton
Bare-MSN	EF1A2	Elongation factor 1-alpha 2	Cytoskeleton
Bare-MSN	EF1A3	Putative elongation factor 1-alpha-like 3	Cytoskeleton
Bare-MSN	ENOA	Alpha-enolase	Cytoplasm
Bare-MSN	G3P	Glyceraldehyde-3-phosphate dehydrogenase	Cytoplasm
Bare-MSN	H2B1A	Histone H2B type 1-A	Nucleus
Bare-MSN	H2B1B	Histone H2B type 1-B	Nucleus
Bare-MSN	H2B1C	Histone H2B type 1-C/E/F/G/I	Nucleus
Bare-MSN	H2B1D	Histone H2B type 1-D	Nucleus

Bare-MSN	H2B1H	Histone H2B type 1-H	Nucleus
Bare-MSN	H2B1J	Histone H2B type 1-J	Nucleus
Bare-MSN	H2B1K	Histone H2B type 1-K	Nucleus
Bare-MSN	H2B1L	Histone H2B type 1-L	Nucleus
Bare-MSN	H2B1M	Histone H2B type 1-M	Nucleus
Bare-MSN	H2B1N	Histone H2B type 1-N	Nucleus
Bare-MSN	H2B1O	Histone H2B type 1-O	Nucleus
Bare-MSN	H2B2E	Histone H2B type 2-E	Nucleus
Bare-MSN	H2B2F	Histone H2B type 2-F	Nucleus
Bare-MSN	H2BFS	Histone H2B type F-S	Nucleus
Bare-MSN	H4	Histone H4	Nucleus
Bare-MSN	H90B3	Putative heat shock protein HSP 90-beta-3	Cytoplasm
Bare-MSN	HS71L	Heat shock 70 kDa protein 1-like	Cytoplasm
Bare-MSN	HS90A	Heat shock protein HSP 90-alpha	Cytoplasm
Bare-MSN	HS90B	Heat shock protein HSP 90-beta	Cytoplasm
Bare-MSN	HSP71	Heat shock 70 kDa protein 1A/1B	Cytoplasm
Bare-MSN	HSP72	Heat shock-related 70 kDa protein 2	Cytoplasm
Bare-MSN	HSP7C	Heat shock cognate 71 kDa protein	Cytoplasm
Bare-MSN	KPYM	Pyruvate kinase isozymes M1/M2	Cytoplasm
Bare-MSN	KPYR	Pyruvate kinase isozymes R/L	Cytoplasm
Bare-MSN	LDHA	L-lactate dehydrogenase A chain	Mitochondria
Bare-MSN	LDHB	L-lactate dehydrogenase B chain	Mitochondria
Bare-MSN	POTEE	POTE ankyrin domain family member E	Secretory
Bare-MSN	POTEF	POTE ankyrin domain family member F	Secretory
Bare-MSN	POTEI	POTE ankyrin domain family member I	Secretory
Bare-MSN	POTEJ	POTE ankyrin domain family member J	Secretory
Bare-MSN	PROF1	Profilin-1	Cytoplasm
Bare-MSN	TBA1A	Tubulin alpha-1A chain	Secretory
Bare-MSN	TBA1B	Tubulin alpha-1B chain	Secretory
Bare-MSN	TBA1C	Tubulin alpha-1C chain	Secretory
Bare-MSN	TBB5	Tubulin beta chain	Secretory
Bare-MSN	UBB	Polyubiquitin-B	Secretory
Bare-MSN	UBC	Polyubiquitin-C	Secretory
Bare-MSN	VIME	Vimentin	---
PEI-MSN	ALBU	Serum albumin	Cytoskeleton
Phos-MSN	4F2	Isoform 4 of 4F2 cell-surface antigen heavy chain	Secretory
Phos-MSN	ACTA	Actin_ aortic smooth muscle	Cytoplasm
Phos-MSN	ACTB	Actin_ cytoplasmic 1	Cytoplasm
Phos-MSN	ACTBL	Beta-actin-like protein 2	Cytoplasm
Phos-MSN	ACTBM	Putative beta-actin-like protein 3	Cytoplasm
Phos-MSN	ACTC	Actin_ alpha cardiac muscle 1	Cytoplasm
Phos-MSN	ACTG	Actin_ cytoplasmic 2	Cytoplasm
Phos-MSN	ACTH	Actin_ gamma-enteric smooth muscle	Cytoplasm
Phos-MSN	ACTN1	Alpha-actinin-1	Cytoplasm
Phos-MSN	ACTN4	Alpha-actinin-4	Cytoplasm
Phos-MSN	ACTS	Actin_ alpha skeletal muscle	Cytoplasm
Phos-MSN	AK1BA	Aldo-keto reductase family 1 member B10	Cytoplasm
Phos-MSN	AK1C3	Aldo-keto reductase family 1 member C3	Cytoplasm
Phos-MSN	AN36A	Ankyrin repeat domain-containing protein 36A	Cytoplasm
Phos-MSN	AN36C	Ankyrin repeat domain-containing protein 36C	Cytoplasm
Phos-MSN	ANXA1	Annexin A1	Nucleus
Phos-MSN	CA173	Uncharacterized protein C1orf173	---
Phos-MSN	CCD30	Coiled-coil domain-containing protein 30	Secretory
Phos-MSN	CEP89	Centrosomal protein of 89 kDa	Cytoplasm
Phos-MSN	DAAM2	Disheveled-associated activator of morphogenesis 2	---
Phos-MSN	DAPLE	Protein Daple	Cytoplasm
Phos-MSN	EF1A1	Elongation factor 1-alpha 1	Cytoskeleton
Phos-MSN	EF1A2	Elongation factor 1-alpha 2	Cytoskeleton

Phos-MSN	EF1A3	Putative elongation factor 1-alpha-like 3	Cytoskeleton
Phos-MSN	EGFLA	Pikachurin	Secretory
Phos-MSN	ENPL	Endoplasmin	Secretory
Phos-MSN	F184A	Protein FAM184A	---
Phos-MSN	FYCO1	FYVE and coiled-coil domain-containing protein 1	Secretory
Phos-MSN	G3P	Glyceraldehyde-3-phosphate dehydrogenase	Cytoplasm
Phos-MSN	GRIN1	G protein-regulated inducer of neurite outgrowth 1	Transmembrane
Phos-MSN	GRP78	78 kDa glucose-regulated protein	Mitochondria
Phos-MSN	GSTA4	Glutathione S-transferase A4	Cytoplasm
Phos-MSN	GUAD	Isoform 2 of Guanine deaminase	---
Phos-MSN	H12	Histone H1.2	Nucleus
Phos-MSN	H13	Histone H1.3	Nucleus
Phos-MSN	H14	Histone H1.4	Nucleus
Phos-MSN	H2A1	Histone H2A type 1	Cytoskeleton
Phos-MSN	H2A1A	Histone H2A type 1-A	Cytoskeleton
Phos-MSN	H2A1B	Histone H2A type 1-B/E	Cytoskeleton
Phos-MSN	H2A1C	Histone H2A type 1-C	Nucleus
Phos-MSN	H2A1D	Histone H2A type 1-D	Nucleus
Phos-MSN	H2A1H	Histone H2A type 1-H	Nucleus
Phos-MSN	H2A1J	Histone H2A type 1-J	Nucleus
Phos-MSN	H2A2A	Histone H2A type 2-A	Nucleus
Phos-MSN	H2A2B	Histone H2A type 2-B	Nucleus
Phos-MSN	H2A2C	Histone H2A type 2-C	Nucleus
Phos-MSN	H2A3	Histone H2A type 3	Nucleus
Phos-MSN	H2AJ	Histone H2A.J	Nucleus
Phos-MSN	H2AV	Isoform 2 of Histone H2A.V	Nucleus
Phos-MSN	H2AX	Histone H2A.x	Nucleus
Phos-MSN	H2AZ	Histone H2A.Z	Nucleus
Phos-MSN	H2B1A	Histone H2B type 1-A	Nucleus
Phos-MSN	H2B1B	Histone H2B type 1-B	Nucleus
Phos-MSN	H2B1C	Histone H2B type 1-C/E/F/G/I	Nucleus
Phos-MSN	H2B1D	Histone H2B type 1-D	Nucleus
Phos-MSN	H2B1H	Histone H2B type 1-H	Nucleus
Phos-MSN	H2B1J	Histone H2B type 1-J	Nucleus
Phos-MSN	H2B1K	Histone H2B type 1-K	Nucleus
Phos-MSN	H2B1L	Histone H2B type 1-L	Nucleus
Phos-MSN	H2B1M	Histone H2B type 1-M	Nucleus
Phos-MSN	H2B1N	Histone H2B type 1-N	Nucleus
Phos-MSN	H2B1O	Histone H2B type 1-O	Nucleus
Phos-MSN	H2B2E	Histone H2B type 2-E	Nucleus
Phos-MSN	H2B2F	Histone H2B type 2-F	Nucleus
Phos-MSN	H2B3B	Histone H2B type 3-B	Nucleus
Phos-MSN	H2BFS	Histone H2B type F-S	Nucleus
Phos-MSN	H31	Histone H3.1	Nucleus
Phos-MSN	H31T	Histone H3.1t	Nucleus
Phos-MSN	H32	Histone H3.2	Nucleus
Phos-MSN	H33	Histone H3.3	Nucleus
Phos-MSN	H3C	Histone H3.3C	Nucleus
Phos-MSN	H90B2	Putative heat shock protein HSP 90-beta 2	Cytoplasm
Phos-MSN	H90B3	Putative heat shock protein HSP 90-beta-3	Cytoplasm
Phos-MSN	H90B4	Putative heat shock protein HSP 90-beta 4	Cytoplasm
Phos-MSN	HS71L	Heat shock 70 kDa protein 1-like	Cytoplasm
Phos-MSN	HS90A	Heat shock protein HSP 90-alpha	Cytoplasm
Phos-MSN	HS90B	Heat shock protein HSP 90-beta	Cytoplasm
Phos-MSN	HSP72	Heat shock-related 70 kDa protein 2	Cytoplasm
Phos-MSN	HSP7C	Heat shock cognate 71 kDa protein	Cytoplasm
Phos-MSN	KIF15	Kinesin-like protein KIF15	Nucleus
Phos-MSN	KIF5C	Kinesin heavy chain isoform 5C	Nucleus

Phos-MSN	KIZ	Centrosomal protein kizuna	Nucleus
Phos-MSN	KPYM	Pyruvate kinase isozymes M1/M2	Cytoplasm
Phos-MSN	KPYR	Pyruvate kinase isozymes R/L	Cytoplasm
Phos-MSN	MAP2	Microtubule-associated protein 2	Cytoplasm
Phos-MSN	MYH7B	Myosin-7B	Cytoplasm
Phos-MSN	PCM1	Pericentriolar material 1 protein	Cytoplasm
Phos-MSN	PLIN4	Perilipin-4	---
Phos-MSN	POTEE	POTE ankyrin domain family member E	Secretory
Phos-MSN	POTEF	POTE ankyrin domain family member F	Secretory
Phos-MSN	POTEI	POTE ankyrin domain family member I	Secretory
Phos-MSN	POTEJ	POTE ankyrin domain family member J	Secretory
Phos-MSN	PRDX1	Peroxiredoxin-1	Cytoplasm
Phos-MSN	RL40	Ubiquitin-60S ribosomal protein L40	Cytoplasm
Phos-MSN	RRBP1	Ribosome-binding protein 1	Cytoplasm
Phos-MSN	RS27A	Ubiquitin-40S ribosomal protein S27a	Cytoplasm
Phos-MSN	RS6	40S ribosomal protein S6	Cytoplasm
Phos-MSN	SPRR3	Small proline-rich protein 3	Cytoplasm
Phos-MSN	SREK1	Splicing regulatory glutAmine/lysine-rich protein 1	---
Phos-MSN	TARA	Isoform 4 of TRIO and F-actin-binding protein	---
Phos-MSN	TBA1A	Tubulin alpha-1A chain	Secretory
Phos-MSN	TBA1B	Tubulin alpha-1B chain	Secretory
Phos-MSN	TBA1C	Tubulin alpha-1C chain	Secretory
Phos-MSN	TBA3C	Isoform 2 of Tubulin alpha-3C/D chain	Secretory
Phos-MSN	TBA3E	Tubulin alpha-3E chain	Secretory
Phos-MSN	TBA4A	Tubulin alpha-4A chain	Secretory
Phos-MSN	TBA8	Tubulin alpha-8 chain	Secretory
Phos-MSN	TBB2A	Tubulin beta-2A chain	Secretory
Phos-MSN	TBB2B	Tubulin beta-2B chain	Secretory
Phos-MSN	TBB3	Tubulin beta-3 chain	Secretory
Phos-MSN	TBB4A	Tubulin beta-4A chain	Secretory
Phos-MSN	TBB4B	Tubulin beta-4B chain	Secretory
Phos-MSN	TBB5	Tubulin beta chain	Secretory
Phos-MSN	TBB6	Tubulin beta-6 chain	Secretory
Phos-MSN	THOC2	THO complex subunit 2	Nucleus
Phos-MSN	UBB	Polyubiquitin-B	Secretory
Phos-MSN	UBC	Polyubiquitin-C	Secretory
Phos-MSN	XXLT1	Xyloside xylosyltransferase 1	---
Phos-MSN	ZC3HD	Isoform 2 of Zinc finger CCCH domain-containing protein 13	Secretory

Table 4.4. Human proteins identified from MSNs incubated with MCF7 cells.

Particle Type	Protein ID	Protein Name	Subcellular Localization
Amine-MSN	ALBU	Serum albumin	Secretory
Amine-MSN	FETUA	Alpha-2-HS-glycoprotein	Cytoskeleton
Bare-MSN	ACTA	Actin_ aortic smooth muscle	Cytoplasm
Bare-MSN	ACTB	Actin_ cytoplasmic 1	Cytoplasm
Bare-MSN	ACTC	Actin_ alpha cardiac muscle 1	Cytoplasm
Bare-MSN	ACTG	Actin_ cytoplasmic 2	Cytoplasm
Bare-MSN	ACTH	Actin_ gamma-enteric smooth muscle	Cytoplasm
Bare-MSN	ACTS	Actin_ alpha skeletal muscle	Cytoplasm
Bare-MSN	ADT2	ADP/ATP translocase 2	Cytoplasm
Bare-MSN	ADT3	ADP/ATP translocase 3	Cytoplasm
Bare-MSN	AGR2	Anterior gradient protein 2 homolog	Secretory
Bare-MSN	ALBU	Serum albumin	Secretory
Bare-MSN	BIRC5	Isoform 2 of Baculoviral IAP repeat-containing protein 5	Cytoskeleton
Bare-MSN	CH10	10 kDa heat shock protein_ mitochondrial	Cytoskeleton
Bare-MSN	CH60	60 kDa heat shock protein_ mitochondrial	Mitochondria
Bare-MSN	HBB	Hemoglobin subunit beta	Cytoplasm
Bare-MSN	HBD	Hemoglobin subunit delta	Cytoplasm
Bare-MSN	HBE	Hemoglobin subunit epsilon	Cytoplasm
Bare-MSN	HBG1	Hemoglobin subunit gamma-1	Cytoplasm
Bare-MSN	HBG2	Hemoglobin subunit gamma-2	Cytoplasm
Bare-MSN	HS902	Putative heat shock protein HSP 90-alpha A2	Cytoplasm
Bare-MSN	HXD9	Homeobox protein Hox-D9	Cytoplasm
Bare-MSN	PI4K2A	Phosphatidylinositol 4-kinase type 2-alpha	Secretory
Bare-MSN	PODN	Isoform 2 of Podocan	Secretory
Bare-MSN	RL40	Ubiquitin-60S ribosomal protein L40	Secretory
Bare-MSN	RS27A	Ubiquitin-40S ribosomal protein S27a	Secretory
Bare-MSN	S2546	Solute carrier family 25 member 46	Mitochondria
Bare-MSN	UBB	Polyubiquitin-B	Secretory
Bare-MSN	UBC	Polyubiquitin-C	Secretory
Bare-MSN	UHMK1	Isoform 2 of Serine/threonine-protein kinase Kist	Cytoplasm
Bare-MSN	VIME	Vimentin	Cytoplasm
Bare-MSN	ZN616	Zinc finger protein 616	Nucleus
Bare-MSN	ZN655	Isoform 3 of Zinc finger protein 655	Nucleus
PEI-MSN	HBB	Hemoglobin subunit beta	Cytoplasm
PEI-MSN	HBD	Hemoglobin subunit delta	Cytoplasm
PEI-MSN	VTNC	Vitronectin	Secretory
Phos-MSN	MK12	Mitogen-activated protein kinase 12	Cytoplasm

Table 4.5. Bovine proteins identified from MSNs incubated with A549, HFF, and MCF7 cells.

Cell Line	Particle Type	Protein ID	Protein Name
A549	Amine-MSN	A5D7M6	KRT5 protein
A549	Amine-MSN	A6QNZ7	Keratin 10 (Epidermolytic hyperkeratosis; keratosis palmaris et plantaris)
A549	Amine-MSN	ALBU	Serum albumin
A549	Amine-MSN	B0JYQ0	ALB protein
A549	Amine-MSN	E1B991	Uncharacterized protein
A549	Amine-MSN	G3MXL3	Uncharacterized protein (Fragment)
A549	Amine-MSN	G3MYU2	Uncharacterized protein
A549	Amine-MSN	G3MZ71	Uncharacterized protein
A549	Amine-MSN	G3N0V2	Uncharacterized protein
A549	Bare-MSN	A0JNH4	Breast carcinoma amplified sequence 1
A549	Bare-MSN	A4IFP6	GIMAP1 protein
A549	Bare-MSN	A5D7M6	KRT5 protein
A549	Bare-MSN	A6QNZ7	Keratin 10 (Epidermolytic hyperkeratosis; keratosis palmaris et plantaris)
A549	Bare-MSN	ALBU	Serum albumin
A549	Bare-MSN	APOA1	Apolipoprotein A-I
A549	Bare-MSN	B0JYK1	BCAS1 protein
A549	Bare-MSN	B0JYN6	Alpha-2-HS-glycoprotein
A549	Bare-MSN	B0JYQ0	ALB protein
A549	Bare-MSN	E1B822	Uncharacterized protein
A549	Bare-MSN	F1MNI3	Uncharacterized protein
A549	Bare-MSN	F2Y907	Zinc finger protein 507 (Fragment)
A549	Bare-MSN	F6QP30	Uncharacterized protein
A549	Bare-MSN	FETUA	Alpha-2-HS-glycoprotein
A549	Bare-MSN	G3MXL3	Uncharacterized protein (Fragment)
A549	Bare-MSN	G3MYU2	Uncharacterized protein
A549	Bare-MSN	G3N0V2	Uncharacterized protein
A549	Bare-MSN	HBBF	Hemoglobin fetal subunit beta
A549	Bare-MSN	Q0VBY4	Tumor protein D52-like 1
A549	Bare-MSN	RANDOM1653	Random Sequence 1653
A549	PEI-MSN	A5D792	DCK protein
A549	PEI-MSN	A5D7M6	KRT5 protein
A549	PEI-MSN	ALBU	Serum albumin
A549	PEI-MSN	B0JYN6	Alpha-2-HS-glycoprotein
A549	PEI-MSN	B0JYQ0	ALB protein
A549	PEI-MSN	E1B7N2	Histone H4
A549	PEI-MSN	E1B9M9	Histone H4
A549	PEI-MSN	E1BBP7	Histone H4
A549	PEI-MSN	E1BLC2	Histone H4
A549	PEI-MSN	FETUA	Alpha-2-HS-glycoprotein
A549	PEI-MSN	G3MXL3	Uncharacterized protein (Fragment)
A549	PEI-MSN	G3MYX0	Histone H4
A549	PEI-MSN	G3N081	Histone H4
A549	PEI-MSN	G3N2B8	Histone H4
A549	PEI-MSN	G3X807	Histone H4 (Fragment)
A549	PEI-MSN	H4	Histone H4
A549	PEI-MSN	RANDOM29734	Random Sequence 29734
A549	Phos-MSN	A5D7M6	KRT5 protein
A549	Phos-MSN	A6QNZ7	Keratin 10 (Epidermolytic hyperkeratosis; keratosis palmaris et plantaris)
A549	Phos-MSN	A7YK65	Toll-like receptor 1
A549	Phos-MSN	A7YK67	Toll-like receptor 1
A549	Phos-MSN	ALBU	Serum albumin
A549	Phos-MSN	APOA1	Apolipoprotein A-I
A549	Phos-MSN	B0JYN6	Alpha-2-HS-glycoprotein
A549	Phos-MSN	B0JYQ0	ALB protein

A549	Phos-MSN	B5TYW4	Toll-like receptor
A549	Phos-MSN	F1N566	Uncharacterized protein (Fragment)
A549	Phos-MSN	F6PRB5	Uncharacterized protein
A549	Phos-MSN	FETUA	Alpha-2-HS-glycoprotein
A549	Phos-MSN	G3MXL3	Uncharacterized protein (Fragment)
A549	Phos-MSN	G3N0V2	Uncharacterized protein
A549	Phos-MSN	Q3T172	ECH1 protein (Fragment)
A549	Phos-MSN	Q4TU52	Toll-like receptor 1 (Fragment)
A549	Phos-MSN	Q5EBY8	ECH1-like protein (Fragment)
A549	Phos-MSN	Q6GV21	Toll-like receptor 1
A549	Phos-MSN	RANDOM18029	Random Sequence 18029
HFF	Amine-MSN	1433F	14-3-3 protein eta
HFF	Amine-MSN	A3KN00	DUSP23 protein
HFF	Amine-MSN	A4FUB9	ACIN1 protein (Fragment)
HFF	Amine-MSN	A4IFM8	Actin_ alpha 1_ skeletal muscle
HFF	Amine-MSN	A5D792	DCK protein
HFF	Amine-MSN	A5D7J0	ACTA2 protein
HFF	Amine-MSN	A5D7M6	KRT5 protein
HFF	Amine-MSN	A5D7N2	Histone H2B
HFF	Amine-MSN	A6QP97	E3 ubiquitin-protein ligase RNF220
HFF	Amine-MSN	A7E3E1	HSPCA protein (Fragment)
HFF	Amine-MSN	A7E3Q2	Heat shock 70kDa protein 1A
HFF	Amine-MSN	A7Z082	ACIN1 protein
HFF	Amine-MSN	ACTA	Actin_ aortic smooth muscle
HFF	Amine-MSN	ACTB	Actin_ cytoplasmic 1
HFF	Amine-MSN	ACTC	Actin_ alpha cardiac muscle 1
HFF	Amine-MSN	ACTG	Actin_ cytoplasmic 2
HFF	Amine-MSN	ACTH	Actin_ gamma-enteric smooth muscle
HFF	Amine-MSN	ACTS	Actin_ alpha skeletal muscle
HFF	Amine-MSN	AINX	Alpha-internexin
HFF	Amine-MSN	ALBU	Serum albumin
HFF	Amine-MSN	APOA1	Apolipoprotein A-I
HFF	Amine-MSN	ATPA	ATP synthase subunit alpha_ mitochondrial
HFF	Amine-MSN	B0JYQ0	ALB protein
HFF	Amine-MSN	CH10	10 kDa heat shock protein_ mitochondrial
HFF	Amine-MSN	CSH1	Chorionic somatomammotropin hormone 1
HFF	Amine-MSN	D3U796	Nucleophosmin
HFF	Amine-MSN	D4QBB3	Hemoglobin beta
HFF	Amine-MSN	D4QBB4	Hemoglobin beta
HFF	Amine-MSN	E1B7J1	Elongation factor 1-alpha
HFF	Amine-MSN	E1B8G9	Histone H2B
HFF	Amine-MSN	E1B8K6	Uncharacterized protein
HFF	Amine-MSN	E1B9F6	Elongation factor 1-alpha
HFF	Amine-MSN	E1B9K1	Polyubiquitin-C
HFF	Amine-MSN	E1B9M9	Histone H4
HFF	Amine-MSN	E1BBP7	Histone H4
HFF	Amine-MSN	E1BDE9	Uncharacterized protein
HFF	Amine-MSN	E1BED8	Elongation factor 1-alpha (Fragment)
HFF	Amine-MSN	E1BEL8	Uncharacterized protein
HFF	Amine-MSN	E1BGW2	Histone H2B
HFF	Amine-MSN	E1BK75	Histone H2B
HFF	Amine-MSN	E1BKX5	Uncharacterized protein
HFF	Amine-MSN	E1BLC2	Histone H4
HFF	Amine-MSN	E1BLK2	Uncharacterized protein
HFF	Amine-MSN	E1BPF4	Elongation factor 1-alpha (Fragment)
HFF	Amine-MSN	E1BPK0	Uncharacterized protein
HFF	Amine-MSN	E3SAZ8	Nucleophosmin
HFF	Amine-MSN	EF1A1	Elongation factor 1-alpha 1

HFF	Amine-MSN	EF1A2	Elongation factor 1-alpha 2
HFF	Amine-MSN	ENPL	Endoplasmin
HFF	Amine-MSN	F1MBN8	Uncharacterized protein
HFF	Amine-MSN	F1MJW1	Uncharacterized protein (Fragment)
HFF	Amine-MSN	F1MKC4	Uncharacterized protein
HFF	Amine-MSN	F1MKC4	Uncharacterized protein
HFF	Amine-MSN	F1MLB8	ATP synthase subunit alpha
HFF	Amine-MSN	F1MLB8	ATP synthase subunit alpha
HFF	Amine-MSN	F1MM88	Uncharacterized protein (Fragment)
HFF	Amine-MSN	F1MNF8	Uncharacterized protein
HFF	Amine-MSN	F1MQG6	Uncharacterized protein
HFF	Amine-MSN	F1MRD0	Actin_ cytoplasmic 1
HFF	Amine-MSN	F1MTV9	Uncharacterized protein
HFF	Amine-MSN	F1MUB8	Uncharacterized protein
HFF	Amine-MSN	F1MUD2	Histone H2B
HFF	Amine-MSN	F1MUU9	Uncharacterized protein (Fragment)
HFF	Amine-MSN	F1MV26	Uncharacterized protein
HFF	Amine-MSN	F1MYF0	Chorionic somatomammotropin hormone 2
HFF	Amine-MSN	F1MYL0	E3 ubiquitin-protein ligase RNF220
HFF	Amine-MSN	F1N453	Histone H2B
HFF	Amine-MSN	F1N614	Uncharacterized protein
HFF	Amine-MSN	F2Z4C1	Uncharacterized protein
HFF	Amine-MSN	F2Z4E8	Histone H2B
HFF	Amine-MSN	F2Z4F9	Histone H2B
HFF	Amine-MSN	F2Z4K0	Uncharacterized protein
HFF	Amine-MSN	F6RP72	Uncharacterized protein (Fragment)
HFF	Amine-MSN	G3MWH4	Uncharacterized protein
HFF	Amine-MSN	G3MX03	Uncharacterized protein
HFF	Amine-MSN	G3MXG1	Uncharacterized protein
HFF	Amine-MSN	G3MXL3	Uncharacterized protein (Fragment)
HFF	Amine-MSN	G3MXT4	Uncharacterized protein
HFF	Amine-MSN	G3MY27	Uncharacterized protein
HFF	Amine-MSN	G3MYJ0	Uncharacterized protein
HFF	Amine-MSN	G3MYV4	Histone H2B
HFF	Amine-MSN	G3MZ21	Uncharacterized protein
HFF	Amine-MSN	G3MZL8	Uncharacterized protein (Fragment)
HFF	Amine-MSN	G3MZR4	Histone H2B
HFF	Amine-MSN	G3N011	Uncharacterized protein
HFF	Amine-MSN	G3N053	Histone H2B
HFF	Amine-MSN	G3N068	Histone H2B
HFF	Amine-MSN	G3N080	Histone H2B (Fragment)
HFF	Amine-MSN	G3N081	Histone H4
HFF	Amine-MSN	G3N0L9	Uncharacterized protein
HFF	Amine-MSN	G3N0V2	Uncharacterized protein
HFF	Amine-MSN	G3N1C9	Histone H2B
HFF	Amine-MSN	G3N1R5	Uncharacterized protein
HFF	Amine-MSN	G3N1Y3	Uncharacterized protein (Fragment)
HFF	Amine-MSN	G3N2B8	Histone H4
HFF	Amine-MSN	G3N2F0	Elongation factor 1-alpha
HFF	Amine-MSN	G3N2V5	Heat shock protein HSP 90-beta
HFF	Amine-MSN	G3N3L9	Uncharacterized protein
HFF	Amine-MSN	G3P	Glyceraldehyde-3-phosphate dehydrogenase
HFF	Amine-MSN	G3X7M4	Uncharacterized protein
HFF	Amine-MSN	G3X807	Histone H4 (Fragment)
HFF	Amine-MSN	G5E507	Heat shock protein HSP 90-beta
HFF	Amine-MSN	G5E6I9	Histone H2B
HFF	Amine-MSN	G8JKX4	Actin_ aortic smooth muscle
HFF	Amine-MSN	G8JL06	Histone H2B

HFF	Amine-MSN	GRP78	78 kDa glucose-regulated protein
HFF	Amine-MSN	H2B1	Histone H2B type 1
HFF	Amine-MSN	H2B1K	Histone H2B type 1-K
HFF	Amine-MSN	H2B1N	Histone H2B type 1-N
HFF	Amine-MSN	H4	Histone H4
HFF	Amine-MSN	HBB	Hemoglobin subunit beta
HFF	Amine-MSN	HBBF	Hemoglobin fetal subunit beta
HFF	Amine-MSN	HBE2	Hemoglobin subunit epsilon-2
HFF	Amine-MSN	HBE4	Hemoglobin subunit epsilon-4
HFF	Amine-MSN	HS71A	Heat shock 70 kDa protein 1A
HFF	Amine-MSN	HS71L	Heat shock 70 kDa protein 1-like
HFF	Amine-MSN	HS90A	Heat shock protein HSP 90-alpha
HFF	Amine-MSN	HS90B	Heat shock protein HSP 90-beta
HFF	Amine-MSN	HSP72	Heat shock-related 70 kDa protein 2
HFF	Amine-MSN	HSP7C	Heat shock cognate 71 kDa protein
HFF	Amine-MSN	HSP7C	Heat shock cognate 71 kDa protein
HFF	Amine-MSN	M5FJZ9	Heat shock protein 75 kDa_ mitochondrial
HFF	Amine-MSN	NPM	Nucleophosmin
HFF	Amine-MSN	O18787	Elongation factor 1 alpha (Fragment)
HFF	Amine-MSN	Q0QES8	Glyceraldehyde-3-phosphate dehydrogenase (Fragment)
HFF	Amine-MSN	Q28163	Placental lactogen (Fragment)
HFF	Amine-MSN	Q2KII5	Histone H2B
HFF	Amine-MSN	Q2QJG3	Beta-actin (Fragment)
HFF	Amine-MSN	Q32S29	Histone H2B
HFF	Amine-MSN	Q3SZD6	HSP90AB1 protein (Fragment)
HFF	Amine-MSN	Q3T007	HSPCA protein (Fragment)
HFF	Amine-MSN	Q3ZBS7	Uncharacterized protein
HFF	Amine-MSN	Q58D76	Proteasome 26S non-ATPase subunit 4 isoform 1
HFF	Amine-MSN	Q58DT9	Alpha 2 actin
HFF	Amine-MSN	Q5JB60	Nucleolin (Fragment)
HFF	Amine-MSN	Q712W6	Glyceraldehyde-3-phosphate dehydrogenase (Fragment)
HFF	Amine-MSN	Q861V2	Similar to 7O kDa heat shock cognate protein (Fragment)
HFF	Amine-MSN	Q862L2	Similar to alpha-tubulin isoform 1 (Fragment)
HFF	Amine-MSN	Q862L7	Similar to elongation factor 1 alpha (Fragment)
HFF	Amine-MSN	Q862P9	Similar to beta actin (Fragment)
HFF	Amine-MSN	Q862R6	Similar to elongation factor 1 alpha (Fragment)
HFF	Amine-MSN	Q865A1	Heat shock protein 90 beta (Fragment)
HFF	Amine-MSN	Q9TTW4	Beta actin (Fragment)
HFF	Amine-MSN	RANDOM11686	Random Sequence 11686
HFF	Amine-MSN	RANDOM12679	Random Sequence 12679
HFF	Amine-MSN	RANDOM1273	Random Sequence 1273
HFF	Amine-MSN	RANDOM1653	Random Sequence 1653
HFF	Amine-MSN	RANDOM25591	Random Sequence 25591
HFF	Amine-MSN	RANDOM28104	Random Sequence 28104
HFF	Amine-MSN	RANDOM450	Random Sequence 450
HFF	Amine-MSN	RANDOM4902	Random Sequence 4902
HFF	Amine-MSN	RL40	Ubiquitin-60S ribosomal protein L40
HFF	Amine-MSN	RN220	E3 ubiquitin-protein ligase RNF220
HFF	Amine-MSN	RS27A	Ubiquitin-40S ribosomal protein S27a
HFF	Amine-MSN	TBA1B	Tubulin alpha-1B chain
HFF	Amine-MSN	TBA1C	Tubulin alpha-1C chain
HFF	Amine-MSN	TBA1D	Tubulin alpha-1D chain
HFF	Amine-MSN	TBA3	Tubulin alpha-3 chain
HFF	Amine-MSN	TBB5	Tubulin beta-5 chain
HFF	Amine-MSN	TRAP1	Heat shock protein 75 kDa_ mitochondrial
HFF	Amine-MSN	UBB	Polyubiquitin-B
HFF	Amine-MSN	UBC	Polyubiquitin-C
HFF	Amine-MSN	VIME	Vimentin

HFF	Bare-MSN	A4IFM8	Actin_ alpha 1_ skeletal muscle
HFF	Bare-MSN	A5D7J0	ACTA2 protein
HFF	Bare-MSN	A5D7M6	KRT5 protein
HFF	Bare-MSN	A6QNZ7	Keratin 10 (Epidermolytic hyperkeratosis; keratosis palmaris et plantaris)
HFF	Bare-MSN	ACTA	Actin_ aortic smooth muscle
HFF	Bare-MSN	ACTB	Actin_ cytoplasmic 1
HFF	Bare-MSN	ACTC	Actin_ alpha cardiac muscle 1
HFF	Bare-MSN	ACTG	Actin_ cytoplasmic 2
HFF	Bare-MSN	ACTH	Actin_ gamma-enteric smooth muscle
HFF	Bare-MSN	ACTS	Actin_ alpha skeletal muscle
HFF	Bare-MSN	APOA1	Apolipoprotein A-I
HFF	Bare-MSN	B0JYN6	Alpha-2-HS-glycoprotein
HFF	Bare-MSN	D4QBB3	Hemoglobin beta
HFF	Bare-MSN	D4QBB4	Hemoglobin beta
HFF	Bare-MSN	E1B7N8	Uncharacterized protein
HFF	Bare-MSN	E1B991	Uncharacterized protein
HFF	Bare-MSN	E1B9M9	Histone H4
HFF	Bare-MSN	E1BBP7	Histone H4
HFF	Bare-MSN	E1BEL8	Uncharacterized protein
HFF	Bare-MSN	E1BLC2	Histone H4
HFF	Bare-MSN	F1MHL1	Uncharacterized protein (Fragment)
HFF	Bare-MSN	F1MIM6	Uncharacterized protein (Fragment)
HFF	Bare-MSN	F1MKC4	Uncharacterized protein
HFF	Bare-MSN	F1MM88	Uncharacterized protein (Fragment)
HFF	Bare-MSN	F1MRD0	Actin_ cytoplasmic 1
HFF	Bare-MSN	FETUA	Alpha-2-HS-glycoprotein
HFF	Bare-MSN	G3MXL3	Uncharacterized protein (Fragment)
HFF	Bare-MSN	G3MYU2	Uncharacterized protein
HFF	Bare-MSN	G3MZ71	Uncharacterized protein
HFF	Bare-MSN	G3N0V2	Uncharacterized protein
HFF	Bare-MSN	G3N1Y3	Uncharacterized protein (Fragment)
HFF	Bare-MSN	G3N2B8	Histone H4
HFF	Bare-MSN	G3X807	Histone H4 (Fragment)
HFF	Bare-MSN	G8JKX4	Actin_ aortic smooth muscle
HFF	Bare-MSN	H4	Histone H4
HFF	Bare-MSN	HBB	Hemoglobin subunit beta
HFF	Bare-MSN	HBBF	Hemoglobin fetal subunit beta
HFF	Bare-MSN	Q58DT9	Alpha 2 actin
HFF	Bare-MSN	Q862P9	Similar to beta actin (Fragment)
HFF	Bare-MSN	Q9TTW4	Beta actin (Fragment)
HFF	Bare-MSN	RANDOM16097	Random Sequence 16097
HFF	Bare-MSN	RANDOM1653	Random Sequence 1653
HFF	Bare-MSN	RANDOM17625	Random Sequence 17625
HFF	Bare-MSN	RT31	28S ribosomal protein S31_ mitochondrial
HFF	PEI-MSN	A4IFM8	Actin_ alpha 1_ skeletal muscle
HFF	PEI-MSN	A5D7J0	ACTA2 protein
HFF	PEI-MSN	A5D7M6	KRT5 protein
HFF	PEI-MSN	A6QNZ7	Keratin 10 (Epidermolytic hyperkeratosis; keratosis palmaris et plantaris)
HFF	PEI-MSN	ACTA	Actin_ aortic smooth muscle
HFF	PEI-MSN	ACTB	Actin_ cytoplasmic 1
HFF	PEI-MSN	ACTC	Actin_ alpha cardiac muscle 1
HFF	PEI-MSN	ACTG	Actin_ cytoplasmic 2
HFF	PEI-MSN	ACTH	Actin_ gamma-enteric smooth muscle
HFF	PEI-MSN	ACTS	Actin_ alpha skeletal muscle
HFF	PEI-MSN	ALBU	Serum albumin
HFF	PEI-MSN	APOA1	Apolipoprotein A-I
HFF	PEI-MSN	B0JYQ0	ALB protein
HFF	PEI-MSN	CDN2D	Cyclin-dependent kinase 4 inhibitor D

HFF	PEI-MSN	DRG2	Developmentally-regulated GTP-binding protein 2
HFF	PEI-MSN	E1B7J1	Elongation factor 1-alpha
HFF	PEI-MSN	E1B991	Uncharacterized protein
HFF	PEI-MSN	E1B9F6	Elongation factor 1-alpha
HFF	PEI-MSN	E1B9G8	Uncharacterized protein
HFF	PEI-MSN	E1B9K1	Polyubiquitin-C
HFF	PEI-MSN	E1BCU2	Uncharacterized protein
HFF	PEI-MSN	E1BED8	Elongation factor 1-alpha (Fragment)
HFF	PEI-MSN	E1BPF4	Elongation factor 1-alpha (Fragment)
HFF	PEI-MSN	EF1A1	Elongation factor 1-alpha 1
HFF	PEI-MSN	EF1A2	Elongation factor 1-alpha 2
HFF	PEI-MSN	F1MC11	Keratin_ type I cytoskeletal 14
HFF	PEI-MSN	F1MIM6	Uncharacterized protein (Fragment)
HFF	PEI-MSN	F1MJ66	Uncharacterized protein (Fragment)
HFF	PEI-MSN	F1MKC4	Uncharacterized protein
HFF	PEI-MSN	F1MM88	Uncharacterized protein (Fragment)
HFF	PEI-MSN	F1MNF8	Uncharacterized protein
HFF	PEI-MSN	F1MRD0	Actin_ cytoplasmic 1
HFF	PEI-MSN	F1MYV1	Uncharacterized protein (Fragment)
HFF	PEI-MSN	F2Z4C1	Uncharacterized protein
HFF	PEI-MSN	F2Z4K0	Uncharacterized protein
HFF	PEI-MSN	F6RP72	Uncharacterized protein (Fragment)
HFF	PEI-MSN	G3MXL3	Uncharacterized protein (Fragment)
HFF	PEI-MSN	G3MYU2	Uncharacterized protein
HFF	PEI-MSN	G3MZ71	Uncharacterized protein
HFF	PEI-MSN	G3N0V2	Uncharacterized protein
HFF	PEI-MSN	G3N1Y3	Uncharacterized protein (Fragment)
HFF	PEI-MSN	G3N2F0	Elongation factor 1-alpha
HFF	PEI-MSN	G3N3B9	Uncharacterized protein (Fragment)
HFF	PEI-MSN	G8JKX4	Actin_ aortic smooth muscle
HFF	PEI-MSN	HBBF	Hemoglobin fetal subunit beta
HFF	PEI-MSN	O18787	Elongation factor 1 alpha (Fragment)
HFF	PEI-MSN	Q17QL7	KRT15 protein
HFF	PEI-MSN	Q3ZBS7	Uncharacterized protein
HFF	PEI-MSN	Q58DT9	Alpha 2 actin
HFF	PEI-MSN	Q862L7	Similar to elongation factor 1 alpha (Fragment)
HFF	PEI-MSN	Q862P9	Similar to beta actin (Fragment)
HFF	PEI-MSN	Q862R6	Similar to elongation factor 1 alpha (Fragment)
HFF	PEI-MSN	Q9TTW4	Beta actin (Fragment)
HFF	PEI-MSN	RANDOM1549	Random Sequence 1549
HFF	PEI-MSN	RANDOM17853	Random Sequence 17853
HFF	PEI-MSN	RANDOM2905	Random Sequence 2905
HFF	PEI-MSN	RANDOM697	Random Sequence 697
HFF	PEI-MSN	RANDOM7813	Random Sequence 7813
HFF	PEI-MSN	RL40	Ubiquitin-60S ribosomal protein L40
HFF	PEI-MSN	RS27A	Ubiquitin-40S ribosomal protein S27a
HFF	PEI-MSN	TAGL2	Transgelin-2
HFF	PEI-MSN	TBA1B	Tubulin alpha-1B chain
HFF	PEI-MSN	TBA1C	Tubulin alpha-1C chain
HFF	PEI-MSN	TBA1D	Tubulin alpha-1D chain
HFF	PEI-MSN	UBB	Polyubiquitin-B
HFF	PEI-MSN	UBC	Polyubiquitin-C
MCF7	Amine-MSN	A1A4M3	KRT86 protein (Fragment)
MCF7	Amine-MSN	A1AT	Alpha-1-antiproteinase
MCF7	Amine-MSN	A3KMY1	KRT82 protein
MCF7	Amine-MSN	A3KN26	KRT33B protein
MCF7	Amine-MSN	A3KN26	KRT33B protein
MCF7	Amine-MSN	A4FV94	KRT6A protein

MCF7	Amine-MSN	A4IFP2	KRT4 protein
MCF7	Amine-MSN	A5D7M6	KRT5 protein
MCF7	Amine-MSN	A5PJJ1	KRT33A protein
MCF7	Amine-MSN	A5PJL3	MAPK12 protein
MCF7	Amine-MSN	A6H7D3	KRT18 protein (Fragment)
MCF7	Amine-MSN	A6QNZ7	Keratin 10 (Epidermolytic hyperkeratosis; keratosis palmaris et plantaris)
MCF7	Amine-MSN	A6QP32	KRT85 protein
MCF7	Amine-MSN	A6QP90	KRT32 protein
MCF7	Amine-MSN	ALBU	Serum albumin
MCF7	Amine-MSN	APOA1	Apolipoprotein A-I
MCF7	Amine-MSN	B0JYN6	Alpha-2-HS-glycoprotein
MCF7	Amine-MSN	B0JYQ0	ALB protein
MCF7	Amine-MSN	D4QBB4	Hemoglobin beta
MCF7	Amine-MSN	E1B898	Uncharacterized protein
MCF7	Amine-MSN	E1B991	Uncharacterized protein
MCF7	Amine-MSN	E1BFG1	Uncharacterized protein
MCF7	Amine-MSN	E1BIL2	Uncharacterized protein (Fragment)
MCF7	Amine-MSN	E1BPW6	Keratin_ type I cuticular Ha5
MCF7	Amine-MSN	F1MC11	Keratin_ type I cytoskeletal 14
MCF7	Amine-MSN	F1MDL7	Uncharacterized protein (Fragment)
MCF7	Amine-MSN	F1MFW9	Uncharacterized protein (Fragment)
MCF7	Amine-MSN	F1MI98	Uncharacterized protein
MCF7	Amine-MSN	F1MJ66	Uncharacterized protein (Fragment)
MCF7	Amine-MSN	F1MKE7	Uncharacterized protein (Fragment)
MCF7	Amine-MSN	F1MM88	Uncharacterized protein (Fragment)
MCF7	Amine-MSN	F1MNI3	Uncharacterized protein
MCF7	Amine-MSN	F1MSA6	Uncharacterized protein
MCF7	Amine-MSN	F1MUY2	Uncharacterized protein
MCF7	Amine-MSN	F1MV92	Uncharacterized protein (Fragment)
MCF7	Amine-MSN	F1MXG6	Uncharacterized protein
MCF7	Amine-MSN	F1N362	Uncharacterized protein
MCF7	Amine-MSN	F1N566	Uncharacterized protein (Fragment)
MCF7	Amine-MSN	F2Y907	Zinc finger protein 507 (Fragment)
MCF7	Amine-MSN	F6S1Q0	Uncharacterized protein
MCF7	Amine-MSN	FETUA	Alpha-2-HS-glycoprotein
MCF7	Amine-MSN	G3MXL3	Uncharacterized protein (Fragment)
MCF7	Amine-MSN	G3MYU2	Uncharacterized protein
MCF7	Amine-MSN	G3MZ71	Uncharacterized protein
MCF7	Amine-MSN	G3N0V2	Uncharacterized protein
MCF7	Amine-MSN	G3N0W8	Uncharacterized protein
MCF7	Amine-MSN	G3N1Y3	Uncharacterized protein (Fragment)
MCF7	Amine-MSN	G3X6C0	Inositol oxygenase
MCF7	Amine-MSN	G3X6N3	Serotransferrin
MCF7	Amine-MSN	G3X7W8	Uncharacterized protein (Fragment)
MCF7	Amine-MSN	HBB	Hemoglobin subunit beta
MCF7	Amine-MSN	HBBF	Hemoglobin fetal subunit beta
MCF7	Amine-MSN	M0QVY0	Uncharacterized protein
MCF7	Amine-MSN	MIOX	Inositol oxygenase
MCF7	Amine-MSN	O62659	Hair keratin A1 (Fragment)
MCF7	Amine-MSN	PI42C	Phosphatidylinositol 5-phosphate 4-kinase type-2 gamma
MCF7	Amine-MSN	Q0VD04	Keratin 85
MCF7	Amine-MSN	Q148I8	Keratin 31
MCF7	Amine-MSN	Q148J0	Keratin 34
MCF7	Amine-MSN	Q17QL7	KRT15 protein
MCF7	Amine-MSN	Q1HDH9	LOC507184 (Fragment)
MCF7	Amine-MSN	Q862F9	Similar to vimentin (Fragment)
MCF7	Amine-MSN	Q9TRP4	Fetuin (Fragment)
MCF7	Amine-MSN	RANDOM10786	Random Sequence 10786

MCF7	Amine-MSN	RANDOM12682	Random Sequence 12682
MCF7	Amine-MSN	RANDOM15146	Random Sequence 15146
MCF7	Amine-MSN	RANDOM16097	Random Sequence 16097
MCF7	Amine-MSN	RANDOM19162	Random Sequence 19162
MCF7	Amine-MSN	RANDOM19634	Random Sequence 19634
MCF7	Amine-MSN	RANDOM20132	Random Sequence 20132
MCF7	Amine-MSN	RANDOM28556	Random Sequence 28556
MCF7	Amine-MSN	RANDOM29734	Random Sequence 29734
MCF7	Amine-MSN	TRFE	Serotransferrin
MCF7	Amine-MSN	VIME	Vimentin
MCF7	Phos-MSN	Q8HY43	Early growth response protein 1 (Fragment)

CHAPTER 5

Delivery of Isoniazid to Mycobacterium Tuberculosis-Infected Macrophages via Mesoporous Silica Nanoparticle Prodrug System

5.1 Abstract

Tuberculosis is a major global health problem for which improved therapeutics are needed to shorten the course of treatment and to combat the emergence of drug resistance. Mycobacterium tuberculosis, is an intracellular pathogen of mononuclear phagocytes to cause tuberculosis. As such, it is an ideal pathogen for nanotherapeutics because macrophages ingest nanoparticles even without specific targeting molecules. Hence, a nanoparticle drug delivery system has the potential to target and deliver high concentrations of drug directly into *M. tuberculosis*-infected cells– greatly enhancing efficacy while avoiding off-target toxicities. We developed stimulus-responsive mesoporous silica nanoparticles of two different sizes, 100 nm and 50 nm, as carriers for the major anti-tuberculosis drug isoniazid in a prodrug configuration. The drug is captured by the aldehyde-functionalized nanoparticle through the formation of hydrazone bonds and released from the nanoparticles in response to acidic pH at levels that naturally occur within acidified endolysosomes. Isoniazid-loaded nanoparticles are ingested by *M. tuberculosis*-infected human macrophages and kill the intracellular bacteria in a dose-dependent manner. We further demonstrate in a mouse model of pulmonary tuberculosis that the nanoparticles are well tolerated and that they are much more efficacious than an equivalent amount of free drug.

5.2. Introduction

Tuberculosis (TB) is a devastating disease and global health problem that infects one third of the world's population, as recognized by the World Health Organization. Although effective antibiotics are available, serious toxic side effects limit the doses that can be used. For example, three of the first line drugs for treating TB – isoniazid (INH), rifampicin (RIF), and pyrazinamide (PZA) – are limited by hepatotoxicity.[1,2] INH in particular, a potent first line anti-TB drug used in standard regimens both for active and latent TB, at standard therapeutic dosages in humans, has adverse effects including neurotoxicity, optic neuritis, and severe hepatic injury.[1] As these side effects are due to the action of the drug on hepatocytes and neuronal cells rather than on macrophages, the primary host cells of M. tuberculosis, selective delivery of these antibiotics into macrophages has the potential to increase greatly their therapeutic index by achieving higher drug concentrations locally. Moreover, because drug resistance develops when bacteria are treated with sub-therapeutic levels of antibiotics, a system that delivers high concentrations of antibiotic to the site where bacteria divide would aid sterilizing sites of infection and minimize emergence of drug resistance.

Mesoporous silica nanoparticles (MSNs) offer many advantages over other delivery vehicles (e.g. liposomes, solid lipid particles, alginates) for drugs because of their stability, uniformity, inherent lack of toxicity, high internal surface area for drug binding, and versatility in incorporating additional design features.[3–6] While these nanoparticle delivery systems for TB drugs offer advantages over free drug, they have disadvantages compared with mesoporous silica nanoparticles (MSNs) which have the advantages of stability, uniformity, inherent lack of toxicity, capacity to encapsulate exceptionally high concentrations of different types of cargo, and most importantly, versatility in incorporating additional design features. Due to their high surface area (~1000 m^2/g), MSNs can encapsulate exceptionally high concentrations of different types of cargos. Their diverse

chemistry enables a variety of different internal and surface design features that can incorporate multiple concurrent functions such as stimuli-responsive release of cargo under specific conditions, imaging, and targeting molecules.[4]

MSNs are synthesized by simple, solution-based procedure that has been well established in literature.[7,8] In order to synthesize the nanoparticles, surfactant (cetyltrimethylammonium bromide, CTAB) is dissolved in a basic aqueous solution, and the micelles assemble into a 2-dimensional hexagonal structure to serve as templating agent for the porous structure. The solution is heated and the silica precursor (tetraethyl orthosilicate, TEOS) is condensed around the surfactant template in a base-catalyzed reaction. The solution is aged and the surfactant is extracted to produce 100 nm diameter MSNs with ~2 nm diameter pores. By adding an additional surfactant, a triblock copolymer Pluronic F127, to the solution can yield smaller MSNs (SMSNs) with 50 nm diameters, while maintaining the ~2 nm diameter pore size. The nonionic co-surfactant limits the growth of the CTAB micelle structure, to produces smaller nanoparticles.[9,10]

MSNs are predominantly used for delivery to a wide range of cancers, but MSNs-based drug delivery systems have also extended their range of applications to treat diabetes, atherosclerosis, and tuberculosis.[11–13] The encapsulation of anti-TB drugs within nanoparticles (NP) offers a mechanism for specific targeting of *Mtb*-infected cells. A system designed to achieve higher local concentrations of therapeutics where the bacteria replicate, without exposing the patient to high systemic concentrations, is crucial for improving the current regime of delivery. Therefore, a delivery mechanism that can selectively and safely introduce antibiotics into macrophages would greatly increase their therapeutic efficacy while reducing their toxicity.

Previously, we developed a pH-gated MSNs loaded with INH for treatment of TB, and we demonstrated efficacy against M. tuberculosis in an in vitro study.[14] However due to the small size of the INH molecule (~ 1 nm), the drug was difficult to trap inside the 2 nm MSNs pores. Because of

its relatively low loading capacity, the system was not a prime candidate to pursue in an in vivo analysis. In the present study, we have developed an entirely new MSNs-based INH delivery system and studied its efficacy against M. tuberculosis in vitro and in vivo. In this new design, INH is covalently bonded to MSNs via a hydrazone bond to form a pro-drug nanoparticle-based system[15,16]. The hydrazone bond is pH-sensitive and the unmodified INH can be reconstituted in acidic conditions, such as naturally occurs in the acidified endosomal/lysosomal compartment of macrophages after ingestion of particles. Finally, we coated the INH-loaded pH-responsive MSNs with a poly(ethylene imine)-poly(ethylene glycol) (PEI-PEG) co-polymer to improve their dispersability and stability (Figure 5.1). With this newly designed INH-loaded pH-responsive MSNs system, we demonstrate high loading of INH, excellent uptake by M. tuberculosis-infected macrophages, in vitro efficacy in killing intramacrophage M. tuberculosis, and in vivo efficacy in treating pulmonary tuberculosis in mice that is significantly greater than that achieved with equivalent amounts of free INH.

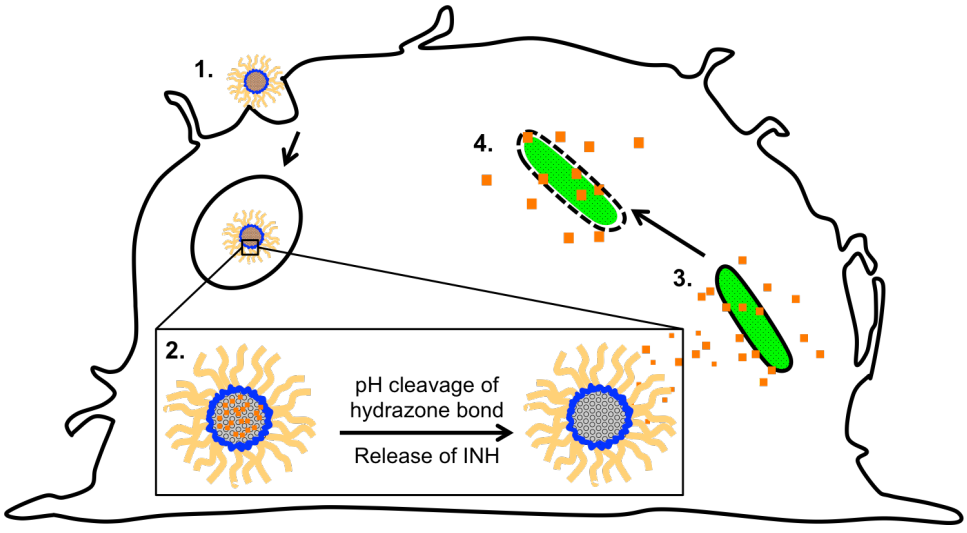

Figure 5.1. Depiction of novel pH-sensitive MSN-CHO-INHs-PEI-PEG system 1) phagocytosed by a macrophage into the acidic endo/lysosome and 2) INH being released with the cleavage of the hydrazone bond holding the cargo to the surface of the MSNs inside the acidic vacuole, 3 & 4) INH is released and delivered into the M. tuberculosis, thereby killing the bacterium.

5.3 Materials and Methods

Materials

All reagents were used as received without further purification. Cetyltrimethylammonium bromide (CTAB, 90%), Pluronic F127 (F127), isoniazid (INH, 99%), rhodamine B isothiocyanate (RITC, 90%), polyethyleneimine (PEI, 1.8 kD, tetraethyl orthosilicate (TEOS, 90%), and 3-(trihydroxysilyl)propyl methylphosphonate monosodium aqueous solution (HTMP, 42% in H_2O) were purchased from Sigma-Aldrich. Triethoxysilylbutyraldehyde (CHO-silane, 90%) poly(ethylene glycol) methyl ether (m-PEG, MW 5 kD) were obtained from Gelest.

Synthesis of 100 nm and 50 nm MSNs

MSNs were synthesized by a simple, solution-based procedure that has been well established in literature.[17,18] Surfactant (cetyltrimethylammonium bromide, CTAB) was dissolved in a basic aqueous solution; the resulting micelles assembled into a 2-dimensional hexagonal structure that served as templating agent for the porous structure. The solution was heated and the silica precursor (tetraethyl orthosilicate, TEOS) condensed around the surfactant template in a base-catalyzed reaction. The solution was aged and the surfactant extracted to produce 100 nm diameter MSNs with ~2 nm diameter pores. Adding an additional surfactant, a triblock copolymer Pluronic F127, to the solution yielded smaller MSNs (SMSNs) with 50 nm diameters, while maintaining the ~2 nm diameter pore size.[19] The nonionic co-surfactant limited the growth of the CTAB micelle structure, yielding smaller nanoparticles.

Functionalization of MSNs and loading with isoniazid

To functionalize the surface of the nanoparticles with aldehyde groups (CHO) for binding drugs, we suspended MSNs (100 mg) in dry toluene (10 mL) and added triethoxysilylbutyraldehyde (200 μl) to the solution. The reaction was heated overnight under nitrogen, cooled, and washed

sequentially with toluene, methanol, and water. Aldehyde-functionalized MSNs (CHO-MSNs) were suspended in a concentrated INH solution (40 mg/mL, Dulbecco's Phosphate Buffered Saline, PBS) and left to load for up to 48 hours. The INH-loaded nanoparticles (MSN-CHO-INHs) were extensively washed with PBS. UV-vis spectra of INH loading were collected by a Cary 500 UV-vis-NIR spectrophotometer. DLS and zeta potentials were measured by ZetaSizer Nano (Malvern Instruments Ltd., Worcestershire, U.K.). Transmission electron microscopy (TEM) images of SMSNs and MSNs were obtained using a JEM1200-EX (JEOL) instrument.

Addition of copolymers (PEI and PEG) to MSN-CHO-INHs and SMSN-CHO-INHs

Stability and dispersion of the MSNs were improved by using copolymers poly(ethylene imine) (PEI) and poly(ethylene glycol) (PEG). Due to the positively charged amines in PEI, the polymer was electrostatically attached to the negatively charged silica surface. MSN-CHO-INHs and SMSN-CHO-INHs (10 mg) were suspended in a PEI solution (2.5 mg/mL, 1.8 kD) for 30 minutes, and the coating was repeated to ensure full coverage. MSNs were collected by centrifugation, and washed sequentially with ethanol and water. The PEG coating was prepared by first synthesizing the activated form of PEG, using poly(ethylene glycol) methyl ether (m-PEG) to prevent crosslinking. The hydroxyl group on m-PEG was replaced with an NHS-ester to react with the amine groups on PEI.[20] PEG was attached to the amine groups of the PEI coating by suspending the PEI-coated MSNs (10 mg) in dry DMF (1.5 mL), adding 50 mg of activated m-PEG, and stirring for 24 hours.

Fluorescence labeling of MSNs

Nanoparticles were labeled with fluorescent dye molecules for imaging purposes. The dye was co-condensed with the silica precursor to ensure labeling throughout the silica matrix. Rhodamine B isothiocyanate (RITC, 2 mg) was dissolved in dry ethanol (1.5 mL), 3-aminopropyltrimethoxysilane (6 μl, APTES) added, and the molecules left to react under nitrogen for 2 hours. TEOS was then added to the solution, and the solution was added drop wise to a

heated (80 °C), aqueous solution of CTAB, NaOH, and aged for 2 hours. The nanoparticles were washed with water and collected by centrifugation.

Trans-cinnamaldehyde derivatization assay

To assess the amount of INH loading on nanoparticles, we suspended 1 mg MSN-CHO-INHs or SMSN-CHO-INHs in 1 mL of PBS or 0.1 N HCl, mixed the suspension on a rotator for 1 hour at room temperature, and centrifuged at 10,000 g for 10 min to collect the nanoparticles. The supernatant was diluted in the range of 1:20 to 1:1000 in 0.1 N HCl to a final volume of 1 mL and mixed with 0.15 mL trans-cinnamaldehyde reagent (0.04%). Reactions with known amount of INH standard were also carried out at the same time. After 15-min incubation at room temperature, the absorbance at 340 nm of the reactions was measured, and the amount of INH in each sample was calculated based on the INH standard curve.

Bacteria

The *M. tuberculosis* virulent strain Erdman (35801; American Type Culture Collection) was used in this study. For the macrophage infection experiments, a single suspension of bacteria was prepared as described previously.[14] For the in vivo studies, a pre-filtered stock of M. tuberculosis Erdman was used to infect mice by aerosol. This stock was prepared by plating guinea pig passaged bacteria one time only on Middlebrook 7H11 agar. A GFPuv expressing M. tuberculosis Erdman strain (Mtb-GFP) was used in MSNs uptake experiments. Mtb-GFP was grown on Middlebrook 7H11 agar containing 50 μg/mL hygromycin and prepared in the same way as the non-fluorescent M. tuberculosis for use in infection experiments.

Macrophages

Peripheral blood monocytic cells were isolated from donor blood by Ficoll-Hypaque centrifugation and incubated in Teflon wells for 5 days to differentiate them into monocyte-derived macrophages (MDM) before use in infection and MSNs uptake experiments. Human monocytic cell

line THP-1 (ATCC TIB202) was maintained in RPMI-1640 (LonzA) with 10% fetal bovine serum. Prior to use in infection experiments, THP-1 cells were treated with phorbol 12-myristate 13-acetate (PMA) to differentiate them into a macrophage-like cell type as described.[14] Briefly, THP-1 cells were pelleted by centrifugation at 200 g for 10 min at room temperature, resuspended in culture medium containing 100 nM PMA, and seeded in 96-well plates (Matrical) at a density of 1 x 10^5 cells/200 µl/well for 3 days at 37 °C in a 5% CO_2-95% air atmosphere.

Uptake of MSNs by M. tuberculosis-infected macrophages

To assess the uptake efficiency of MSNs by infected macrophages, we seeded MDMs in 384-well glass bottom plates (Matrical) and infected them with GFP-expressing M. tuberculosis as described above. At the end of the 90-min incubation period, half of the medium was replaced with fresh medium containing rhodamine isothiocyanate (RITC)-labeled MSNs. The monolayers were fixed at 3 h and 1 day in 4% paraformaldehyde in PBS. Macrophages were incubated with Wheat Germ Agglutinin (WGA)-Alexa Fluor 633 (5 µg/mL) for 5 min at room temperature to stain plasma membranes. Cell nuclei were stained for 10 min with Hoechst 33342 (1 µg/mL) in PBS containing 0.1% Tween 20. Monolayers were washed twice with PBS and imaged with an ImageXpress (Molecular Devices) high throughput epifluorescence microscope using a 10x objective lens. Automated image analysis was performed using the Granularity and Count Nuclei modules of MetaXpress (Molecular Devices) software to quantitate the integrated GFP fluorescence intensity and the number of macrophage nuclei, respectively. CellProfiler software was used to quantitate the degree of co-localization between Mtb-GFP and MSNs-RITC within the same cells.

In vitro efficacy of MSNs in killing M. tuberculosis in macrophages

A single bacterial suspension of M. tuberculosis was used to infect PMA-differentiated, human macrophage-like THP-1 cells at a multiplicity of infection ratio of 10:1 for 90 min at 37 °C, 5% CO_2-95% air. The infected macrophages were washed to remove extracellular bacteria and fresh

medium with or without INH or MSNs was added. The cultures were incubated in the continued presence of INH or MSNs for 3 days after which the infected macrophage monolayers were lysed with 0.1% SDS. Control infected THP-1 monolayers not treated with INH or MSNs were harvested at 2 h and 3 days post infection to assess bacterial growth. Culture supernatant and lysed THP-1 cells were combined, serially diluted, plated on 7H11 agar, and bacterial CFU enumerated after 2 weeks of incubation at 37 °C, 5% CO_2-95% air.

In vivo efficacy of MSNs in treating pulmonary tuberculosis

Eight-week old, female, pathogen-free Balb/c mice (Taconic) were infected with 250-500 CFU of *M. tuberculosis* Erdman via exposure for 30 minutes within an aerosol chamber to an aerosol generated by a Collision Type 6-jet nebulizer (BGI, Inc. Waltham, MA) at 20 psi from a suspension containing ~2 x10^6 CFU/mL *M. tuberculosis* in PBS. The precise number of bacteria used in the aerosol was determined by plating serial dilutions of the stock on Middlebrook 7H11 agar plates and enumerating bacterial CFU. One day later, two mice were euthanized to determine the initial number of bacteria delivered to their lungs. Two weeks later, three mice were euthanized to determine the number of bacteria in the lungs prior to treatment. The mice were then sham-treated, treated with MSN-CHO-INHs, SMSN-CHO-INHs, or free INH 3 days a week (Monday, Wednesday, and Friday) for 2 weeks (total of 6 doses) by tail vein injection. Three days after the last treatment dose, all mice were euthanized and the lung, liver, and spleen removed aseptically. The organs were homogenized in PBS, and the homogenates serially diluted and plated on 7H11 agar containing ampicillin (12.5 μg/mL), amphotericin B (5 μg/mL), and polymyxin B (20 units/mL). The plates were incubated at 37 °C in 5% CO_2-95% air atmosphere for 3 weeks and CFU enumerated.

Biodistribution of MSNs in vivo

Organs harvested from M. tuberculosis-infected mice that were either sham- treated or treated with INH-loaded pH-responsive MSNs were homogenized in PBS, digested with 0.1% HNO_3, and analyzed by inductively coupled plasma optical emission spectrometry (ICP-OES) (ICPE-9000, SHIMADZU, Japan). The amount of silica recovered from each organ was normalized to the total dose of MSNs injected.

Median-Effect plots

We used median effect plots to compare the relative efficacies of free INH, MSN-CHO-INHs and SMSN-CHO-INHs. The fraction of inhibition for samples treated with different amounts of INH was calculated using bacterial CFU in base-10 logarithm (log CFU) with the equation: Fraction of inhibition = 1- (log CFU from sample treated with INH or INH-loaded pH-responsive MSNs/log CFU from untreated sample). A median-effect plot for INH or INH-loaded pH-responsive MSNs was generated using INH or INH equivalent (MSNs) dose in base-10 logarithm as the X-axis and the fraction of surviving bacteria divided by the fraction of killed bacteria in base-10 logarithm as the Y-axis.

Statistics

All statistical analyses were performed using GraphPad Prism software (version 5.03). Experimental comparisons with multiple groups used ANOVA analysis with Bonferroni's post-test correction. Two-tailed Student's t tests were performed for some comparisons, as indicated in the figure captions. A *P* value of 0.05 or less was considered statistically significant.

5.4 Results and Discussion

Current regimens for treatment of tuberculosis are prolonged, requiring 6 – 9 months of multidrug therapy, and are complicated by toxicities, noncompliance, and emergence of drug resistance. Nanoparticle delivery platforms that deliver high concentrations of antibiotic directly to the site of infection have the potential to improve treatment by sterilizing infected tissues more rapidly, reducing the duration of treatment while also reducing systemic drug exposure and off-target toxicities. To achieve this goal, we have developed a stimulus-responsive MSNs drug delivery platform for INH with high (up to 11%) drug loading that releases INH intracellularly after uptake into acidified compartments. Stimulus-responsive release was achieved by bonding the INH to the MSNs via acid-reversible hydrazone bonds. The INH loading is stable at neutral pH for at least one month under refrigeration. We have shown that the MSNs are tolerated well with repeated i.v. administration in mice and that they target tissues of the Mononuclear Phagocyte System that are the sites of tuberculosis infection. Moreover, our ICP-OES silica analysis demonstrates that the MSNs do not accumulate and are cleared, consistent with previous demonstrations of MSNs biodegradability (25-27).

Synthesis of MSNs carrying INH as a prodrug (MSN-CHO-INHs)

Due to the difficulty in trapping isoniazid (INH) in our previous studies, we sought to increase the drug delivery payload of the MSNs using alterative methods. By developing a 'prodrug'-type of MSNs has enabled us to utilize of the high external and internal surface areas of MSNs with a pH-sensitive function. MSNs first were synthesized by a simple, solution-based procedure that has been well established in literature that has been well established in literature.[21,22] The MSNs were aldehyde-functionalized (Figure 5.2 A) by attaching aldehyde-terminated silane to the MSNs. The MSNs were loaded with INH as a prodrug by chemically bonding the hydrazine portion of INH to the aldehyde-functionalized MSNs, forming a pH-sensitive hydrazone bond. At neutral pH (7.4), the

hydrazone bond is stable, but once exposed to acidic conditions (pH 5-6) the hydrazone is hydrolyzed, and the INH can be released and delivered in its original form (Figure 5.2 A).

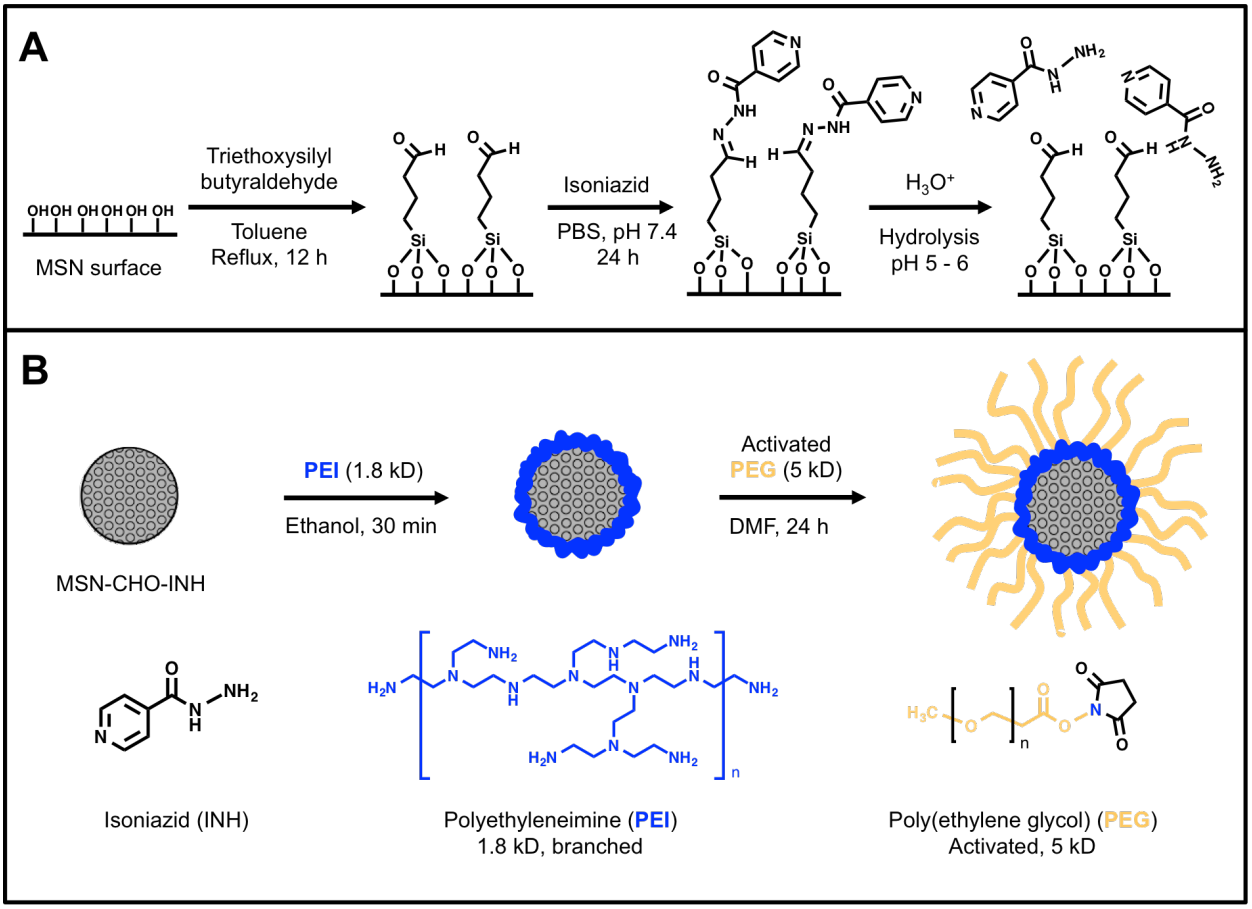

Figure 5.2. A) Synthesis of aldehyde-functionalized MSNs and attachment of isoniazid (INH) onto the surface of the aldehyde-modified nanoparticles, and release of the INH from MSN-CHO-INHs by hydrolysis at acid pH; B) assembly of copolymer PEI-PEG on the INH-loaded pH-responsive MSNs.

Due to the extended angiogenesis that causes hypervasculature in carcinomas, tumor physiology possesses the enhanced permeability and retention (EPR) effect.[23,24] And by redesigning smaller MSNs (SMSNs) with 50 nm diameters, we have seen a higher distribution of silica in the tumor than other vital organs (liver, kidneys, spleen, lung, heart), when compared to traditional MSNs (100 nm).[25] In order to ascertain some information of size dependence in macrophage uptake, we synthesized two sizes of MSNs (50 nm, 100 nm diameters) for the delivery of INH. We

synthesized both types of MSNs using CTAB as a templating agent for the pores; however for the smaller, 50 nm MSNs (SMSNs), we added an additional co-surfactant, Pluronic F127. The copolymer serves to restrict the growth of the CTAB micelle structure and helps stabilize silica nucleation sites, keeping the silica structure small. We evaluated the in vivo and in vitro efficacy of the INH-loaded pH-responsive MSNs – large 100 nm MSNs (MSN-CHO-INHs) and small 50 nm diameter MSNs (SMSN-CHO-INHs). It is well known macrophages can easily phagocytose a wide range of sizes, to objects much larger than themselves. However their discriminatory behavior towards different nanoscale sizes is not well understood.[26] Additionally, intravenously injected MSNs have been shown to be taken up by macrophages of the reticuloendothelial system and accumulate in liver, spleen, and lung, organs that Mtb infects the most.[27,28]

The pH-stimulated release of INH from the MSN-CHO-INHs and SMSN-CHO-INHs was first tested by UV-vis spectroscopy, measuring INH absorbance (λ_{max} = 262 nm) in the MSNs supernatant. We suspended nanoparticles in PBS and obtained the supernatant by centrifugation to obtain the residual drug present. We then resuspended the nanoparticles in 0.1 N HCl (pH 1) for 15 min, collected the nanoparticles by centrifugation, and obtained the supernatant under this condition (acidic release). We measured the absorbance of INH in the residual drug and acidic release solutions at 262 nm. We observed negligible release of INH into the neutral pH solution, but observed substantial release of INH under acid conditions, with a release capacity of the INH-loaded nanoparticles as high as 11% wt (drug / MSNs) (Figure 5.3).

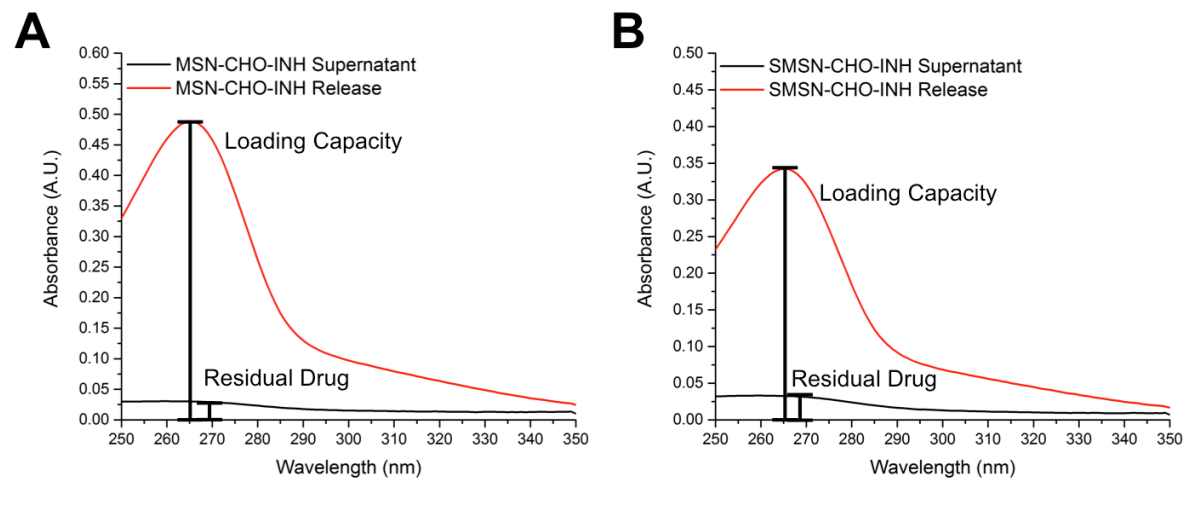

Figure 5.3. UV-vis spectra of pH-stimulated releases: supernatants after washing INH-loaded nanoparticles with PBS (black trace) or with 0.1 N HCl (red trace) demonstrating release of INH under acidic conditions for A) MSNs and B) SMSNs.

Synthesis of PEI-PEG copolymer coated MSN-CHO-INHs

To improve the dispersion and stability of the MSNs in various aqueous media, the copolymer poly(ethylene imine)-poly(ethylene glycol) (PEI-PEG) was added to the particles' surface in a two-step process (Figure 5.2 B). The PEI-PEG copolymer has shown to improve dispersability and promote endosomal escape in biological media.[20,25] First, the aldehyde-terminated silane was first attached to the MSNs and the INH was bonded to the particle as previously described. Subsequently, the PEI polymer was coated onto the surface via electrostatic attraction between the negatively charged silica surface and the cationic polymer. The cationic polymer improves particle dispersion by providing electrostatic repulsion, however can be toxic at high molecular weights above 25 kD.[29] To ensure little to no cytotoxicity, a 1.8 kD PEI polymer was used in throughout this study. Additionally, the positive charge of the PEI enables the 'proton sponge effect' where the high osmotic pressure can cause endosomal rupturing to releasing their contents into cytosol. An amine-reactive form of PEG (5 kD) is attached to the MSNs by utilizing the amines of the PEI. PEG is a

branched, hydrophilic polymer that helps decrease particle aggregation by adding steric hindrance to the nanoparticle.[30] Before and after all modifications of the MSNs, we determined the hydrodynamic radius by dynamic light scattering and zeta potential, and we examined their structure by TEM imaging (Figure 5.4 A&B).

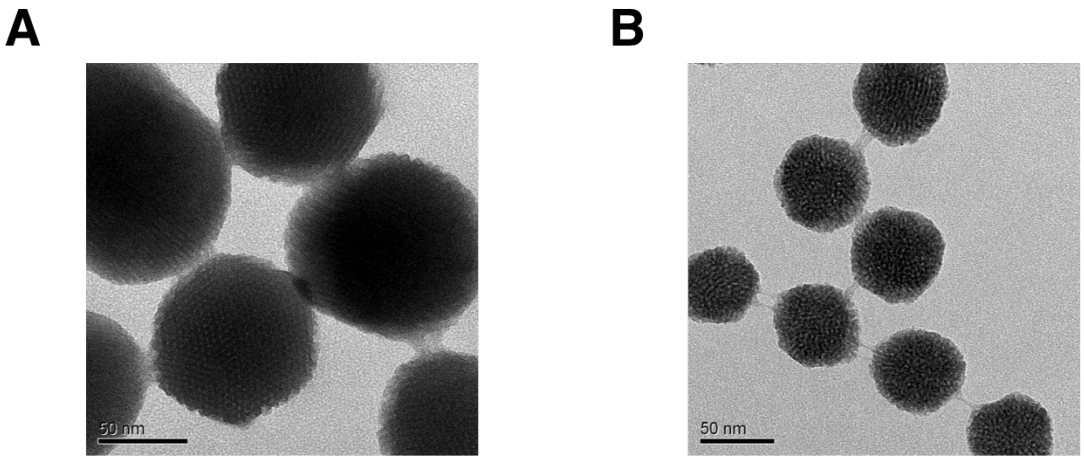

Figure 5.4. TEM images of PEI-PEG copolymer-coated MSN-CHO-INHs A) and B) SMSN-CHO-INHs. The structural integrity of the MSNs is preserved after all surface modifications.

Loading and stability of INH prodrug on MSNs coated with PEI-PEG copolymer

The INH loading and release capacity of the 100 nm and 50 nm MSNs was evaluated by UV-Vis measurements of INH release into neutral and acidic aqueous solutions from the MSNs. At neutral pH, relatively low amounts of INH were detected as being released from the MSNs. In contrast, at acid pH, substantial amounts of INH were released (Figure 5.3). We also evaluated INH release capacity of the MSNs using a trans-cinnamaldehyde derivatization assay (Figure 5.5 A). The INH release capacity for the 100 nm MSN-CHO-INHs was 8.2% wt, and for the smaller 50 nm SMSN-CHO-INHs was 10.8% wt.

A

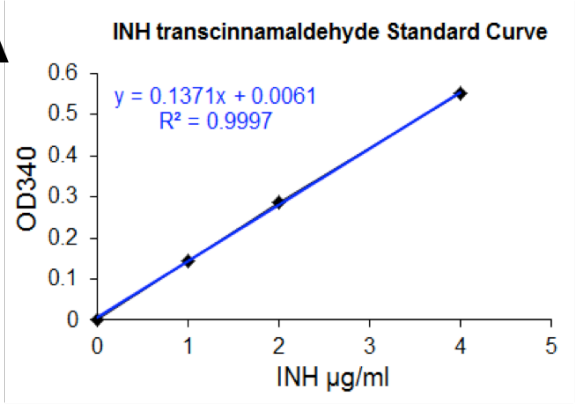

B

Sample	Amount of INH released in PBS, pH 7.4 (wt/wt%)	Amount of INH released in 0.1 N HCl (wt/wt%)	Total Amount of releasable INH (wt/wt%)
MSN-CHO-INH (100 nm)	1.09	8.22	8.22
SMSN-CHO-INH (50 nm)	0.54	10.6	10.6

Figure 5.5. INH release capacity from MSNs. A) The INH standard curve was used to calculate drug release from a batch of MSN-CHO-INHs and SMSN-CHO-INHs and B) MSNs were treated with either a neutral or an acid buffer and not treated sequentially, the total amount of releasable INH is equal to that released under acid conditions.

We evaluated the stability of the hydrazone bond formed between the aldehyde and INH by repeating the release capacity evaluation of the MSNs-CHO-INH after one month storage at 4 °C, again using the trans-cinnamaldehyde derivatization assay. The amount of INH released into the neutral solution remained very low, confirming the stability of the hydrazone bond on the MSNs-CHO-INH. For this sample, we measured 8.3% (wt/wt) release of INH from the MSNs-CHO-INH under acidic pH, similar to the 8.9% (wt/wt) release of INH from the same batch one month earlier (Figure 5.6), demonstrating that the MSNs-CHO-INH is stable for at least one month in storage with negligible INH leakage from the nanoparticle carrier.

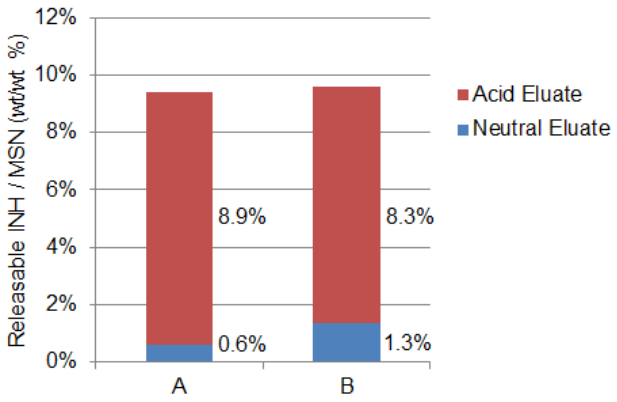

Figure 5.6. MSN-CHO-INHs are stable at 4 °C for at least one month. The nanoparticles were suspended sequentially in PBS, pH 7.4 and then in 0.1 N HCl for 30 min at room temperature The amount of releasable INH in a batch of MSN-CHO-INHs was A) assayed immediately or B) after storage at 4 °C for 1 month with the trans-cinnamaldehyde assay.

Uptake of MSN-CHO-INHs by human macrophages infected with M. tuberculosis

To assess the efficacies of the two types of INH-loaded pH-responsive MSNs (100 nm and 50 nm), we infected differentiated THP-1 macrophage-like cells with virulent *M. tuberculosis* and left them untreated or treated them with A) control MSNs or SMSNs without drug; B) MSN-CHO-INHS; C) SMSN-CHO-INHs; or D) free INH. As shown in Figure 5.7, the rhodamine-labeled MSN-CHO-INHs are taken up avidly by *M. tuberculosis*-infected macrophages. We obtained similar results with the smaller 50 nm MSN-CHO-INHs and with human macrophage-like THP-1 cells. *M. tuberculosis* grew similarly in macrophages that were untreated or treated with control nanoparticles (no INH loaded), indicating that the nanoparticle carrier by itself has no inhibitory effect on the bacterium. The amount of *M. tuberculosis* killing in macrophages treated with free INH, MSN-CHO-INHs, or SMSM-CHO-INH increased in a dose dependent fashion (Figure 5.8 A-C).

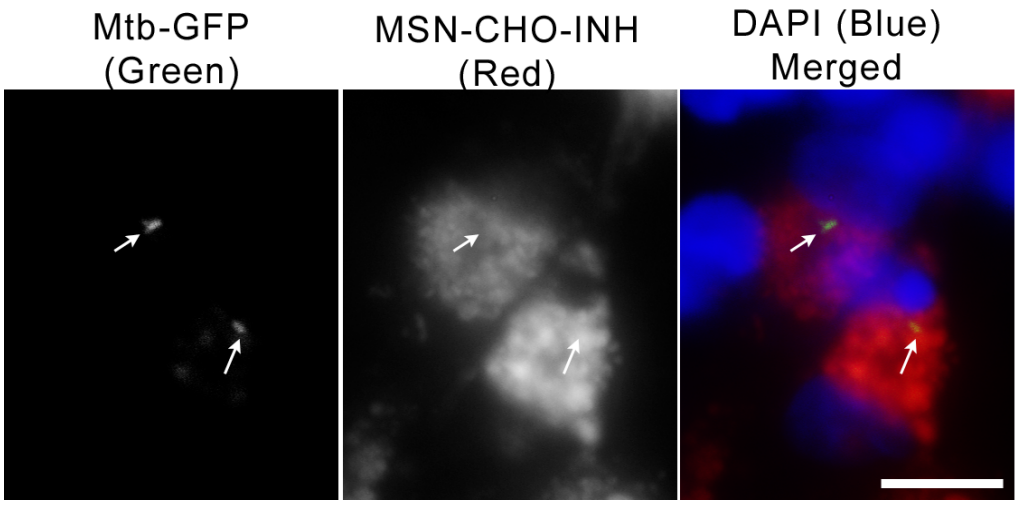

Figure 5.7. Localization of Mtb and MSNs in macrophages. Macrophages in monolayer culture were infected with Mtb-GFP for 90 min, washed, and incubated with 12.5 μg/ml of RITC-labeled MSN-CHO-INHs. After 3 hours, the macrophages were fixed and nuclei stained with DAPI. Left panel (green channel) shows Mtb-GFP (arrows) within the macrophages; central panel (red channel) shows abundant RITC-labeled MSN-CHO-INHs within the macrophages; and right panel (merged color images) shows macrophage nuclei stained blue with DAPI, Mtb-GFP fluorescing green, and RITC-labeled MSN-CHO-INHs fluorescing red. Scale bar, 10 μm.

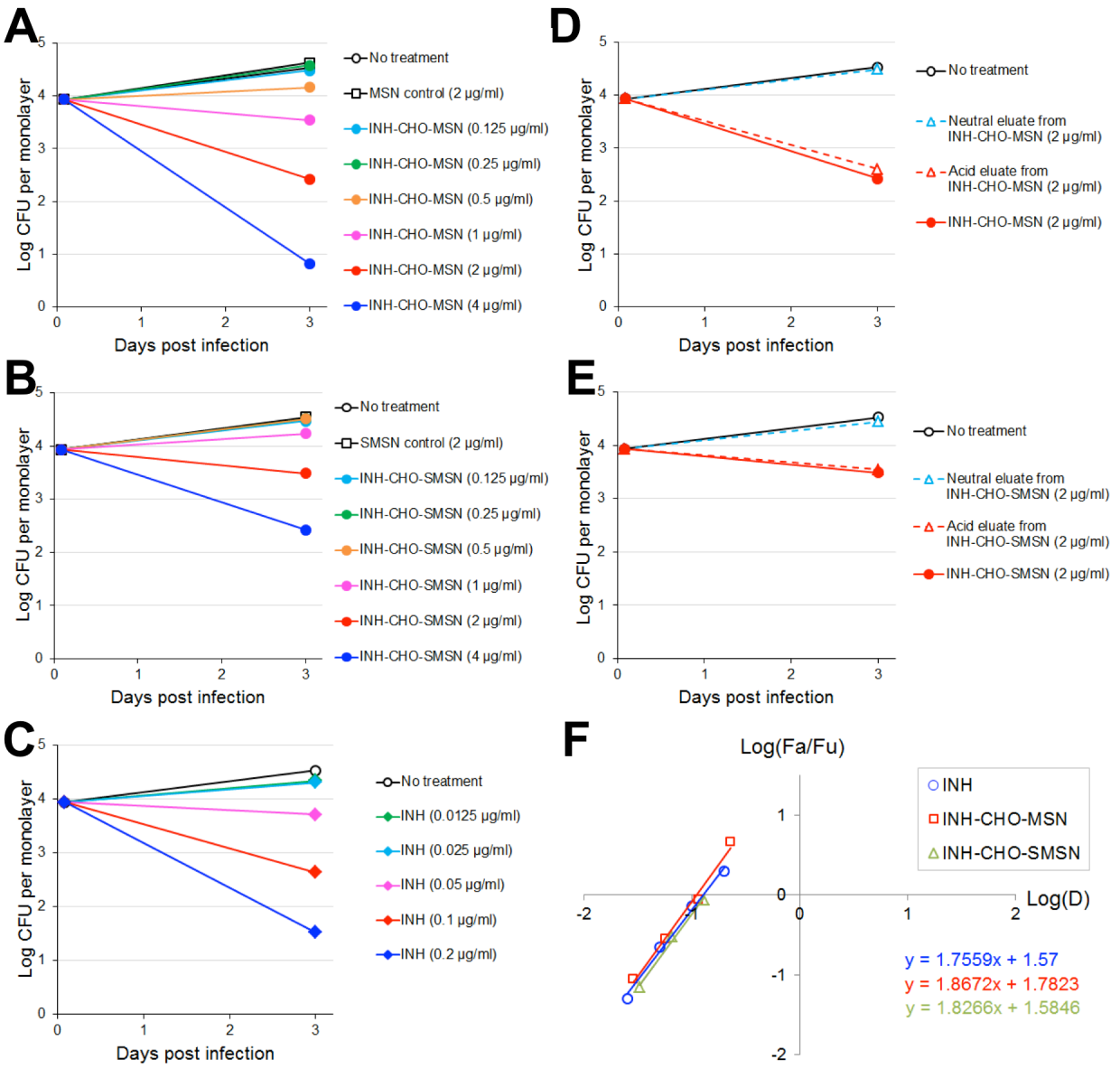

Figure 5.8. Killing of M. tuberculosis in human macrophages by free INH and the 100 nm and 50 nm INH-loaded pH-responsive nanoparticles. THP-1 macrophages were infected with M. tuberculosis and treated with various concentrations of A) MSNs-CHO-INH. B) SMSNs-CHO-INH, or C) INH. D. and E. The killing effect of supernates eluted from D) MSNs-CHO-INH and E) SMSNs-CHO-INH under neutral or acidic conditions on intracellular M. tuberculosis were compared with the killing effect of no treatment or treatment with INH-loaded pH-responsive nanoparticles. F. Median-effect plot, where D is the dose of INH; Fa/Fu is the Fraction of bacteria killed/Fraction of bacteria surviving.

We prepared supernates from MSN-CHO-INHs and SMSN-CHO-INHs resuspended in PBS, pH 7.4 (neutral eluate) or in 0.1 N HCl (acid eluate) and compared the potency of these supernates with the corresponding INH-loaded nanoparticles in killing intracellular M. tuberculosis. As shown in Figure 5.8 D-E, the neutral eluates prepared from MSN-CHO-INHs or SMSN-CHO-INHs had minimal killing effect on intramacrophage M. tuberculosis. In contrast, the acid eluates killed M. tuberculosis to the same extent as the corresponding MSN-CHO-INHs or SMSN-CHO-INHs from which they were prepared. These results confirm that the hydrazone bond formed between INH and the aldehyde-functionalized nanoparticle is hydrolyzed in the acidic macrophage endo-lysosomal environment, releasing INH from the nanoparticles, and that the acid-released INH is biologically active.

With a drug loading of 5.73% wt/wt, 1 μg/ml of MSN-CHO-INHs carried 0.11 μg/ml ofINH and killed 2.1 log of M. tuberculosis, close to the 1.9-log killing achieved by free INH at 0.1 μg/ml. Similarly, 4 μg/ml of SMSN-CHO-INHs, with 3.26% (wt/wt) drug loading, carried 0.13 μg/ml of INH and gave 2.1 log killing of M. tuberculosis. As shown in Figure 5.8 F, the median-effect plot of the free INH and the two types of INH acid-responsive nanoparticles show similar slopes indicating that they have comparable anti-M. tuberculosis efficacy in this cell culture assay system. Thus, this study demonstrates that INH delivered by the MSN-CHO-INHs or SMSN-CHO-INHs is as effective as an equivalent amount of free INH in killing M. tuberculosis in infected human macrophages, indicating an efficacy ratio of 1 in the macrophage cell culture system.

In our macrophage cell culture model, the MSN-CHO-INHs is as effective as equivalent doses of free INH, whereas in vivo, the MSN-CHO-INHs given i.v. or s.q. kill more M. tuberculosis in lung, liver and spleen than 2 – 4 times the equivalent dose of free INH. The higher efficacy ratio of the MSNs-delivered drug in vivo vs. in vitro could reflect a combination of several factors: 1) direct uptake of the MSNs by M. tuberculosis-infected macrophages with release of high

concentrations of INH inside these macrophages, 2) uptake of drug into cells nearby infected macrophages with release of high concentrations of drug in the vicinity of the infected cells, 3) uptake of drug into uninfected mononuclear phagocytes elsewhere in the host that migrate to the site of infection and ingest M. tuberculosis (see below), and/or 4) delayed drug clearance and prolonged drug release by virtue of the drug being encapsulated in MSNs, resulting in improved pharmacokinetics, such as a higher AUC/MIC (Area Under the Curve/ Minimal Inhibitory Concentration) ratio. With respect to the last factor, in the in vitro macrophage model, free INH in the culture medium bathes the infected cells at a constant concentration for the duration of the experiment, whereas after in vivo administration, free INH is cleared rapidly by hepatic metabolism. The half-life of INH after oral administration in mice is 1.7 h, similar to that of human rapid acetylators (41). The half-life of INH in humans is similar after i.v. and oral administration (1.8 h in rapid acetylators and 2.9 h in slow acetylators) (42). Enclosing the INH within MSNs that release the drug only after uptake into acidified compartments shields the drug from immediate metabolism and hepatic clearance and likely provides for a delayed release of drug with more favorable pharmacokinetics.

In Vivo Delivery of INH-PEI-PEG MSNs

To evaluate the efficacy of our 100 nm MSN-CHO-INHs and 50 nm SMSN-CHO-INHs in a mouse model of pulmonary tuberculosis, mice were infected with virulent M. tuberculosis Erdman by aerosol with 250-500 colony-forming units (CFU) delivered into the lung. Over the ensuing two weeks, the bacteria grew 5-logs to approximately 10^7 CFU per lung (Figure 5.9, A&B). Two weeks after aerosol infection, mice were sham-treated or treated with INH-loaded pH-responsive MSNs or free INH with doses matching 1, 2 or 4 fold the equivalent amount of INH loaded on the nanoparticles, 3 times/week for 2 weeks (total of 6 injections) via the i.v. or subcutaneous (s.q.) route. The INH-loaded pH-responsive MSNs were well tolerated by the infected mice as evidenced

by the fact that all treated mice, regardless of nanoparticle size or route of administration, maintained their body weight over the course of treatment (Figure 5.10).

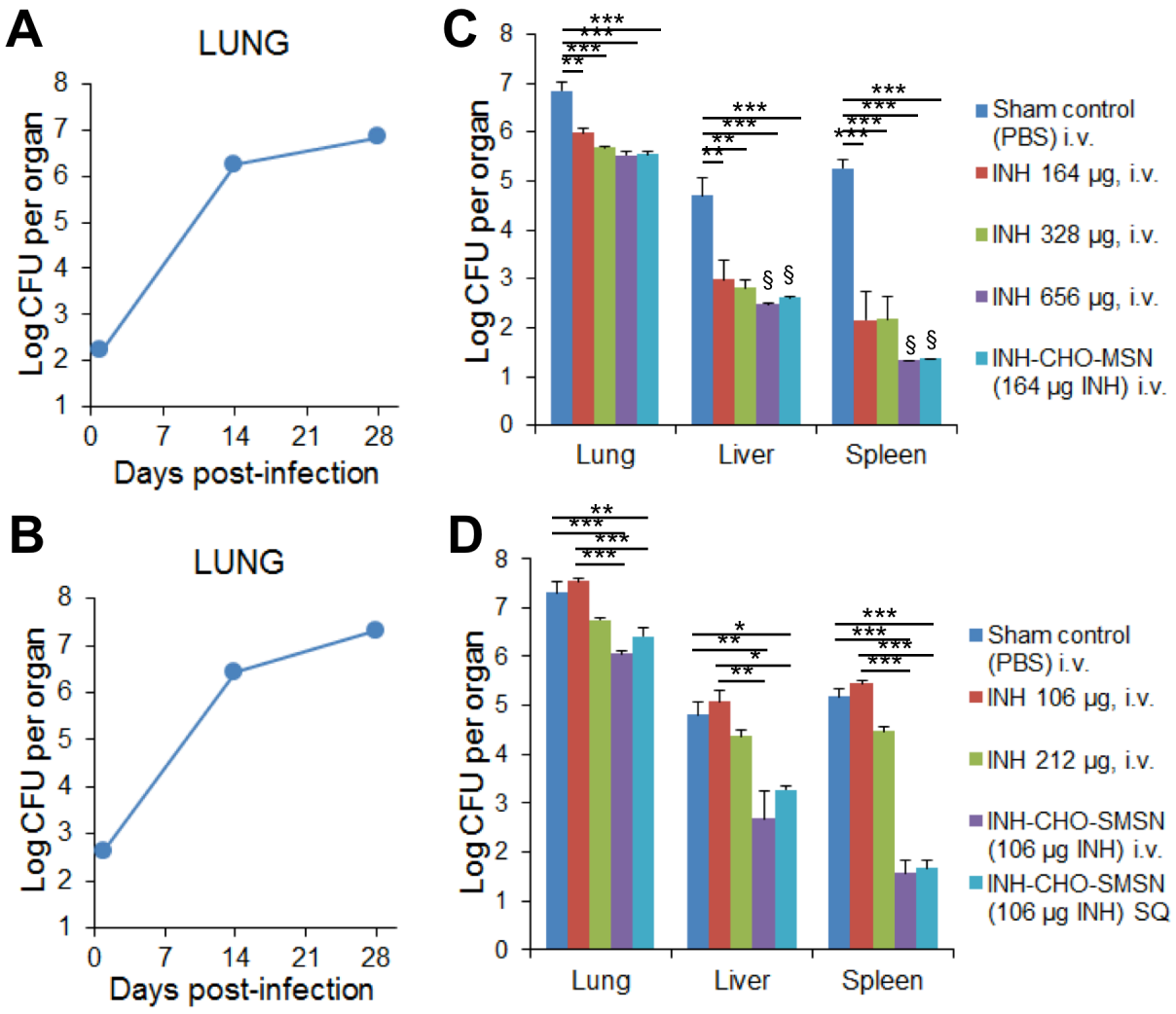

Figure 5.9. In vivo efficacy of MSNs-CHO-INH and SMSNs-CHO-INH. Mice were infected with A) 250 and B) 500 live M. tuberculosis bacilli by aerosol. Bacterial burdens in the lung were monitored throughout the course of infection. The effect of C) MSNs-CHO-INH and D) SMSNs-CHO-INH) treatments on M. tuberculosis burden in lung, liver, and spleen was determined by assaying M. tuberculosis CFU three days after the final treatment. The equivalent amount of free INH for each type of nanoparticle is shown in parenthesis. PBS, phosphate buffered saline; i.v., injection by intravenous route; s.q., injection by subcutaneous route. Statistics were analyzed using one-way ANOVA with Bonferroni post-test correction. *$p < 0.1$, **$p < 0.01$, ***$p < 0.001$. Organ bacterial CFU below the experimental limit of detection.

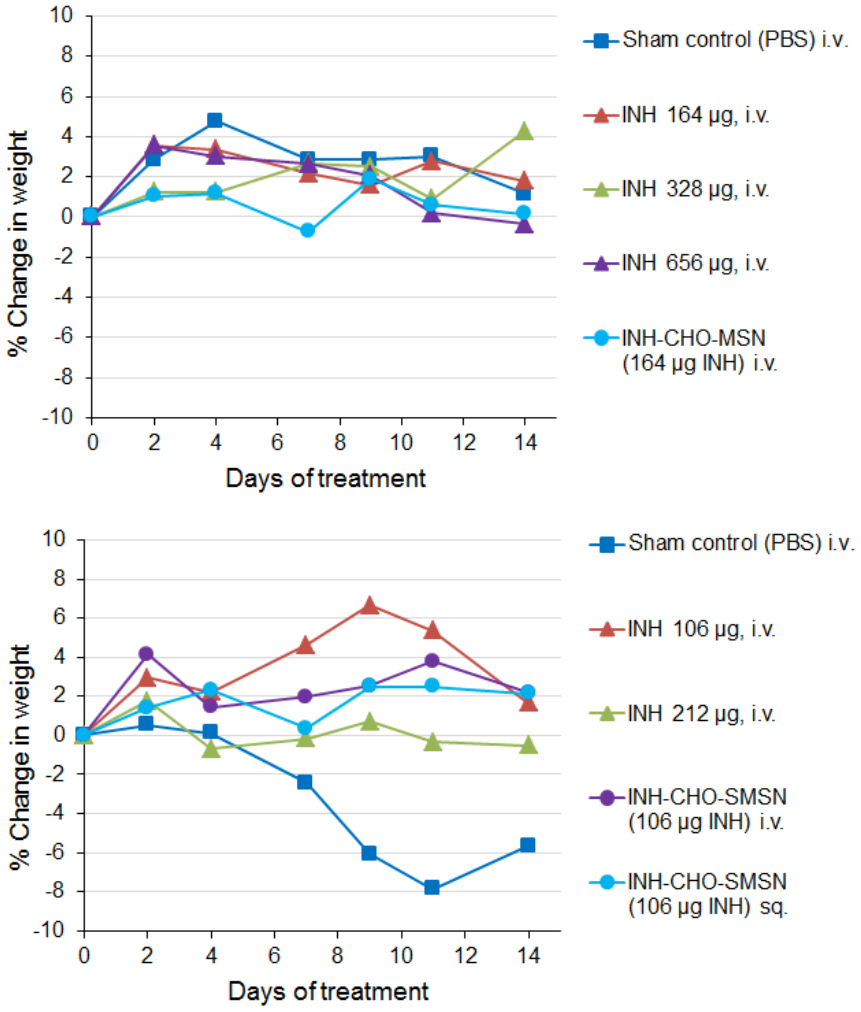

Figure 5.10. Weight charts of infected mice. Mice were sham-treated, treated with free INH, or treated with A) 100 nm MSNs-CHO-INH or B) 50 nm SMSNs-CHO-INH by the intravenous (i.v.) or subcutaneous (s.q.) route, and their weights monitored over the course of treatment. The equivalent amounts of free INH for each type of nanoparticle are shown in parenthesis beneath the name of the nanoparticle in the legend. PBS, phosphate buffered saline.

The bacterial burden in mice treated with MSN-CHO-INHs, compared with sham-treated mice, was reduced by 1.3 logs in the lung, 2.1 logs in the liver, and 3.9 logs in the spleen (Figure 5.9 C). The reduction in bacterial CFU in the lung achieved by MSN-CHO-INHs was significantly

greater than that achieved by an equivalent amount of free INH (t-test, $p < 0.005$). Of note, bacterial burden in the organs of mice treated with MSN-CHO-INHs was as low as that in mice treated with 4-fold the equivalent amount of free INH, consistent with an efficacy ratio of 4 for the MSN-CHO-INHs vs. free drug. In the liver and spleen, both the MSN-CHO-INHs and the 4-fold amount of free INH lowered bacterial CFU to a level below the limit of detection. Mice treated with SMSN-CHO-INHs by either the i.v. or s.q. route had significantly fewer bacteria in the lung, liver, and spleen than mice treated with 2-fold the amount of free INH (Figure 5.9 D), consistent with an efficacy ratio of 2. These results demonstrate that both 100 nm MSN-CHO-INHs and 50 nm SMSN-CHO-INHs are more effective than two to four times the equivalent amount of INH (Figure 5.11). Interestingly, SMSN-CHO-INHs showed comparable efficacies when delivered s.q. or i.v. Consistent with the reduced bacterial organ burden, mice treated with INH-loaded pH-responsive MSNs also exhibited reduced numbers of surface lesions on their lungs (Figure 5.12).

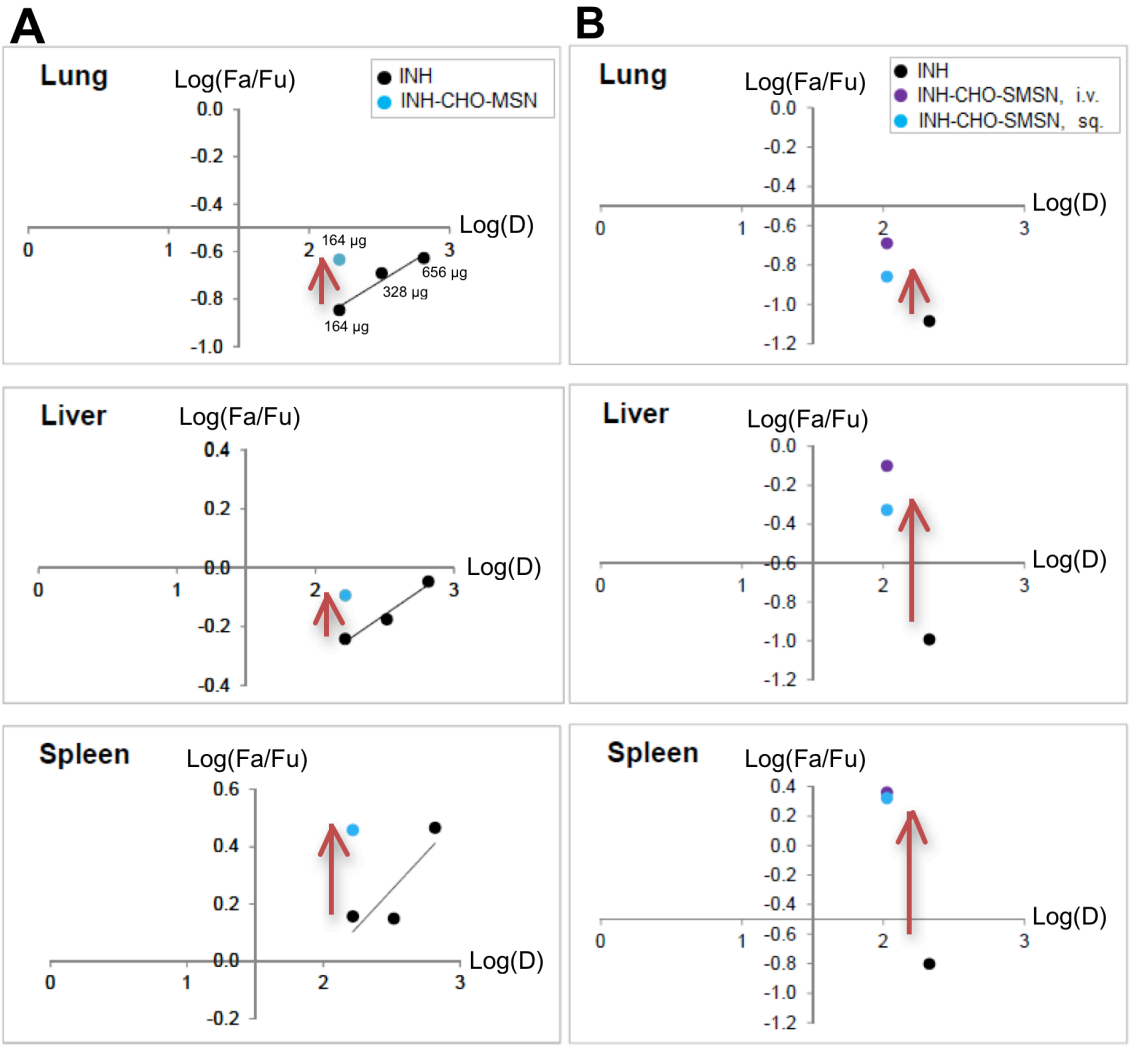

Figure 5.11. Median-effect plots to compare efficacy of MSNs vs. free drug. The efficacy of A) 100 nm MSNs-CHO-INH and B) 50 nm SMSNs-CHO-INH in the lung, liver, and spleen was compared to that of free INH in a Median-effect plot. For a given dose of INH, an upward shift (as indicated by the arrows) on the y-axis indicates a greater killing efficacy. Fa/Fu: Fraction killed/Fraction surviving; D: Dose of INH in micrograms.

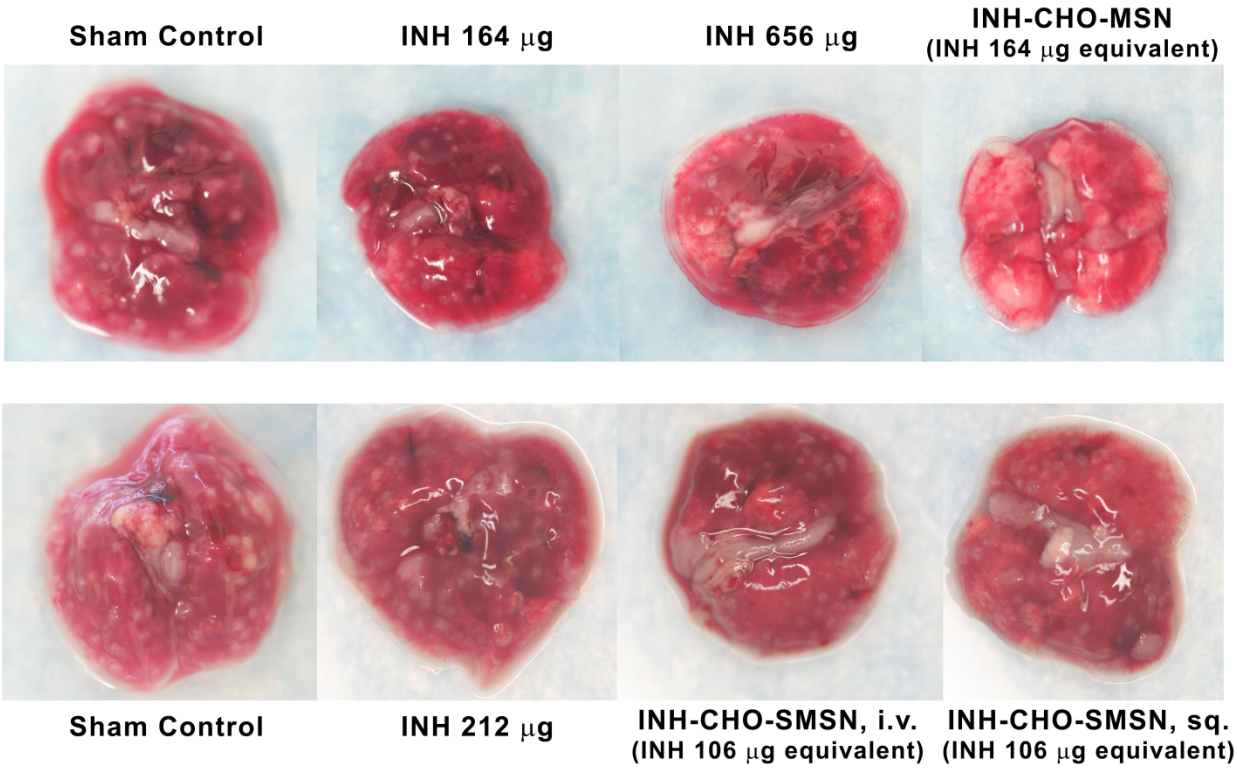

Figure 5.12. Gross pathology of lungs dissected from sham-treated or mice treated with INH or INH-loaded pH-responsive MSNs (100 nm) or SMSNs (50 nm) by intravenous (i.v.) or subcutaneous (s.q.) injection.

Both s.q. and i.v. administered MSN-CHO-INHs were more effective than i.v. administered free drug. While it is likely that the improved efficacy of nanoparticle-delivered drug vs. free drug is due in large part to improved pharmacokinetics (i.e. greater AUC due to sustained drug release), delivery of the drug-loaded nanoparticle to M. tuberculosis-infected lung tissue may occur via both routes of administration, thereby providing for higher tissue levels of drug and enhanced therapeutic efficacy. Subcutaneously administered MSNs could either enter the blood directly or be taken up by uninfected macrophages that subsequently migrate to sites of M. tuberculosis infection, including the lung.

The in vivo efficacy of MSNs-platforms is greatly impacted by the size of the MSNs, because size impacts both tissue penetration and cellular uptake of the MSNs. In the case of tumors, 100 nm

MSNs are suitable to transit the vasculature by virtue of the enhanced permeability and retention (EPR) effect, but show poor diffusion into the collagen matrix of the interstitial space, whereas smaller nanoparticles are able to penetrate further. Lu et al. demonstrated that for MSNs of 30 nm – 200 nm, optimum endocytic uptake by HeLa cells was achieved with MSNs of 50 nm size and Zhang et al. identified 30 nm as the optimal size for endocytic uptake of nanoparticles based on thermodynamic considerations. We have observed that smaller MSNs (SMSNs) with 50 nm diameters achieve a higher distribution than traditional MSNs (100 nm) into tumor tissue and lower distribution into other vital organs (liver, kidneys, spleen, lung, heart). While macrophages are known to phagocytose a wide range of sizes, including objects much larger than themselves, their discriminatory behavior towards different nanoscale sizes is less well characterized, but Walkey et al.[26] demonstrated greater uptake efficiency by J774 mouse macrophages for 90 nm gold nanoparticles than 60 nm, 30 nm, or 15 nm nanoparticles. In this study, we examined two sizes of MSNs (100 nm and 50 nm diameters) for the delivery of INH in vitro and in vivo. These two MSNs had somewhat different tissue distribution, but both were highly effective against M. tuberculosis both in vitro and in vivo.

Distribution of MSNs In Vivo

In order to understand the clearance and biodistribution of nanoparticles in vivo over time, ICP-OES analysis of the silicon content present in animal organs was utilized. In short-term studies, we administered nanoparticles to mice in a single dose by i.v. (tail vein) injection and euthanized the mice 24 hours after injection (24 hour time point). In long-term studies, we injected mice three times a week for two weeks and euthanized the mice 72 hours after the last injection (2 weeks, 72 hour time point). Organs were digested and analyzed for Si content via ICP-OES elemental analysis. Figure 5.13 shows the distribution of nanoparticles can vary greatly, depending on surface chemistry, size, and time.

In the short-term study, the larger nanoparticles (MSN-CHO-INHs) preferentially localized to the liver followed by the spleen, whereas the smaller nanoparticles (SMSN-CHO-INHs) preferentially localized to the spleen followed by the lung (Figure 5.13, A&C). Interestingly, at the 24-hour time point, the SMSNs showed a 4-fold greater delivery to the lungs than the larger MSNs. In the long-term study, the larger MSNs showed a localization pattern similar to that in the short-term study. However, the quantities of silica present were much lower, indicating that most of the silica had been cleared by 72 h after the last of six injections (Figure 5.13 B). On the other hand, the SMSNs showed a different localization pattern in the long-term study with the liver now the primary location (Figure 5.13 D). This study demonstrates that the majority of the silica was cleared from animal organs by three days after the last of six doses, as only a small percentage of the total injected silica remained (5.13% for the five organs for MSN-CHO-INHs and 2.69% for SMSN-CHO-INHs).

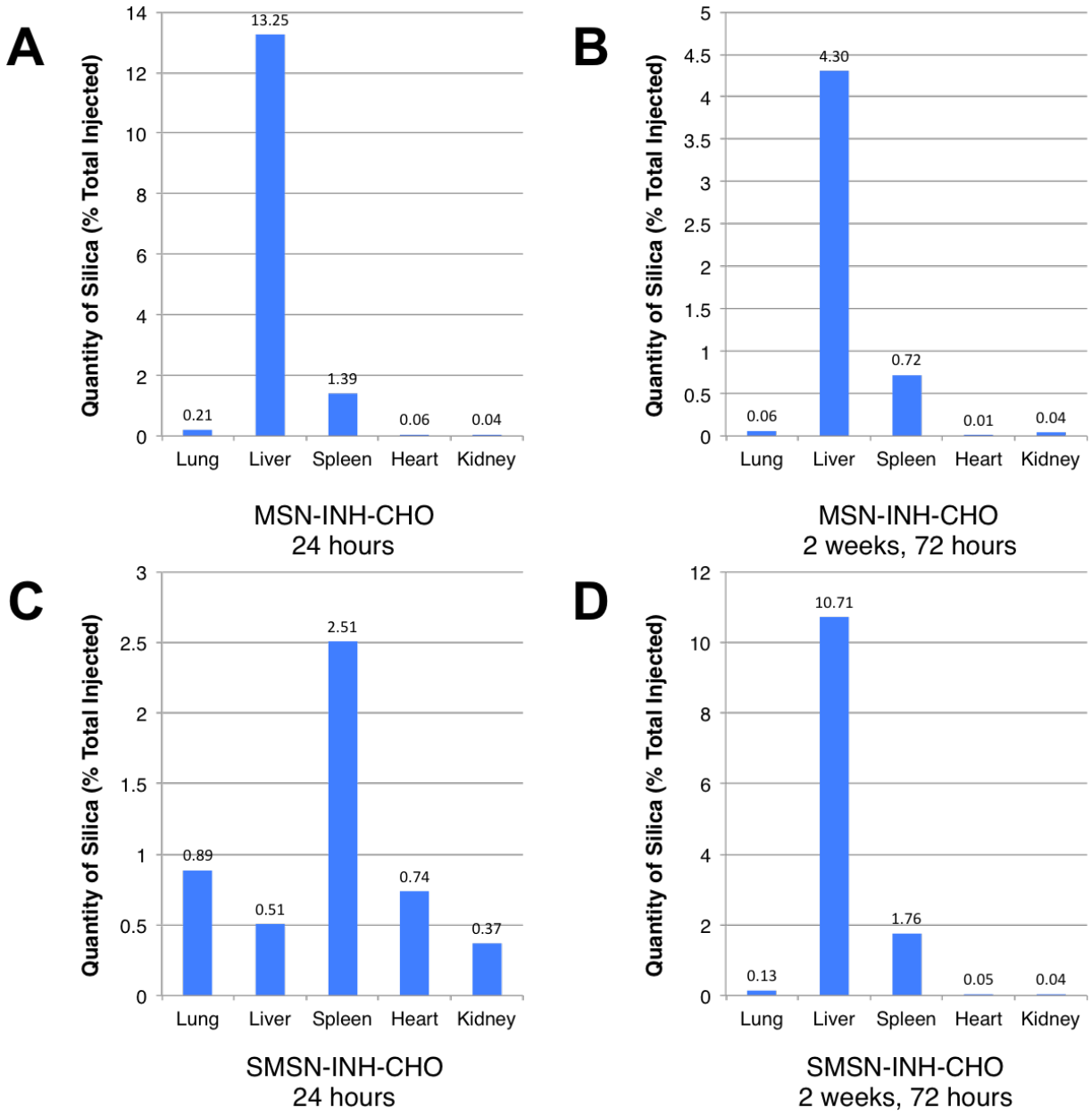

Figure 5.13. Distribution of MSNs-CHO-INH and SMSNs-CHO-INH in animal organs. The distribution of i.v. administered A) & B) MSNs-CHO-INH and C) & D) SMSNs-CHO-INH in lung, liver, spleen, heart and kidney 24 h after a single injection (A, C) or 72 h after six injections over 2 weeks (B, D) was determined by ICP-OES analysis of silica. A and C) At 24 h after a single injection, A) MSNs-CHO-INH are primarily in the liver, while C) SMSNs-CHO-INH are well distributed throughout the body. At 72 h after six injections spread over 2 weeks, MSNs-CHO-INH and SMSNs-CHO-INH show a similar distribution pattern – primarily in the liver, spleen and lung – but mice injected with SMSNs-CHO-INH have more than twice as much silica in these organs as mice injected with MSNs-CHO-INH.

5.5 Conclusion

Our nanoparticle delivery system for treatment of TB differs from previous systems that have been tested in vivo in that it is engineered to be stimulus responsive to release drug only after uptake into acidified intracellular compartments as opposed to being a passive biodegradable drug encapsulation system. While our present demonstration that a stimulus responsive nanoparticle INH delivery system has greater in vivo therapeutic efficacy than free drug is an important proof of principle, incorporation of additional rational design features has the potential for even greater improvement in efficacy. For example, modifications of the MSNs to enhance pulmonary targeting or to optimize the drug release profile would be expected to further enhance efficacy. Aerosol delivery of the MSNs represents another important modification for potential enhancement of therapeutic efficacy. Delivering the pH-responsive INH-loaded MSNs by aerosol inhalation would immediately target the lung, avoiding systemic toxicities and potentially providing high concentrations of drug directly to infected lung tissue, thus potentially greatly enhancing efficacy.

5.6 References

(1) Van Hest, R.; Baars, H.; Kik, S.; van Gerven, P.; Trompenaars, M.-C.; Kalisvaart, N.; Keizer, S.; Borgdorff, M.; Mensen, M.; Cobelens, F. *Clin. Infect. Dis.* **2004**, *39*, 488–496.

(2) Tostmann, A.; Boeree, M. J.; Aarnoutse, R. E.; De Lange, W. C. M.; Van Der Ven, A. J. a M.; Dekhuijzen, R. *J. Gastroenterol. Hepatol.* **2008**, *23*, 192–202.

(3) Mamaeva, V.; Sahlgren, C.; Lindén, M. *Adv. Drug Deliv. Rev.* **2013**, *65*, 689–702.

(4) Li, Z.; Barnes, J. C.; Bosoy, A.; Stoddart, J. F.; Zink, J. I. *Chem. Soc. Rev.* **2012**, *41*, 2590–2605.

(5) Slowing, I. I.; Vivero-Escoto, J. L.; Wu, C.-W.; Lin, V. S.-Y. *Adv. Drug Deliv. Rev.* **2008**, *60*, 1278–1288.

(6) Zhang, Y.; Hsu, B. Y. W.; Ren, C.; Li, X.; Wang, J. *Chem. Soc. Rev.* **2015**, *44*, 315–335.

(7) Trewyn, B. G.; Slowing, I. I.; Giri, S.; Chen, H.-T.; Lin, V. S.-Y. *Acc. Chem. Res.* **2007**, *40*, 846–853.

(8) He, Q.; Shi, J. *J. Mater. Chem.* **2011**, *21*, 5845.

(9) Suzuki, K.; Ikari, K.; Imai, H. *J. Am. Chem. Soc.* **2004**, *126*, 462–463.

(10) Ikari, K.; Suzuki, K.; Imai, H. *Langmuir* **2006**, *22*, 802–806.

(11) Mackowiak, S. a; Schmidt, A.; Weiss, V.; Argyo, C.; von Schirnding, C.; Bein, T.; Bräuchle, C. *Nano Lett.* **2013**.

(12) Zhao, Y.; Trewyn, B. G.; Slowing, I. I.; Lin, V. S.-Y. *J. Am. Chem. Soc.* **2009**, *131*, 8398–8400.

(13) Aznar, E.; Villalonga, R.; Giménez, C.; Sancenón, F.; Marcos, M. D.; Martínez-Máñez, R.; Díez, P.; Pingarrón, J. M.; Amorós, P. *Chem. Commun. (Camb).* **2013**, *49*, 6391–6393.

(14) Clemens, D. L.; Lee, B.-Y.; Xue, M.; Thomas, C. R.; Meng, H.; Ferris, D.; Nel, A. E.; Zink, J. I.; Horwitz, M. a. *Antimicrob. Agents Chemother.* **2012**, *56*, 2535–2545.

(15) Li, Z.-Y.; Liu, Y.; Wang, X.-Q.; Liu, L.-H.; Hu, J.-J.; Luo, G.-F.; Chen, W.-H.; Rong, L.; Zhang, X.-Z. *ACS Appl. Mater. Interfaces* **2013**, *5*, 7995–8001.

(16) Fan, J.; Fang, G.; Wang, X.; Zeng, F.; Xiang, Y.; Wu, S. *Nanotechnology* **2011**, *22*, 455102.

(17) Vivero-Escoto, J. L.; Slowing, I. I.; Trewyn, B. G.; Lin, V. S.-Y. *Small* **2010**, *6*, 1952–1967.

(18) Wu, S.-H.; Mou, C.-Y.; Lin, H.-P. *Chem. Soc. Rev.* **2013**, *42*, 3862–3875.

(19) Meng, H.; Mai, W. X.; Zhang, H.; Xue, M.; Xia, T.; Lin, S.; Wang, X.; Zhao, Y.; Ji, Z.; Zink, J. I.; Nel, A. E. *ACS Nano* **2013**, *7*, 994–1005.

(20) Xia, T.; Kovochich, M.; Liong, M.; Meng, H.; Kabehie, S.; George, S.; Zink, J. I.; Nel, A. E. *ACS Nano* **2009**, *3*, 3273–3286.

(21) Patil, R.; Portilla-Arias, J.; Ding, H.; Konda, B.; Rekechenetskiy, A.; Inoue, S.; Black, K. L.; Holler, E.; Ljubimova, J. Y. *Int. J. Mol. Sci.* **2012**, *13*, 11681–11693.

(22) Rollas, S.; Küçükgüzel, S. G. *Molecules* **2007**, *12*, 1910–1939.

(23) Lu, F.; Wu, S.-H.; Hung, Y.; Mou, C.-Y. *Small* **2009**, *5*, 1408–1413.

(24) Zhang, S.; Li, J.; Lykotrafitis, G.; Bao, G.; Suresh, S. *Adv. Mater.* **2009**, *21*, 419–424.

(25) Meng, H.; Xue, M.; Xia, T.; Ji, Z.; Tarn, D. Y.; Zink, J. I.; Nel, A. E. *ACS Nano* **2011**, *5*, 4131–4144.

(26) Walkey, C. D.; Olsen, J. B.; Guo, H.; Emili, A.; Chan, W. C. W. *J. Am. Chem. Soc.* **2012**, *134*, 2139–2147.

(27) Kumar, R.; Roy, I.; Ohulchanskky, T. Y.; Vathy, L. a; Bergey, E. J.; Sajjad, M.; Prasad, P. N. *ACS Nano* **2010**, *4*, 699–708.

(28) He, Q.; Zhang, Z.; Gao, F.; Li, Y.; Shi, J. *Small* **2011**, *7*, 271–280.

(29) Meng, H.; Liong, M.; Xia, T.; Li, Z.; Ji, Z.; Zink, J. I.; Nel, A. E. *ACS Nano* **2010**, *4*, 4539–4550.

(30) Bagwe, R. P.; Hilliard, L. R.; Tan, W. *Langmuir* **2006**, *22*, 4357–4362.

(31) Liong, M.; Lu, J.; Kovochich, M.; Xia, T.; Ruehm, S. G.; Nel, A. E.; Tamanoi, F.; Zink, J. I. *ACS Nano* **2008**, *2*, 889–896.